

AN ABSTRACT OF THE THESIS OF

David J. Matthews for the degree of Master of Science in Electrical and Computer Engineering presented on December 18 2013.

Title: Fabrication of a Flexible Glucose Sensing Catheter for Human Implantation

Abstract approved:

John F. Conley, Jr.

Flexible electronics processing techniques were applied to integrate a glucose sensor with a hormone-delivery catheter in order to create a cheap and minimally invasive method for patients with type 1 diabetes to continually monitor and control their blood sugar levels. Ultimately, this work intends to move toward the development of a complete artificial pancreas. The theory, development, and optimization of a process to fabricate these sensors/catheters is discussed along with electrical and mechanical characterization of the resulting devices. Experiments performed in the process of device development are presented, including data indicating that aluminum oxide deposited via atomic layer deposition (ALD) may not be suitable for application in flexible devices intended to withstand extreme curvature.

As an additional topic, a model of ALD in porous materials is presented as applied to deposition of aluminum oxide in carbon nanocrystal (CNC) aerogels. Aerogel geometry was modeled as a simple three-dimensional cubic network of cylinders, and recently published modeling techniques were applied to generate expected thickness profiles of ALD alumina as a function of depth into an aerogel sample. Modeled thickness profiles were generally found to agree with experimental observations, suggesting the usefulness of this model for ALD in aerogels and other complex porous geometries.

©Copyright by David J. Matthews
December 18, 2013
All Rights Reserved

Fabrication of a Flexible Glucose Sensing Catheter for Human Implantation

by
David J. Matthews

A THESIS

submitted to

Oregon State University

in partial fulfillment of
the requirements for the
degree of

Master of Science

Presented December 18, 2013
Commencement June 2014

Master of Science thesis of David J. Matthews presented on December 18, 2013

APPROVED:

Major Professor, representing Electrical and Computer Engineering

Director of the School of Electrical Engineering and Computer Science

Dean of the Graduate School

I understand that my thesis will become part of the permanent collection of Oregon State University libraries. My signature below authorizes release of my thesis to any reader upon request.

David J. Matthews, Author

ACKNOWLEDGEMENTS

I would like to first thank my wonderful girlfriend Halley Farwood for dealing with and supporting me from afar while I continue my education in a different city.

I would like to thank Dr. John Conley for aiding my transition from physics to engineering and for providing technical and professional advice throughout my stay at Oregon State University (OSU). Dr. Souvik Kundu provided valuable assistance in performing much of the processing and organization of this work. Chris Durgan, Dr. Greg Herman, Dr. Xiaosong Du, Dr. Liney Arnadóttir, and undergraduates Geoffrey Zath, Jacob Johnson, Jonah Flick, Matt Bates, Tyler Schmeckpeper, Kovit Pholsena, and Josh Motley all contributed to the fabrication and characterization of glucose oxidase and diffusion barrier materials. Tyler Klarr provided assistance with sputtering and project organization in the early stages of this project, and many thanks to Rick Presley, Casey Hines, and lab manager Chris Tasker for doing the work of an entire team of engineers and technicians to maintain the Materials Synthesis and Characterization Facility (MASC) where the majority of this work occurred.

The members of Pacific Diabetes Technologies (PDT) and those who work with them, including CEO Dr. Robert Cargill, Dr. Ken Ward, Dr. Jessica Castle, Sheila Benware, Pete Jacobs, Kristin Morris, Tyler Milhem, and Peter Hannaway, provided funding, direction, chemical and physical characterization, and other assistance, and I hope that they will be successful in continuing the work described herein to realization of a full artificial pancreas.

Primary funding for this project came from The National Institutes of Health (NIH, grant number 1-R43-DK-096678-01), The Leona M. and Harry B. Helmsley

Charitable Trust (grant number 2012PG_T1D034), and the Oregon Nanoscience and Microtechnologies Institute (ONAMI). MASC, the Microproducts Breakthrough Institute (MBI), the Pacific Northwest National Laboratory (PNNL), and the Electron Microscopy Facility (EMF) at OSU provided some of the tools and facilities that made this project possible.

I would also like to thank Sean Smith, Dustin Austin, Simon Reissman, and the other members of Dr. Conley's research group through most of this project, each of whom provided valuable input at some stage of this project. Finally, many thanks to each of the professors that I took classes from throughout my education, and thanks to Drs. John Wager, David Cann, Julia Jones, and, again, John Conley for serving as my thesis committee.

TABLE OF CONTENTS

	<u>Page</u>
1. Introduction.....	1
2. Background.....	5
2.1 Glucose sensing: motivation and history	5
2.1.1 Point glucose monitoring.....	6
2.1.2 Continuous glucose monitoring.....	7
2.2 Device working principles	10
2.2.1 Equivalent circuit model.....	10
2.2.2 Glucose oxidase for glucose detection	13
2.2.3 Inactivated GOx to enhance selectivity	14
2.2.4 Diffusion barrier to enhance linearity.....	15
2.2.5 Silver / silver chloride reference electrode	16
2.2.6 Passivation and microstructure formation	17
2.3 Brief history of flexible electronics	18
2.4 Theory of flexible electronics	19
2.4.1 Internal stresses.....	20
2.4.2 Adhesion and cohesion	22
2.4.3 Design for flexible electronics.....	24
3. Materials and Methods.....	27
3.1 Materials	27
3.1.1 Substrates.....	27
3.1.2 Rigidization.....	28
3.1.3 Conductive traces.....	30

3.1.4 Adhesion promotion	32
3.1.5 Passivation	32
3.2 Deposition methods	33
3.2.1 Physical vapor deposition processes.....	33
3.2.2 Atomic layer deposition.....	35
3.2.3 Liquid-state deposition processes	38
3.3 Patterning	40
3.3.1 Masking	40
3.3.2 Etching.....	42
3.4 Surface treatments.....	46
3.5 Characterization	48
3.5.1 Surface energy	48
3.5.2 Interfacial adhesion.....	49
3.5.3 Mechanical durability	50
3.5.4 Imaging and elemental analysis.....	52
3.5.5 Electrochemical response	54
4. Development of a Flexible Device Foundation	56
4.1 Device preparation	56
4.2 Rigidization.....	58
4.2.1 Initial rigidization methods.....	58
4.2.2 Gel-Pak DGL film	60
4.3 Al ₂ O ₃ interlayers	63
4.3.1 Thicker Ti to compensate for Al ₂ O ₃ failure.....	63
4.3.2 Surface treatments for interfacial adhesion	67

4.3.3 Investigation of adhesive failure.....	69
4.3.4 Effect of Al ₂ O ₃ thickness.....	73
4.4 Titanium deposition on polyimide	75
4.5 Gold-coated polymer substrates.....	81
4.5.1 Polymer substrates.....	81
4.4.2 Gold-coated polyimide	81
4.6 Conclusion	87
5. Process development for sensor fabrication	89
5.1 Layout and process flow	89
5.1.1 Device layout.....	91
5.1.2 Process flow.....	94
5.2 Process development.....	99
5.2.1 Metal deposition	99
5.2.4 Patterning.....	100
.....	104
5.2.5 Etching.....	105
5.2.6 Passivation and well formation.....	105
5.2.7 Glucose oxidase and diffusion barrier	108
5.2.8 Device encapsulation and fixturing	110
5.3 Durability characterization.....	111
5.4 Conclusion	114
6. Summary and Future work in flexible electronics	115
6.1 Further investigation of metal/polyimide adhesion	115
6.2 Improvements in glucose sensor design and processing.....	116

6.2.1 Mask layout	116
6.2.2 Processing	118
6.3 Toward an artificial pancreas	119
7. Modeling Atomic Layer Deposition in Porous Substrates	120
7.1 Introduction	120
7.2 Background	121
7.2.1 Aerogels and other porous materials	121
7.2.2 Atomic layer deposition in porous substrates	122
7.3 Model development	124
7.4 Experimental application to ALD in CNC aerogels	128
7.5 Results	129
7.6 Conclusion and future work	134
Bibliography	137
Appendix 1: Mask set	151
Appendix 2: Run sheet through SU-8 deposition	155
Appendix 3: 50 nm ALD Al ₂ O ₃ recipe	157
Appendix 4: Matlab code for ALD model	159

LIST OF FIGURES

<u>Figure</u>	<u>Page</u>
2.1 Glucose sensing technologies in use or under development.....	9
2.2 Equivalent circuit model for the developed glucose sensor.....	10
2.3 Cross-sectional schematic representation of developed sensor.....	12
3.1 ALD cycle.....	37
3.2 EDHP printed patterns.....	39
3.3 Liftoff processing errors.....	43
3.4 Automated flex tester.....	51
3.5 Utility of back-lit microscopy.....	53
4.1 Al ₂ O ₃ device stack.....	58
4.2 Processing flaws for devices produced with different rigidization methods.....	60
4.3 Failed initial Al ₂ O ₃ devices.....	64
4.4 Electrical resistance change with bending for constant Al ₂ O ₃ thickness and varied Ti thickness.....	66
4.5 Representative images of failed samples with 50 nm Al ₂ O ₃	69
4.6 EDAX spectra from delaminated metal and the surface beneath.....	72
4.7 Representative results of bending and scratch tests for varied Al ₂ O ₃ thicknesses.....	74
4.8 Titanium on polyimide device stack.....	75
4.9 Contact angle measurements on polyimide.....	77
4.10 Contact angle values for polyimide surface treatments.....	77
4.11 Bending results of titanium on polyimide with and without plasma treatment...	79
4.12 Gold-coated polyimide device stack.....	82

LIST OF FIGURES (Continued)

<u>Figure</u>	<u>Page</u>
4.13 Contact angle measurements on gold surfaces.....	83
4.14 Contact angle values for gold surface treatments.....	83
4.15 Scratch tests on gold-coated polyimide.....	86
5.1 Sensor layout and initial masks.....	90
5.2 Sensors at multiple stages of processing.....	96
5.3 Ag and Au sidewalls after wet etch.....	102
5.4 Pt/Ir sidewalls after liftoff processing.....	104
5.5 Possible Pt/Ir redeposition during ion bombardment etching.....	105
5.6 SU-8 sidewalls after patterning.....	107
5.7 Effect of SU-8 on bending performance.....	108
5.8 Output current as a function of glucose concentration.....	110
5.9 Electrical resistance change after repeated bending for devices without GOx or PFSA.....	113
5.10 Images of electrodes before and after 62,140 bending cycles.....	113
7.1 Open-pore cubic network of cylinders.....	125
7.2 Uncoated and Al ₂ O ₃ coated CNC aerogels, with TEM of individual fibers.....	130
7.3 EPMA Al ₂ O ₃ thickness profiles compared with predicted.....	131
7.4 SEM of fractured, Al ₂ O ₃ coated aerogels.....	132
7.5 Modeled vs. observed Al ₂ O ₃ thickness profiles.....	133

LIST OF TABLES

<u>Table</u>	<u>Page</u>
4.1 Gel-Pak evaluation.....	62
4.2 Sample preparations using Al ₂ O ₃	78
4.3 Contact angle measurements on polyimide surfaces.....	84
4.4 Contact angle measurements on gold surfaces.....	81
5.1 Process flow for sensor fabrication.....	95
5.2 Wet etch masking recipe.....	102
5.3 Liftoff patterning recipe.....	103
5.4 SU-8 recipe for polyimide.....	106
7.1 ALD parameters for Al ₂ O ₃ deposition in CNC aerogels.....	129

1. Introduction

The modern electronics industry is under constant pressure to produce smaller, faster, and more convenient devices. These demands require a variety of innovative solutions, lately including a shift away from the silicon technologies that have been the core of the industry for most of its existence. Flexible electronics represent one such exciting departure from conventional devices, with promising applications including flexible displays [1], wearable electronics [2], and other mutable applications not compatible with a rigid device construction.

Implantable biomedical devices can especially benefit from a flexible construction. The ability to move and deform with a moving body allows application in locations where rigid devices would not be practical while reducing discomfort for patients. Sensors are particularly location-dependent and potentially intrusive, which has motivated development of flexible electronics for biosensing applications. Such applications range from simple, single-function devices to entire self-contained feedback systems intended to replicate natural homeostatic functions in the body. The latter represents the category of the current work.

The intention of this work is to apply flexible processing techniques to move toward the construction of an artificial endocrine pancreas that would take over the natural pancreas's primary role of regulating blood sugar levels within the human body. The necessary functions of such a device can be broken into four broad categories. First, it must be able to accurately detect and constantly monitor glucose concentration in the bloodstream, converting glucose levels into a measurable signal.

Second, it must be able to dispense insulin or glucagon to raise or lower that concentration, respectively. Third, it must be capable of deciding on its own when each action is necessary, and to what extent. Fourth, it must be able to record its functioning and communicate with external devices. Obviously, the consequences of device failure are high, and thus such a device requires a high level of reliability in all of these tasks.

This work does not intend to address all of the functions described above, and instead focuses on the ability to detect glucose levels in order to gather the information necessary for an artificial pancreas to function. This work takes a novel approach to this problem by integrating this function with the actual delivery method for glucose regulation hormones. Modern artificial pancreas technologies require a minimum of two separate insertion points, with some applications involving up to four [3]. This work details the fabrication of a sensor directly on the hormone delivery catheter itself, intending to reduce both the overall cost and number of separate insertion points required for the final product.

There are several significant challenges to the construction of an integrated sensor and catheter. First, the final sensor must take a cylindrical rather than a planar form, which introduces a number of processing difficulties. Second, the sensor must bend and flex as a catheter would, introducing additional reliability concerns and further process limitations. Third, the sensor must of course be biocompatible, limiting choice of materials and processes. Fourth, the sensor must actually perform its intended function of converting glucose concentration into a detectable signal, and

fifth, it must be able to communicate this signal to an appropriate control system. This work details the theory, development, and optimization of a process to fabricate glucose sensing and hormone delivery catheters that meet these requirements, along with the physical, chemical, and electrical characterization of the resulting devices. The organization of this thesis is given below.

Chapter 2 begins by motivating the need for glucose sensing and giving an overview of the history of devices created to address this need. The operating principles of the device created in the current work are then described, followed by a brief history of the flexible electronics industry and a description of associated theory and processing challenges in order to motivate the experiments in later chapters. Chapter 3 then provides a description of the materials and methods applied in the current work.

Chapter 4 describes experiments performed to establish a foundation for sensor fabrication that can withstand a curvature radius of approximately 0.25 mm. Initially, aluminum oxide (Al_2O_3) deposited via atomic layer deposition (ALD) was explored as an adhesion layer between sputtered titanium (Ti) and polyimide (PI). This material appeared to be unsuitable for the extreme bending radius used in the current work. Chapter 4 continues by exploring options to avoid usage of a failure-prone Al_2O_3 adhesive interlayer, arriving on the use of gold-coated polyimide as a solid foundation for device fabrication.

Having established a reliable substrate, Chapter 5 describes the design and fabrication process developed to implement the operating principles described in

Chapter 2, including data collected from experiments performed as part of process optimization. Chapter 6 summarizes recommendations for future work suggested by the observations in Chapters 4 and 5.

Finally, Chapter 7 is presented primarily as a self-contained work, detailing the modeling of ALD penetration into porous substrates. The work in this chapter extends existing ALD modeling techniques to apply to deposition within aerogel geometries, which would be useful for a variety of applications in the electronics industry as well as other fields. Modeled coating thickness profiles are compared to experimental observations, and the two are found to agree well enough to encourage further development and extension of this technique. Some possible avenues for such future work are discussed.

2. Background

Section 1 of this chapter motivates the need for glucose sensing and gives an overview of the history of devices created to address this need. Section 2 describes the operating principles of the device created in the current work. Section 3 gives a brief history of the flexible electronics industry, and Section 4 provides a description of the theory and processing challenges associated with flexible electronics.

2.1 Glucose sensing: motivation and history

Diabetes, formally called diabetes mellitus, is a common metabolic disease that produces dangerously elevated blood sugar concentration. Three types of the disease exist. Type 1 diabetes, also known as insulin-dependent diabetes mellitus (IDDM), represents a failure of the pancreas to produce sufficient insulin and typically requires sufferers to inject supplemental insulin. Type 2 diabetes, or non-insulin-dependent diabetes mellitus (NIDDM), describes the failure of cells in the body to respond appropriately to naturally-produced insulin. Gestational diabetes represents a third form of the disease, wherein elevated blood sugar levels appear during pregnancy. Both types 1 and 2 diabetes are chronic conditions that currently have no cure, though medication exists to manage type 2 diabetes [4].

According to the Centers for Disease Control and Prevention (CDC) in a report released 26 January 2011 [5], Diabetes affects approximately 25.8 million people in the United States, representing 8.3% of the total population. All forms of diabetes can cause serious complications, and the CDC indicates that diabetes was the leading cause of kidney failure, non-traumatic lower-limb amputations, and new cases of

blindness in the United States in 2010. Diabetes remains a major cause of heart disease and stroke, and is the seventh leading cause of death in the United States at the time of this writing [6].

Facts like these establish a clear need for technology to combat the effects of diabetes. Glucose represents the most common form of blood sugar [7], thus motivating advancement of glucose sensing technology for clinical application. The remainder of this section briefly describes the history of such technologies in order to set the context of the current work.

2.1.1 Point glucose monitoring

Leland Clark and Champ Lyons at the Medical College of Alabama developed the first significant glucose sensing technology, the glucose enzyme electrode, in 1962 [8, 9]. These devices relied on a thin layer of glucose oxidase to catalyze the oxidization of glucose to hydrogen peroxide, which generated a measurable current when applied to an electrode [9]. Hospitals did not widely adopt this technology, however, instead continuing to use reagent-impregnated strips that would change color based on glucose concentration. Measurement resolution of the color change technology was only as good as the user's ability to match the color of a strip to that on a chart. Quantitative techniques did not see widespread usage until Anton H. Clemens developed the portable Ames Reflectance Meter in 1971, which provided an analytic method of measuring this color change [10, 11].

Studies first examined the effectiveness of home glucose monitoring for type 1 diabetes in 1978. These and other work that followed confirmed that home glucose

monitoring was effective at controlling blood glucose levels and did so in a way that patients found acceptable [12-16]. In 1986, the American Diabetes Association, the Food and Drug Administration, and the National Institutes of Health issued a combined statement recommending home glucose monitoring for a wide range of applications, including pregnancies complicated by diabetes and individuals prone to hypoglycemia who did not experience the usual warning symptoms [17].

Self-monitoring of glucose levels in patients with type 2 diabetes has not shown the same beneficial effects as it has in patients with type 1 diabetes [18-21]. Regardless, the National Institute for Clinical Excellence (NICE) still recommends self-monitoring for patients with type 2 diabetes in several situations, such as to ensure safety during activities like driving [22]. The intent of the current work is to move toward providing all functions of the endocrine pancreas artificially, thus primarily targeting patients with type 1 diabetes; however, the recommendation from NICE suggests that the technology developed herein may be useful for home glucose monitoring for type 2 diabetes as well.

2.1.2 Continuous glucose monitoring

Technologies like color-changing strips and the Ames Reflectance Meter require finger-prick blood samples to work, giving information about glucose levels only for isolated points in time. Recent research has explored glucose sensing on a continual basis in order to collect data about the direction, magnitude, duration, frequency, and possible causes of fluctuations in glucose concentration [11]. Literature refers to this approach as constant or continuous glucose monitoring, abbreviated in either case as

CGM [23]. Collection of this additional data makes immediate, intensive therapy possible, which research has shown to be effective in delaying the onset and slowing the progression of some of the most serious effects of type 1 diabetes including ocular lesions, nephropathy, and neuropathy. These results have held across a range of populations [24], indicating the clinical importance of continuous glucose sensing technologies. A range of continuous glucose sensing methods now exist, each with their own benefits and drawbacks. Figure 2.1 presents an overview of the technologies currently in use or under investigation for glucose sensing in general, and indicates the field of the current work.

Every successful continuous glucose sensing technology must meet a particular set of basic requirements. First, it must be selective for glucose and must give a fast and predictable response to changes in glucose concentration, meaning that the sensing mechanism must be reversible and repeatable. Second, it must continue to provide this response for an extended period of operation, meaning that it must not degrade rapidly. Third, the sensor must exist in a way that is acceptable to the patient, meaning that it should be minimally invasive and should not require much effort from the user. Finally, production must be repeatable and easy enough to be practical [11]. Each technology in Figure 2.1 accomplishes these objectives to some degree, and though it is beyond the scope of this work to describe each in detail, Figure 2.1 is useful in setting the context of the current work.

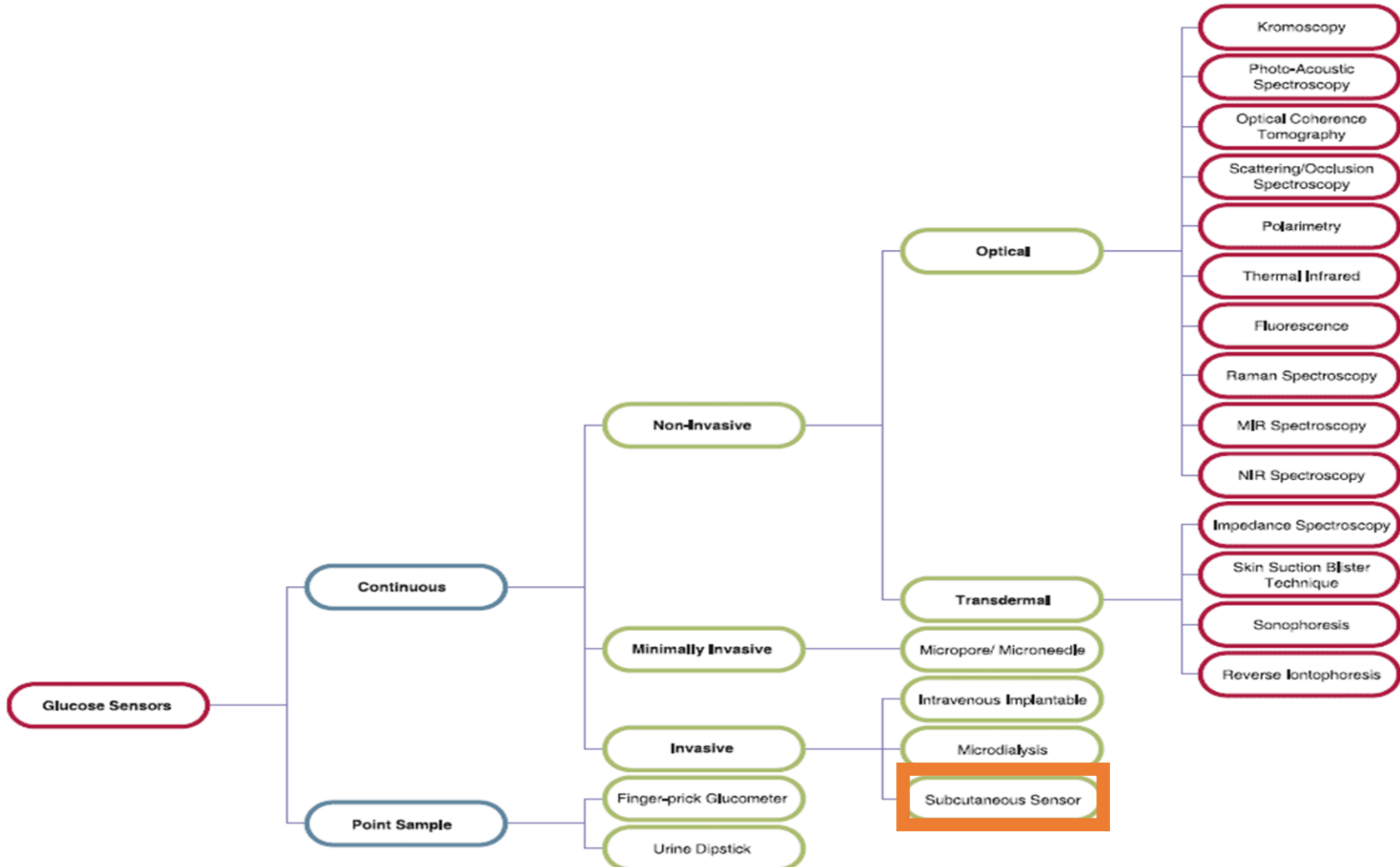


Figure 2.1: Glucose sensing technologies under development, reproduced from [11]. Box added to indicate the category of this work.

2.2 Device working principles

Many modern devices, including the one developed in the current work, operate on the same basic principle as Clark and Lyon's original device from 1962: a layer of glucose oxidase reacts with glucose to produce gluconic acid and hydrogen peroxide, the latter of which is then oxidized at a catalytic electrode to produce a measurable current [9]. This section provides a high-level overview using an equivalent circuit model in Section 2.2.1, and then presents the details of the systems used to achieve and enhance this process in Sections 2.2.2 – 2.2.6.

2.2.1 Equivalent circuit model

A high-level understanding of the developed sensor is obtainable from the simple equivalent circuit model displayed in Figure 2.2.

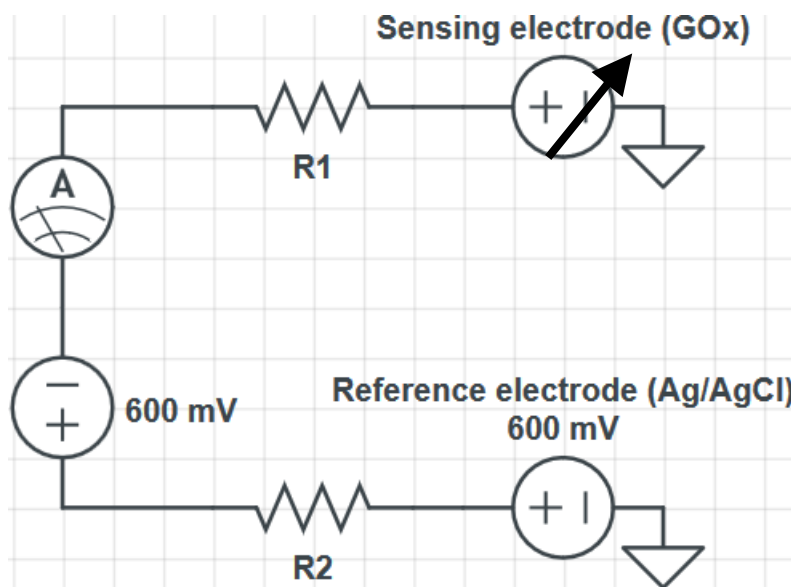


Figure 2.2: Equivalent circuit model for the developed glucose sensor. Only the actual electrodes and traces are actually implanted.

Any metals in contact with aqueous ions, such as those dissolved in subcutaneous fluid, will generate an electrochemical potential. Electrodes in contact with these fluids are thus modeled here as voltage sources. The electrochemical potential at the sensing electrode is modeled as a variable voltage source, controlled by glucose concentration via the mechanism described previously. The reference electrode is constructed to generate a known potential (0.6 V) between the subcutaneous fluid and the rest of the circuit, providing a steady reference voltage. The reference electrode is thus modeled as a constant voltage source. This reference potential is balanced by an external constant voltage source, meaning that any current flow observed through the external ammeter is driven by the electrochemical potential at the sensing electrode. Resistances R_1 and R_2 represent the combined effect of trace resistance, contact resistance with external electronics, and contact resistance with subcutaneous fluid for the sensing and reference electrodes, respectively. Finally, signal ground is considered to be at the subcutaneous fluid itself, where current is carried by redox reactions with aqueous species and, in the case of the reference electrode, reactions within the electrode material itself. The mechanisms by which each electrode functions are described in further detail in the following sections.

Figure 2.3 presents a cross-sectional schematic representation of the actual device layers that carry out the functions described by this equivalent circuit model. The remainder of Section 2.2 will reference this figure often.

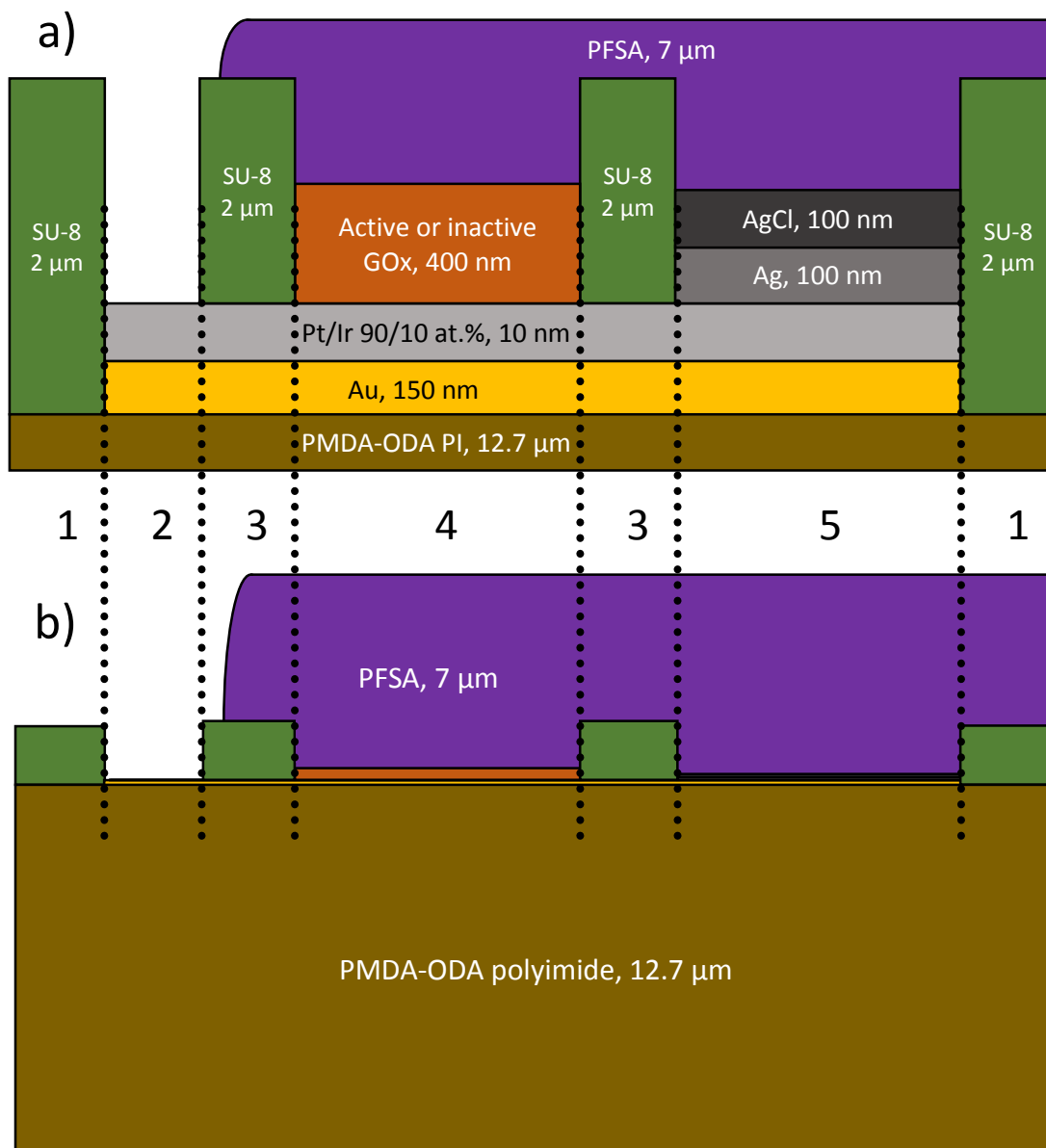


Figure 2.3: Cross-sectional schematic representation of layers in the device developed in the current work. Horizontal spacing is not to scale, and serves only to separate device sections for the purposes of illustration. This drawing does not represent physical device layout, only material stacks. A final silicone layer, not shown, may also be applied on top of PFSA in future work.

- a) Functional device layers expanded for visibility.
 b) All device layers shown to scale vertically.

Numbered regions: 1) passivated polyimide, 2) contact pads, 3) passivated traces, 4) sensing electrode, and 5) reference electrode.

2.2.2 Glucose oxidase for glucose detection

Keilin & Hartree in 1948 first suggested the use of glucose oxidase (GOx) to determine the glucose concentration of biological compounds [25]. Today, GOx is the most widely employed enzyme as an analytical reagent due first to its utility in analyzing glucose, a common analyte of interest in biochemistry and other fields, and second to the low cost and high stability of the glucose/GOx system that makes it a convenient model for development of new analytical methods [26].

GOx works together with its cofactor, flavin adenine dinucleotide (FAD), to catalyze the oxidation of β -D-glucose into D-glucono-1,5-lactone, which can then hydrolyze to gluconic acid. The oxidation of β -D-glucose occurs by reducing FAD to FADH₂, which molecular oxygen (O₂) then oxidizes to produce FAD and hydrogen peroxide (H₂O₂). H₂O₂ molecules then decompose, partially returning to O₂ and partially converting to water. This process produces excess electrons, and when oxidation occurs at the surface of an electrode, these electrons will produce a measurable current through that electrode [27]. Biasing that electrode will further encourage decomposition of H₂O₂, increasing the likelihood of H₂O₂ decomposition on contact. The decomposition of H₂O₂ itself is catalyzed by many transition metals, including platinum, gold, and silver [28]; fabricating an electrode from a catalytic material ensures that the majority of these reactions occur at the electrode surface, thereby generating a consistent current. This is the primary mechanism by which the current device, and many others, convert glucose concentration into electric current.

Region 4 of Figure 2.3 represents the device stack responsible for this primary sensing mechanism in our device.

2.2.3 Inactivated GOx to enhance selectivity

Glucose oxidase itself is highly selective to glucose (specifically β -glucose) [25, 29], but the electrostatic potential used to oxidize peroxide at the platinum electrode surface, 0.6 V relative to a reference electrode in contact with the solution, will also cause the oxidation of other species such as acetaminophen [30]. Care is necessary to ensure that these other signals are not confused with the current resulting from peroxide oxidation, which is produced by glucose oxidation. In our device, an electrode covered with GOx that is no longer catalytically active, referred to as inactivated GOx (iGOx), mirrors every GOx-coated electrode at the same implanted depth. GOx can be inactivated multiple ways, including UV exposure [31], thermal processing [32], chemical interaction [33, 34], and ultrasonic treatment [35]. Ideally, inactivation will completely remove the glucose-dependent signal while not altering any signals that are independent of the presence of glucose. iGOx should have a similar diffusivity to that of active GOx, and thus should ensure the same flux of potential interferants, or chemical species that may also create an oxidation current, to the electrode pad in both active and inactive GOx pads. Subtracting the signal of an iGOx electrode from that of its paired GOx electrode should then reduce sensor noise and drift by ensuring that only the actual glucose-dependent signal component remains in any significant magnitude. Region 4 in Figure 2.3 represents the stack responsible for this function in our device as well as the active sensor described

above, as fabrication of the inactivated working electrodes mirrors that of the active GOx electrodes as closely as possible.

2.2.4 Diffusion barrier to enhance linearity

According to the Mayo Clinic, normal glucose concentration in human blood ranges from 5-10 mM (90-180 mg/dL) [36]. Glucose sensors for clinical application are typically designed to respond to glucose levels from 0 to at least 20 mM (360 mg/dL) to include hypo- and hyperglycemic patients, ideally producing a linear relationship between glucose concentration and output current over this entire range [37–39]. The current work examined linearity from 0 to 30 mM (540 mg/dL) glucose concentration in order to give a more complete description of glucose levels even in extremely hyperglycemic cases. To ensure that signal from our sensor did not saturate from an overabundance of glucose within this range, a porous diffusion barrier was applied on top of the GOx layer to reduce the flux of glucose to the electrode surface, effectively causing glucose concentration at the electrode to be some fraction of that at the surface of the diffusion barrier. Ideally, this barrier will not significantly reduce the diffusion of molecular oxygen so that the desired redox reactions can continue at a rate determined solely by glucose supply. Applying such a barrier reduces overall signal by limiting total glucose and oxygen concentrations at the sensor, however, creating a tradeoff between linearity and overall signal magnitude.

Diffusion barriers have also been shown to be useful in limiting the effect of “poisoning” or “fouling” at the working (GOx) electrode, where other chemical species adsorb onto the metal surface and block electron exchange [23]. Further,

diffusion barriers such as perfluorosulfonic acid (PFSA) have been shown to enhance selectivity for glucose over potential interferants such as acetaminophen [30], and it is expected that the application of such a barrier can also protect against mechanical abrasion.

Work performed by Chris Durgan and Dr. Xiaosong Du explored diffusion barrier materials including PFSA, sulfonated poly-ether-ether-ketone (sPEEK), polydimethylsiloxane (PDMS), and combinations thereof. The optimal composition for this layer is still being determined, though PFSA layers of 7 μm thickness appear to be the preferred solution at the time of this writing. The final diffusion barrier material will be deposited across the entire device surface except for the contact pads, as illustrated in Figure 2.3b.

2.2.5 Silver / silver chloride reference electrode

To maintain a reliable glucose-dependent signal, it is necessary to maintain a constant electrochemical reference potential for the sensing electrodes. A common system used for this purpose is the silver / silver chloride (SSC) electrode [40, 41]. The steady state potential of the silver / silver chloride reaction,



is well known and relatively constant for a known chloride concentration. This potential, E , is expressed by the Nernst equation

$$E = E^0 - 2.303 \left(\frac{RT}{nF} \right) \log_{10} [\text{Cl}^-]^\alpha \quad (2.2)$$

where E^0 is the electrode standard potential (+0.22233 V for Ag/AgCl [42]), n is the number of electrons involved in the redox reaction, R is the molar gas constant

(8.31451 J/(K*mol)), T is the absolute temperature, F is the Faraday constant (96,485.33665 C/mol), $[Cl^-]$ is the concentration of free chloride ions, and α is the chloride ion activity coefficient [43]. Eq. 2.2 can be simplified using normal human body temperature, $T = 37$ C; using $n = 1$ as shown in Eq. 2.1; and by assuming a low chloride concentration and ideal solution behavior, in which case $\alpha = 1$. Using these simplifications and values for the appropriate constants, Eq. 2.2 simplifies to

$$E = E^0 - 87.56 \log_{10} [Cl^-] \quad (2.3)$$

which is dependent only on the logarithm of chloride concentration. Chloride is an important electrolyte in human blood, and chloride concentration is normally maintained within a relatively narrow range (normally 96-106 mM) [44]. Thus, the silver/silver chloride system produces a relatively constant potential and is thus ideal for application as a reference electrode for biological implementation. All current CGM systems use SSC electrodes in this manner [23]. Region 5 of Figure 2.3 represents the region that functions as an SSC electrode in our device.

2.2.6 Passivation and microstructure formation

Most electrical devices require some form of protection from their environment. Device layers applied for this purpose are known as passivation layers. Devices presented in the current work benefit from passivation in multiple ways, using SU-8 polymer obtained from MicroChem Corporation as a primary passivation material. First, chemical passivation of all implanted regions that do not require exposure to subcutaneous fluid will reduce the possibility of chemical species undergoing redox reactions along the electrode traces. These reactions would increase the ratio of non-

glucose-specific current to glucose-specific current. Ideally, any signal generated by this mechanism would cancel out when subtracting the inactive electrode signal from the active electrode signal; in practice, reducing overall non-glucose-dependent signal should improve accuracy by reducing the amount of correction necessary in the first place.

A second benefit of passivation is that it is expected that electrically isolating traces from subcutaneous fluids as much as possible will reduce noise from direct conduction between traces or other electrical sources in the body, thus further increasing signal-to-noise ratio.

A third reason is that a passivation layer can protect device layers from mechanical damage, such as abrasion caused by movement of the sensor inside the body. Tensile or compressive mechanical stresses from device flexion can also be neutralized by an overlying layer, as discussed Section 2.4.3.

The SU-8 passivation layer also served to create “wells” to facilitate deposition of GOx and iGOx, defining precise edges for GOx deposition as addressed in Chapter 3.1.5.

Regions 1 and 3 in Figure 2.3 represent the device regions in which SU-8 is applied. This includes everywhere that direct exposure to subcutaneous fluids or outside electrical contact is not required.

2.3 Brief history of flexible electronics

To paraphrase I-Chun Cheng in *Flexible Electronics: Materials and Applications*, any material is flexible if it is thin enough [45]. One of the first

applications of this principle in the electronics industry was in the 1960s, when the first flexible photovoltaic arrays were assembled by thinning crystalline silicon wafers to approximately 100 μm and then assembling them on a plastic substrate [46–48]. Flexible TFTs were first assembled around the same time [49, 50]. Solar cells continued to drive the development of flexible electronic technology through the early 1980s [45, 51–53], when reel-to-reel fabrication was demonstrated on flexible steel [54] and organic polymer substrates [55].

The mid-1980s saw the rise of the active-matrix liquid-crystal display (AMLCD) industry in Japan, which was made possible in part by adopting plasma-enhanced chemical vapor deposition (PECVD) processes developed for use in fabrication of hydrogenated amorphous silicon (a-Si:H) solar cells [45]. Other common electronics processing methods were adopted by flexible electronics researchers, eventually allowing entire TFT-based circuits to be fabricated on polyimide in 1994 [31]. Further advances were reported throughout the 1990s as research into flexible displays became a topic of intense interest [56–58]. Recently, Samsung, LG, and others have demonstrated flexible displays for such applications as curved or entirely flexible watches [59], smartphones [60, 61], and even televisions [62, 63].

2.4 Theory of flexible electronics

Fabrication processes for flexible electronics must address some different concerns than rigid fabrication processes due to the extra mechanical strain they are

typically expected to withstand. This section presents some of the theory behind those concerns.

2.4.1 Internal stresses

In addition to stress applied from external sources, such as flexion or tension applied to the finished device, stresses can develop within a device during fabrication such that devices fail, or are primed to fail, before construction is even complete.

Device films are typically deposited at elevated temperatures. If coefficients of thermal expansion (CTE) differ greatly between materials in the device stack, stress fields will develop upon cooling. For rigid substrates, the strength of the substrate (as defined by the ratio of stress (in units of pressure) to strain (unitless), termed the Young's modulus, multiplied by thickness [45]) is always much greater than that of the device layers, causing thermally induced stress to occur almost exclusively in the film rather than the substrate. In such cases, stress formation usually does not cause overall device deformation and thus does not become problematic except in special or extreme cases [64]. Substrates with strengths comparable to that of deposited films behave differently, however, sharing induced stress and bending so that the device surface becomes either concave (due to tensile stress in the deposited film) or convex (due to compressive stress). Strong rigidizing solutions can mitigate this effect as long as the devices remain adhered, but induced stress can even then lead to significant changes in the planar dimensions of a flexible substrate and thus cause alignment errors in masking processes [45]. Other ways to mitigate this phenomenon

include choosing materials with similar CTEs or keeping overall process temperatures low, though these options are often severely limiting from a fabrication standpoint.

In addition to thermal stress from CTE mismatch, a certain amount of built-in stress may occur depending on the deposition process used. Typically, physical vapor deposition (PVD, discussed in Chapter 3.2.1) processes involve material arriving at a substrate with a high kinetic energy, which will tend to introduce a compressive stress by forcing arriving material into the midst of immobile and already closely-packed atoms. The amount of compressive stress induced tends to be directly related to the energy of ion bombardment on the growing film [65]. Stress induced in this manner can be detrimental for the same reasons as thermal stress.

Polymeric substrates like polyimide face an additional challenge. Water absorption can cause significant dimensional changes in a process referred to as hydrolytic expansion [45]. Further, incorporated water and potentially other chemicals will outgas in a vacuum environment, potentially interfering with deposition or other processes. Baking a polymeric substrate can successfully drive out water, reducing the potential for hydrolytic shrinking under vacuum and improving surface energy for adhesion [66]. However, polymeric substrates can then expand when reintroduced to water vapor in air, creating interfacial strain.

It is important to control internal stress from any source mentioned above, as internal stress influences all other coating properties, including adhesive strength, microhardness, wear resistance, and in some cases, electrical behavior [65, 67]. Care was taken to maintain low process temperatures in the current work, but strain

development was not examined in detail. Instead, the current work relied on literature and experimental observation for evidence that fabrication using the chosen materials and processes was feasible. Future work may explore strain engineering in more detail, however, as addressed in Chapter 6.2.

2.4.2 Adhesion and cohesion

Mechanical strain, either internal from the sources described previously or external from device flexion or mechanical abuse, is resisted and distributed by the cohesive strength of each layer in a device and the adhesive strength of the interfaces between them. Cohesion allows sharing of strain throughout a layer, while adhesion allows sharing of strain between layers. Crack formation ultimately results from cohesive failure, but stress can be concentrated and cracks initiated by adhesive failure. Typically, adhesive energy between dissimilar layers is much lower than cohesive energy within each layer, and thus engineering to increase adhesion between layers is a major subject of research in the field of flexible electronics.

The phenomenon of adhesion is addressed by a number of theories, including mechanical interlocking, electronic bonding, interphase mixing, adsorption, diffusion, and chemical bonding, and the relative importance of each theory depends on the system under examination [68]. Adsorption theory describes the achievement of intimate contact between surfaces, which is necessary for other mechanisms to begin to take effect. Due to this fact and the current work's lack of significant interlocking mechanical structures, diffusion or interphase formation, and electronic or chemical bonds at material interfaces, adsorption theory was considered to be the most useful

for describing the interface between cured polyimide film and deposited materials. Similar assumptions are commonly made for polymeric substrates in literature [69–73].

Adsorption theory, also called wettability, acid-base theory, or thermodynamic theory, is generally attributed to Sharpe and Schonhorn [74] and is currently the most widely used approach in adhesion science [68]. This theory describes interatomic and intermolecular forces at an interface as the source of adhesion, most commonly focusing on van der Waals and Lewis acid-base interactions. These interactions can then be related to fundamental thermodynamic quantities such as surface free energy [68], which can in turn be quantified by a variety of methods including observation of wettability via contact angle measurement (discussed in Chapter 3.5.1). Theoretically, the relation between contact angle and surface energy is given by Young’s Equation,

$$\gamma_{SL} + \gamma_{LG}\cos\theta_C = \gamma_{SG} \quad (2.4)$$

where γ_{SL} , γ_{SG} , and γ_{LG} are the interfacial tensions at each interface between solid (S), liquid (L, in this case water) and gas (G, in this case air), and θ_C is the resulting contact angle <the measurement of surface energy of polymers, Hansen>. This justifies use of contact angle measurements to predict the effect of surface treatments on adhesive strength between a substrate and a deposited layer.

Other mechanisms than adsorption theory do factor in to overall adhesion, so contact angle measurements are useful but do not tell the entire story of adhesion or device durability. Mechanical fatigue testing allows direct observation of crack formation using optical and electrical measurements. Compressive stress encourages

delamination and buckling to relieve strain, which is resisted by good adhesive coupling between layers [45]. Thus, using mechanical testing to induce compressive stress is an effective way to measure interfacial adhesion. Compressive stress can be applied by bending a metallized sample such that the metallized face is on the interior of a bend, which was implemented to investigate device durability in the current work. The methods of bend testing used in this work is described in Chapter 3.5.3.

2.4.3 Design for flexible electronics

As discussed, bending a flexible device induces tensile strain on the outside face and compressive stress in the inside face of the bend. Between these two faces exists a continuous stress gradient, including a plane where tensile or compressive stress is effectively neutralized. This region is not always exactly in the middle of the substrate, and is instead determined by the relative strength of each device layer. Burying active devices layers between layers of equal strength, and therefore in or near this stress-neutral plane, is a common technique for extending the lifetime of flexible devices [45, 75, 76]. Devices developed in the current work are expected to benefit somewhat from this effect, though device layers were not calibrated to place active layers specifically in the stress-neutral plane as final device layers are still under investigation by OSU Chemical Engineering and Pacific Diabetes Technologies.

Careful engineering of device geometry can avoid stress buildup and thus increase device lifetime. The guidelines given below are a compilation of advice

given in [77–80], and similar advice can be found in design guides for flexible electronics and interconnects published elsewhere.

Stress buildup tends to occur wherever device makeup changes, including changes in shape or composition. Ideally, such changes in device construction will occur outside of the flexible area, avoiding external mechanical stressing altogether. The entire device produced by the current work must bend, however, making it impossible to apply this advice. Further, it is considered best for electrical traces to run perpendicular to the axis around which devices are being bent, describing an arc around the circumference of a cylinder rather than a line along its length. This was not possible for the current devices without utilizing complex device wrapping methods, such as a spiral wrapping and braiding technique used in literature [81]. Trace width is also desired to be at least 10 times the expected bend radius, which was not possible due to limited available surface area. These guidelines are mentioned here to illustrate why reliability challenges are a major concern for the current work.

Some guidelines that were conducive to application in the current work included use of rounded corners and gradual changes in line width, avoiding abrupt compositional changes. Further, trace width was maximized where possible in order to increase conductivity, decrease sensitivity to processing flaws, and reduce variation in surface coverage at any point along the device length. Finally, the top and bottom of the reference electrode were extended slightly beyond the ends of sensing electrodes, again attempting to reduce the amount of change (and, therefore, stress

buildup) at a single point along the length of the device. The resulting design is shown and discussed in Chapter 5.1.

3. Materials and Methods

A wide range of materials are used in the fabrication of flexible electronics, and these materials require an even wider range of processing methods to deposit, pattern, remove, or otherwise alter them. Section 1 of this chapter describes the materials relevant to the present work, organized by application. Section 2 covers the deposition technologies applied in the current work. Section 3 describes techniques used to pattern and etch deposited materials. Section 4 addresses some surface treatments used to modify these materials. Finally, Section 5 presents characterization methods.

3.1 Materials

A material is considered relevant to the current work only if it was considered for use or if it has been identified as potentially useful for future work. This excludes discussion of important substrates such as glass, steel, or semiconducting materials like amorphous hydrogenated silicon (a-Si:H) and indium-gallium-zinc-oxide (IGZO), all of which play significant roles in current flexible electronics research and industrial activity.

3.1.1 Substrates

Most materials become flexible once they are thin enough [45], but flexible substrates must generally be thicker than other layers in order to be mechanically stable, meaning that flexibility of the substrate material is a primary concern. Further, flex substrates must be chemically compatible with a range of process technologies and materials, requiring that they be relatively chemically inert. Many thin film

deposition technologies also require substrates to withstand vacuum pressures and high temperatures, which is particularly problematic for polymer substrates. Electrical and optical properties of flexible substrates are also important for many applications, but these did not significantly affect the current work.

Three materials were evaluated for use as substrates for the current work: biaxially-oriented polyethylene terephthalate (BoPET), liquid crystal polymer (LCP), and PMDA-ODA polyimide (PI). BoPET, commonly sold as Mylar, is often used as a carrier for flexible circuits and interconnects [82]. LCP, also sold as Vectran or Zenite, has been previously reported in flexible high-frequency devices that make use of its low dielectric constant [83]. PI is a robust plastic composed of chains of imide monomers that exists in many formulations. PMDA-ODA polyimide is generally the most well-established of these three classes of material in literature [84, 85] and was eventually chosen over the other materials for use in the current work. Chapter 4 provides a more complete motivation for this choice.

3.1.2 Rigidization

The need for rigidization is a concern unique to flexible electronics. Flexible substrates generally need to be kept rigid and planar throughout device fabrication unless using specialized equipment like that used in roll-to-roll fabrication techniques. This requirement is especially problematic in academic research labs that may not be able to justify the purchase of specialized industrial processing equipment. Therefore, the first problem that such a lab must overcome to deal with

flexible substrates is how to make a substrate planar and rigid for compatibility with existing process technologies.

Rigidization solutions are subject to a number of strict requirements. First, they must provide enough adhesion to maintain planarity throughout fabrication while still being weak enough, or able to become weak enough, to allow removal of the final product without causing damage. It is important to emphasize that the goal is planarity, rather than simple adhesion, as even small deviations from planarity can have significant effects on patterning or deposition processes that depend on a flat surface. Second, a rigidization solution must be chemically compatible with substances used in the fabrication process, including harsh chemicals used in etching and cleaning processes. Third, it must be physically compatible with the entire fabrication process, meaning that it must withstand the temperatures and pressures used without losing adhesion, applying too much strain from mismatched coefficients of thermal expansion (CTE), or outgassing, which can interfere with deposition processes and destroy planarity by creating bubbles beneath the substrate material.

Three approaches taken in literature to address rigidization specifically for PI substrates are formation of the PI film directly on a process-compatible rigid substrate [86–88], use of vacuum-compatible epoxies to attach pre-fabricated PI films to a rigid backing [87], and use of an adhesive interlayer between a pre-fabricated PI film and a rigid backing [89–92]. Direct deposition of a PI film on a rigid substrate has been reported to give better planarity for photomask registration when compared to the use of a vacuum-compatible adhesive epoxy [87], but requires the development of a

process for forming and curing the PI layer. While such processes are common in literature [66], the present work was completed using pre-fabricated PI films and employing the use of an adhesive interlayer. This decision was made to simplify the overall process, given that suitable PI films already exist on the market from providers such as DuPont (Kapton), UBE (Upilex), Saint-Gobain (Norton), and Caplinq (Linqtape).

The adhesive layer used for the majority of the current work is a solid, silicon-based film provided by Vichem under the name Gel-Pak DGL film. Gel-Pak was found to be chemically and physically process compatible, provided a proper adhesive strength, and succeeded in maintaining relative planarity in an affixed flexible substrate. A more detailed investigation of variants of Gel-Pak DGL film is presented in Chapter 4.

3.1.3 Conductive traces

No matter the construction of an electrical device, it must interact with other devices and the outside world. This generally requires conductive traces. The high aspect ratio (length \gg width or thickness) nature of many electrical traces leaves them vulnerable to small flaws along their length, allowing the damaging effects of bending to become more apparent for traces that span large distances. Conductive layers on flexible substrates must tolerate both compressive and tensile stress, and generally must not crack or otherwise lose their conductive properties even after repeated bending. The current work places metal traces toward the outside face of a tight radius of curvature, thus potentially introducing strong tensile stress. Ductility,

as the quality of being able to tolerate deformation under tensile stress without fracturing, thus served as a useful metric for selecting conductive layers.

Electrical traces are most commonly fabricated from metals due to their high electrical conductivity. Ductile metals such as gold, silver, copper, platinum, and titanium, listed in order of descending ductility [42], are especially useful for conductive traces in flexible electronics, though biocompatibility complicates the use of raw copper in biomedical devices [93]. The current work explored the use of titanium and gold as primary conductive layers, settling on gold for actual device construction. In each case, conduction was augmented by a thin 90/10 at.% platinum/iridium (Pt/Ir) layer intended primarily to catalyze H_2O_2 oxidation for glucose sensing. Silver was also selectively applied to create a reliable reference electrode. The electrochemical functions of silver and Pt/Ir are described in Chapter 2.2.

Conductive polymers are also appealing for their flexibility and can be viable design choices in situations where moderate resistivity is acceptable [94, 95]. Easy deposition by inkjet printing, discussed Section 3.2.3, is another motivating factor for the use of conductive polymers. Graphene [96, 97] and other two-dimensional conductors such as molybdenum disulfide [98–100] are also worth mentioning as conductive materials for flexible electronics due to their unique electrical and mechanical properties and, at least in the case of graphene, relative ease of deposition. These materials were not applied in the present work, but may be worth future investigation.

3.1.4 Adhesion promotion

As discussed in Chapter 2.4, adhesion presents a major obstacle to the fabrication of devices on inert substrates such as PI. In cases where two adjacent layers need not be in direct contact, adhesion between layers can be enhanced by the presence of an interlayer. The most common adhesion-promoting interlayers in literature for metals on polyimide are titanium [66, 101–103] and chromium [66, 101, 104, 105]. ALD-deposited aluminum oxide (Al_2O_3) has also been studied more recently as an adhesion promotion layer on polymeric substrates [106]. As chromium complicates biological applications due to potential allergy or toxicity [107, 108], titanium and Al_2O_3 are explored in the present work. Chapter 4 explores the use and effects of titanium and Al_2O_3 together.

Section 3.4 describes surface treatments that do not involve an interlayer to promote adhesion. Chapter 4 also experimentally explores some of these treatments in detail, concluding that no adhesive interlayer is necessary for the current work. Thus, no layer in final device construction was intended specifically as an adhesion layer, though the presence of gold does effectively enable deposition and adhesion of Pt/Ir.

3.1.5 Passivation

Completed electronic devices usually must be protected from their environment, as discussed in Chapter 2.2.5. Many flexible devices, especially polymer-based, are also sensitive to diffusion of water and other chemical species from the outside; this was expected, but not observed, to be a problem in the current work. Further, isolation or encapsulation layers can improve resistance to mechanical

stresses and abrasion. The current work investigated the use of Al_2O_3 and SU-8 polymer as passivation materials.

Thin layers of ceramics such as Al_2O_3 have been shown to be effective barriers to water diffusion when deposited by highly conformal methods such as ALD [109–112], a technique described in Section 3.2.2. ALD Al_2O_3 was initially intended to prevent water absorption in the substrate material in addition to its role in promoting adhesion, but was shown to be overall detrimental to device integrity as described in Chapter 4.

SU-8 polymer, provided by MicroChem Corporation, was applied to protect and electrically isolate metals while also forming physical “wells” to facilitate GOx deposition. As described in Chapter 5, SU-8 was found to provide sufficient flexibility, mechanical stability, and adhesion to PI once deposited by an optimized recipe.

3.2 Deposition methods

To construct a thin-film device, one must first be able to deliver the appropriate materials in an appropriate manner. The appropriate manner differs between materials and applications, and a range of technologies exist to address this.

3.2.1 Physical vapor deposition processes

Physical vapor deposition (PVD) is perhaps the most straightforward class of thin film deposition methods. Any technique that relies on sheer kinetic energy to achieve material deposition falls into this category, though the chemistry of a PVD process should not be assumed to be trivial.

Thermal evaporation is a straightforward and widely applied method to deposit materials that do not degrade under vacuum or at high temperatures. Essentially any material that will retain its desired properties through sublimation and desublimation is eligible for use in thermal evaporation. This requirement excludes most complex molecules and organics, but is well suited for elemental or amorphous materials.

This work used a Veeco thermal evaporation system to deposit silver for later partial chloridization in order to form a reference electrode. 50g of silver were placed in a tungsten boat and evaporated at approximately 10^{-6} Torr over a throw distance of approximately 4 inches, and samples were placed within a 3 in² area to ensure uniformity. Deposition rate and film thickness were monitored with a Maxtek, Inc. TM-350 Thickness Monitor quartz crystal microbalance (QCM) system. Evaporation temperature and ramp rate were not directly measured.

Another method of PVD, called sputtering, is to utilize plasma ion bombardment rather than thermal energy to eject source material. This process ejects source particles in the range of 4.0 to 10 eV, compared to 0.1 to 0.6 eV for thermal evaporation [113]. Generally, this higher ejection energy is expected to increase adhesion of the deposited layer, though this does not hold true in every case [113]. Also, the presence of a plasma between the source and substrate causes sputtered species to scatter multiple times before arriving at the substrate, causing sputter deposition to be less dependent on line-of-sight and therefore more conformal than thermal evaporation.

The current work used an AJA ATC Orion sputtering system to deposit both Pr/Ir and titanium using DC sputtering. Sputter power was 300W for Ti and 100 W for Pt/Ir. 5 mTorr argon gas was used in both cases, and deposition was performed after a 5 minute pre-sputter to clean the deposition target.

3.2.2 Atomic layer deposition

Rather than relying solely on kinetic energy, chemical vapor deposition (CVD) processes utilize chemical reactions to achieve material deposition. Usually, this requires formulating a compound that decomposes into a desired material under specific conditions. Such a material is called a precursor, and often several precursors exist for a given material. Many precursors are formed by joining atoms of the desired material to organic ligands; in the case of metal deposition, this deposition process is referred to as metal-organic chemical vapor deposition, or MOCVD. The resulting weak organometallic bonds will decompose on contact with a heated substrate, turning the ligands into gasses that can be pumped away while leaving the desired material behind.

Atomic layer deposition (ALD) is a particular form of CVD that has become the subject of intense interest since the late 90's [114–118]. Most CVD processes introduce precursors continually throughout the deposition process, causing continual film growth. ALD instead uses sequential pulses of at least two different reactants, taking advantage of self-limiting surface reactions to coat a surface with one monolayer of adsorbed species per pulse [114, 115, 117, 118]. This growth method provides superior conformality and film quality at the cost of low growth rates, hence

its recent application in deposition of ultra-thin high-k dielectrics for TFTs and MOS capacitors [116, 119]. A basic ALD setup includes a vacuum chamber, precursor containers, and computer-controlled valves to control the delivery of precursor material into the reaction chamber. A single ALD cycle begins by introducing one reactant to the reaction chamber. Ideally, this reactant adsorbs as a monolayer, replacing ligands at active sites such as -OH groups. The gaseous ligands released by this process are then purged along with remaining precursor material using an inert gas such as nitrogen, as utilized in this work. The second reactant is then pulsed into the chamber, where it combines with the first reactant, again replacing remaining ligands to form a single monolayer of the desired film and restoring original active groups to the surface, as present before the first pulse. The gaseous ligands released by this process are then purged with excess reactant in the same manner as the first purge. This cycle, illustrated in Figure 3.1, then repeats until the desired film thickness is achieved.

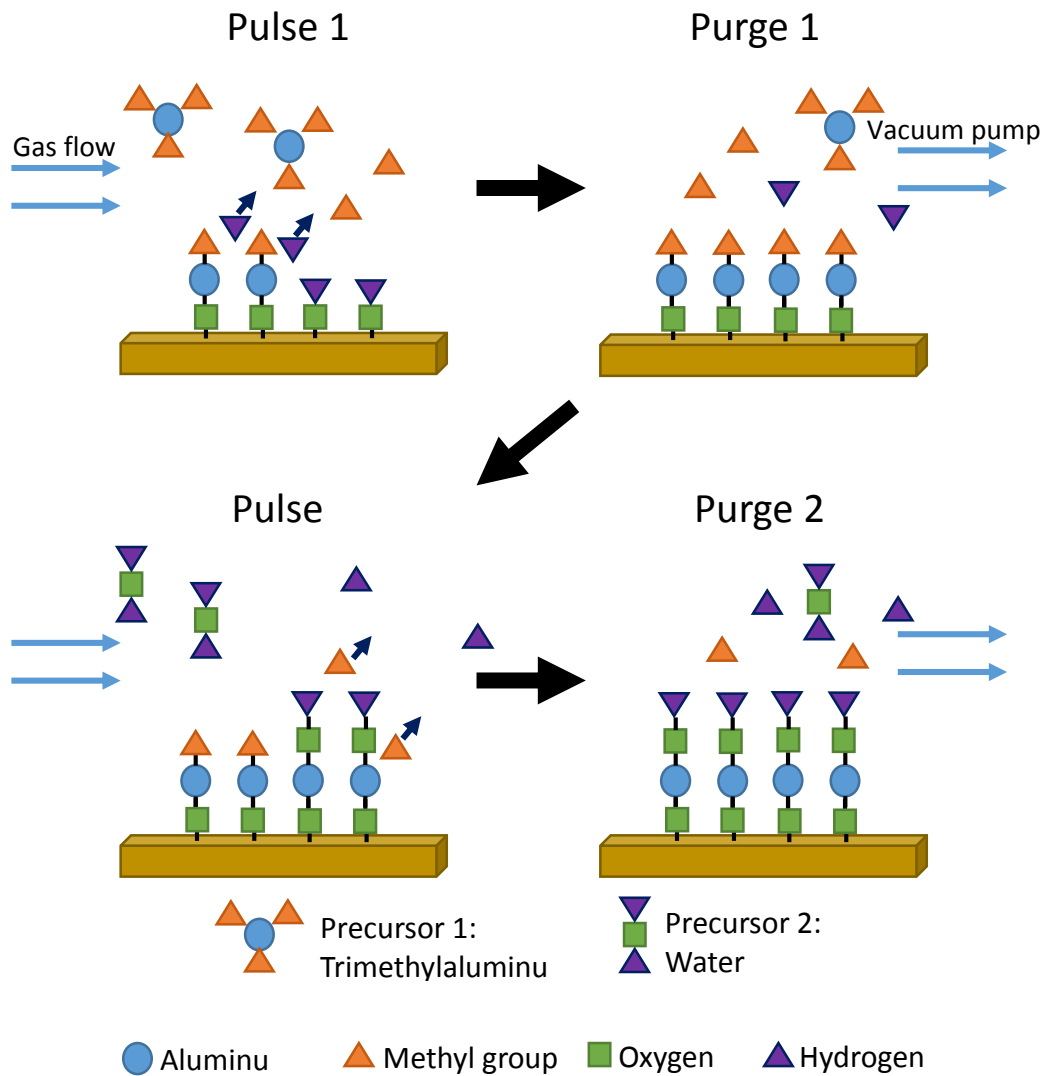


Figure 3.1: One ALD cycle, as explained in the text.

The basic sequence for an ALD cycle, then, is pulse reactant 1, purge reactant 1, pulse reactant 2, purge reactant 2. Typically, purge times must be much longer than pulse times to ensure that reactants meet nowhere besides the surface of the substrate; hot-wall reactors are often used to discourage precursor adsorption elsewhere in the reaction chamber for this reason. Purge times that are too short cause precursor materials to meet and react in the gas phase, causing unwanted CVD deposition on

the substrate and possibly elsewhere in the ALD system, while overly long purge times may allow adsorbed reactant on the substrate to desorb thus creating defects in the deposited layer. Each reactant pulse is calibrated to provide enough precursor material to coat a substrate thoroughly without adding extra reactant to be removed by the following purge. Precursors with slow reaction times or low reaction probabilities may require the addition of a “soak” or “exposure” step after pulsing, during which no precursor is introduced to or removed from the chamber in order to allow complete surface coverage before the next purge step. Occasionally, the ALD cycle can also be extended to include more than two reactants in order to create tertiary or quaternary systems.

3.2.3 Liquid-state deposition processes

Recent advances in solution processing and materials chemistry have allowed inkjet printing systems to become viable for microscale deposition of a wide range of materials, including polymers [95], metals from nanoparticle films [120], and graphene [121, 122]. When the application permits, direct printing of a material is often quicker and more cost-efficient than gas-phase methods, as printing wastes less material and generally does not require vacuum processing.

A number of microscale printing technologies exist, including thermal, electrodynamic, and piezoelectric printing mechanisms [123]. Printed features as small as 5 μm in width have been reported for semiconducting polymers utilizing pre-defined polyimide channels [123], facilitating the use of such technologies in microelectronics. The current work explored the use of electrohydrodynamic printing

(EDHP) to deposit glucose oxidase. EDHP works by setting up an electric field between the ink solution, biased using an electrode in the print needle, and the substrate or a conductive stage beneath it. The resulting electric force attempts to pull ink from the needle and is resisted by surface tension of the ink itself. This electric field can be modulated to create a droplet, then increased temporarily to defeat surface tension and dispense the single droplet, and reduced again to allow surface tension to form another droplet. This process can be repeated across a material in a desired pattern. Thermal annealing or vacuum desiccation is then used to remove ink solvents and solidify the deposited layer. . demonstrates patterns deposited using EDHP printing at OSU.

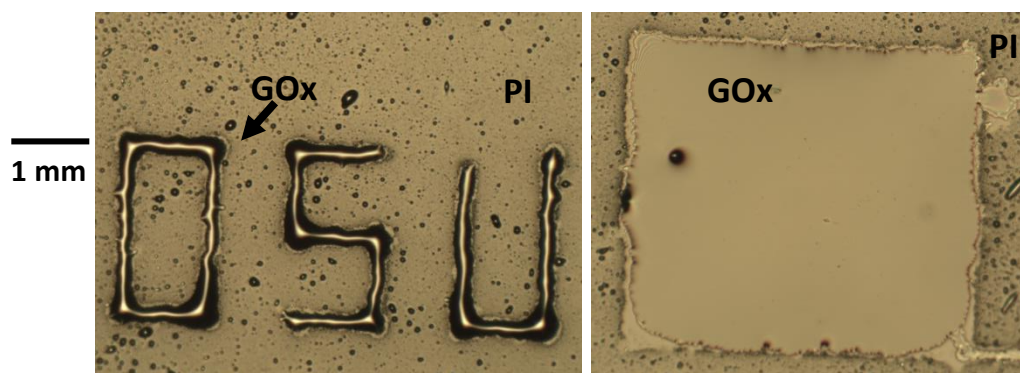


Figure 3.2: Optical images of glucose oxidase printed via EDHP. Printing and imaging performed by Chris Durgan of OSU Chemical Engineering.

Finally, spinning is a simple liquid-state deposition technique that is very common in semiconductor research and industry. Spinning refers to the process of dropping a liquid onto a substrate and then rapidly spinning that substrate, typically at several thousand RPM, in order to leverage centrifugal effects to spread the liquid and create a uniform layer. Typically, as in inkjet printing, the spun film is baked after

deposition to drive out solvents and create a stable, solid film. Layer thickness is varied by adjusting spin speed and solvent concentration. Spinning is attractive because of its simplicity, since it requires nothing more than a rotating chuck and perhaps a fume hood depending on the solvents used. The nature of this technique leaves it vulnerable to particles or deviations from planarity, however, which can create “trails” of imperfections radiating from the center of rotation. In addition, spinning tends to leave edge beads at the boundary of a substrate due to surface tension of the spun solution.

This work used spinning techniques to apply photoresist and diffusion barrier materials, discussed in the following section.

3.3 Patterning

Simply depositing layers of different material is rarely sufficient to make a useful device. This section will describe the methods used to pattern deposited layers in the present work.

3.3.1 Masking

Conceptually, the simplest way to pattern a material is to make sure that it is deposited in the desired pattern to begin with. For large design features and relatively nonconformal deposition methods, this can be done by simply placing a solid mask between the source material and substrate. The first iteration of devices in this project used a large minimum feature size, allowing the utilization of simple “shadow masks” of this type fabricated from stainless steel using a laser cutter. Available resources did not allow easy shadow mask alignment for a multi-layer process, however, and were

not able to provide better than approximately 300 μm minimum feature size, which was not sufficient for final device production. Advanced shadow masking techniques can dramatically improve resolution beyond 300 μm , but access to other processing capabilities made the pursuit of such techniques unnecessary for the current work.

Rather than fabricating a separate solid mask, it is also possible to deposit an easily patterned material directly on the surface of a substrate, allowing the formation of a mask on the device itself. This technique, known generally as lithography, improves resolution by clearly defining pattern edges and preventing unwanted deposition due to gaps between a solid mask and substrate. Lithographic processing is especially important for highly conformal deposition processes for this reason.

The most common type of resist is patterned using exposure to high-energy light, commonly in the ultraviolet (UV) range in order to make use of short wavelengths. These materials are called photoresists, and advanced photoresist materials can produce minimum feature sizes on the order of the wavelength of light to which they respond. Photoresist can be broadly divided into positive and negative resists depending on how they respond when exposed to UV radiation. UV exposure breaks chemical bonds within a positive resist, causing exposed regions to become soluble to a developer solution that preferentially dissolves exposed regions. Negative resists perform oppositely: they are soluble to developer as deposited, but become insoluble when exposed to UV. In this case, insolubility is the result of crosslinking between polymers resulting from input of thermal and photonic energy. Overall, the

photolithography process is fundamentally similar to that used to develop film photographs.

The current work applies both positive and negative photoresists. All patterning and mask aligning was performed on a Karl Suss MJB3 mask aligner with a 350W mercury-vapor lamp. Liftoff, wet-etch, and experiments with dry-etch processing used Shipley S1818 positive photoresist and a 4:1 solution of deionized (DI) water to Shipley 315 developer for pattern development. Acetone was used for non-selective removal of all S1818 as required in liftoff processing. Protection, electrical isolation, and well formation for glucose oxidase deposition used Microchem SU-8 negative photoresist and developer. Exact recipes are presented along with process optimization details in Chapter 5.2.

3.3.2 Etching

A resist mask can be used in the same manner as a shadow mask to create a pattern by selectively preventing adhesion between a deposited layer and the substrate. Using a resist in this way is known as liftoff processing, which is not technically an etch process, but achieves a similar result. Liftoff processing is performed by depositing and patterning a resist, depositing the desired material, and then removing the resist with an appropriate solvent. Ideally, material that has adhered to the resist will wash away while material deposited directly on the substrate will remain.

For materials with strong cohesive strength patterned in features placed close together, sometimes “bridging” between features can occur where resist washes away

from beneath the deposited material without removing the material itself. Also, in cases with poor adhesion between the deposited material and the substrate, unwanted material may drag desired material away as it washes off. Both of these faults are demonstrated in Figure 3.3. Further, liftoff processing generally results in the presence of ridges along pattern edges even in ideal cases. Limiting deposition on resist sidewalls can suppress these effects. This can be achieved by creating steep or negatively sloped sidewalls and using nonconformal deposition methods. Further, not all resists are compatible with all types of processing: resists must remain soluble – or somehow removable – after going through the deposition process, and should not outgas significantly during processing.

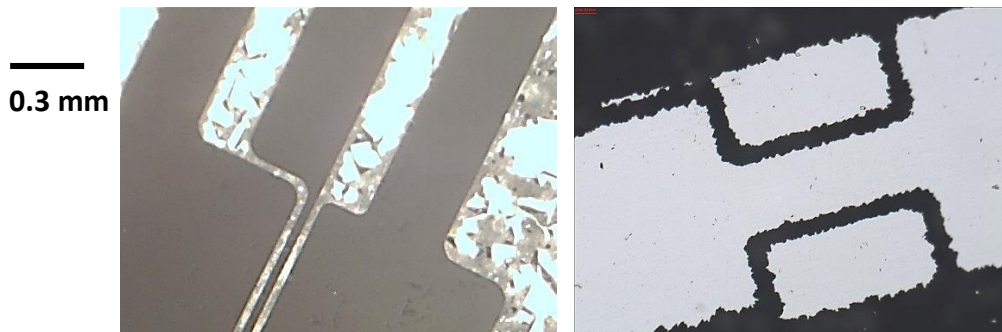


Figure 3.3: Optical images of problems in liftoff processing.

Left (backlit): Poor material removal and bridging between features intended to be isolated. Caused by poor adhesion of deposited material to liftoff resist.

Right: Removal of desired material. Caused by strong cohesion of deposited layer and weak adhesion of desired material to substrate.

Light shining through a contact photomask diffracts around pattern edges, exposing a slightly wider region than defined by the mask. The width of this region increases with depth in the resist, resulting in positively sloped sidewalls (sloping away from developed regions) for positive photoresists and negatively sloped

sidewalls (overhanging developed regions) for negative resists. This motivates the use of negative resists for liftoff processing in order to suppress sidewall coverage. SU-8, a negative photoresist applied elsewhere in this work, is difficult to remove once set, generally precluding its use without additional sacrificial layers or other novel techniques [124–126]. For the feature sizes and thin layers used in this project, a simple layer of S1818 positive resist performed sufficiently despite generating positively sloped sidewalls, and thus such novel techniques were not explored.

Most often, photoresists are used as etch masks instead of deposition masks. Etching can occur in two forms, wet or dry, depending on the material phase of the etchant used. Wet etching requires the least equipment, simply requiring a masked material to be submerged in an etchant bath long enough to remove exposed material. A wet etch process is accomplished by depositing the desired material as a uniform layer, depositing and patterning a resist, submersing the system in an etchant bath, and washing away the resist to leave only the patterned material behind. A variety of wet etch chemistries exist, covering most common materials [127, 128]. Typically, if a suitable wet etch chemistry exists, wet etching will be the most desirable processing method due to its simplicity. However, etchants are often harsh chemicals, and thus may not be compatible with other materials in a device. Also, liquid etchants will etch isotropically, meaning that they will seep under a mask if etch times are not carefully calibrated or device layers are especially thick.

Dry etching utilizes plasma-phase etchants to etch anisotropically along the direction of the electric field used to generate the plasma. This process, generally

known as reactive ion etching (RIE), can utilize a variety of gasses including highly fluorinated compounds such as tetrafluoromethane (CF_4) or trifluoromethane (CHF_3). Inert gasses are also usable, including argon, which is desirable for the energy it can deliver to a substrate due to its high atomic mass. To remain technically accurate, a dry etch process that uses only non-reactive ions is referred to as ion bombardment, since the material removal process is purely physical. Dry etching in general is applicable in situations where no suitable wet etch chemistry exists or resist undercut is a significant problem. The dry etch process proceeds in the same order as a wet etch, replacing the wet etch bath with exposure to plasma-phase etchants. Dry etch is often much less selective than wet etch, however, and can cause significant film damage from ion bombardment and ultraviolet irradiation. Further, dry etch will damage photoresist to the point that it is often difficult or impossible to remove without damaging device materials. Combined with the increased cost and complexity introduced by using a vacuum process, this limits the overall applicability of dry etching procedures.

The current work investigated the use of dry etching, but did not apply it in final device fabrication. Gold, silver, and titanium were conducive to wet etching. Gold etching utilized type TFA etchant, a potassium iodide (KI) based solution, available from Transene Company, Inc. Gold etch in this solution at room temperature was observed to proceed at approximately 100 nm/min. Silver etching occurred using a dilute “base piranha” solution composed of 1:1:25 mixture of 30wt.% hydrogen peroxide (H_2O_2), 30wt.% ammonium hydroxide (NH_4OH), and DI

water. This formula of base piranha etched silver at approximately 150-200 nm/min. Titanium etching used a concentrated base piranha, using 1:1 30wt.% H₂O₂ and 30wt.% NH₄OH. Titanium etch in this solution proceeded at approximately 33 nm/min.

No appropriate wet etch chemistry exists for 90/10 atomic percent Pt/Ir. Aqua regia is reported to etch elemental platinum at a very slow rate [129], but an aqua regia formulation of 1:3 nitric and hydrochloric acid heated to 90 °C was not observed to create sufficient etch activity when applied to Pt/Ir. Literature reports iridium as slightly soluble [130] or insoluble [129] in aqua regia, and thus it was assumed that iridium helped cause wet etching of Pt/Ir to be impractical for the current work. Argon ion bombardment initially showed promise as an etching method, but began to show signs of significant Pt/Ir redeposition and was thus also avoided for the current work. This was assumed to occur because argon is non-reactive and both Pt and Ir are stable, solid, and inert, meaning that etch products were not held in the gas phase and therefore were difficult to remove from the chamber. The failure of an exhaust scrubber prevented the safe evaluation of reactive process gasses such as trifluoromethane (CHF₃). The final device iteration presented in this writing only required a 10 nm Pt/Ir film, and thus liftoff processing with S1818 was used instead.

3.4 Surface treatments

Adhesion between a substrate and a deposited material is a significant concern, especially in the field of flexible electronics. Polyimide is no exception, as the same

chemical inertness that makes it valuable for a range of devices causes it to be prone to poor adhesion. A range of surface treatments exist to address this problem.

To ensure strong adhesion between two layers, it is first necessary to ensure that nothing on the surface of either layer will interfere. A basic, general-purpose procedure to clean silicon wafers is to expose the substrate successively to acetone, methanol, and DI water, intending to dissolve a range of possible contaminants and physically wash away small particles. Isopropyl alcohol (IPA) replaced methanol for this work due to the safety concerns in a university laboratory. Cleaning was performed using either sequential rinses or sonication in each of these solutions, as specified in experimental chapters.

Several chemical treatments have been reported to enhance adhesion of metals to polyimide. One treatment investigated in Chapter 4 involves the use of potassium hydroxide (KOH) and hydrochloric acid (HCl) to increase the concentration of polar active groups on the polyimide surface or even convert the surface of PMDA-ODA polyimide into potassium polyamate, which has shown improved adhesion between polyimide and metal films in literature [131, 132]. Other chemical treatments were avoided due primarily to safety and handling concerns.

The most common treatment for improving adhesion between metal and a polyimide film is to expose the polyimide to a plasma before depositing metal on it. This process, sometimes referred to as corona treatment, has been examined using a number of different process gasses including argon, oxygen, and mixtures of the two occasionally with added nitrogen [66, 68, 105, 133–135]. Exposure to any plasma

will modify the polyimide surface both chemically and mechanically. Chemical modification takes place by breaking chemical bonds at the polyimide surface, leaving dangling or unstable bonds behind and thereby forming energetically favorable adsorption sites for deposited species. Mechanical modification occurs by simply roughening the polyimide surface, which is beneficial because it both increases total surface area and thus total surface energy, and because it potentially creates a mechanical trapping effect by physically capturing an amount of deposited material at the interface.

Chapter 4 examines several different surface treatments to improve adhesion of deposited metal on polyimide and gold films in detail.

3.5 Characterization

This work applied a number of characterization methods to observe, troubleshoot, and measure the success of each part of this project.

3.5.1 Surface energy

A common method of measuring surface energy is to place a drop of water with a known volume on a surface to analyze and measure the contact angle between the surface and the liquid-air interface. Assuming that both the drop and the substrate are not accelerating with respect to one another and that the drop is symmetric about a central axis, interfacial tension and gravity should be the only forces determining the shape of the drop, thereby allowing direct comparison of the surface energy between different surfaces analyzed by this method [136]. A surface with high surface energy relative to the liquid-ambient interface will generate a very low contact angle,

meaning that the water drop will spread out to increase the area of the water-surface interface. A low surface energy will instead create a drop that is closer to spherical as the drop attempts to minimize surface area in contact with the surface. More complex methods of determining surface energy exist, such as X-ray Photoelectron Spectroscopy (XPS) [137], but a simple comparison of “higher” vs. “lower” surface energy was sufficient for this project. Example contact angle measurements are presented in Chapter 4.

3.5.2 Interfacial adhesion

The goal of increasing surface energy of a material is, for the purposes of the current work, to increase adhesion to a layer deposited on that surface. A direct but imprecise method of measuring adhesion is given by the tape test measurement detailed in American Society for Testing and Materials (ASTM) standard D3359-09^{E2} [138]. A blanket coat of material is deposited on a substrate and scored into a 5x5 grid of squares, approximately 2 mm² each. Scotch® tape (a 3M brand) is then applied, firmly rubbed onto the coating surface, and peeled away. The substrate is then examined and classified by the approximate percentage of coating that remains. The current work modified this technique by using structures defined via photolithography instead of a simple grid of squares, and thus did not use the classification system prescribed by the given ASTM standard.

A more quantitative adhesion measurement technique is given in ASTM standard D451-09^{E1} [139] and used by at least one group in literature [134]. This standard describes a “pull-off test” that can be performed using a loading structure, an

adhesive, and a tension gauge. The loading structure, some sort of dolly or stud, is glued to the coating under examination and allowed to set. The loading structure is then fitted into a testing apparatus with a tension gauge, which applies tension normal to the substrate surface, increasing strain at a controlled rate, until adhesive failure occurs. The tension required to induce failure is then recorded. Assuming failure occurs within the system under test, not where the loading structure is affixed to the system, this value gives a direct and quantitative measurement of adhesive strength. This technique was not applied in the current work, but is described here for its potential in future work.

Other mechanical methods exist to test adhesion strength, such as blister, stretch deformation, scratch, and peel tests, as described in literature [66]. Blister tests, or “bulge” tests, require a more complicated setup than was deemed practical for the current work. While simpler to perform, stretch deformation, scratch, and peel tests were avoided in the current work because the results of both are highly dependent on film properties other than pure adhesion. One example of this is that copper films on PMDA-ODA polyimide have shown adhesion values of 0.052 J/m^2 in blister tests, 9.6 J/m^2 in stretch deformation test, and 600 J/m^2 in peel tests [66].

3.5.3 Mechanical durability

The goal of improving interfacial adhesion within devices produced by the current work was ultimately to improve mechanical durability by the mechanisms explained in Chapter 2.4. The produced devices are intended to withstand being rolled into a cylinder with inner radius approximately 0.25 mm, and so devices were evaluated by

bending them by hand around a 26g needle with an outer radius of 0.23 mm, slightly smaller and thus more strenuous than the target bend radius. In some cases an 18g needle, outer radius 0.635 mm, was used for samples that failed immediately around a 26g needle. In either case, samples were then lightly pinched by hand to ensure conformality to the nominal bend radius. Optical microscopy images and, in some cases, electrical resistance measurements were taken before and after bending to observe and quantify the effects of these tests. In cases where samples survived one bend, the process was repeated and images and electrical measurements were taken periodically throughout the process.

Manipulating thin films by hand is not especially reliable, especially for high numbers of bending cycles, and so Tyler Milhem at Pacific Diabetes Technologies fabricated a device for repeatedly bending a sheet of devices in a controllable manner. This device is pictured in Figure 3.4.

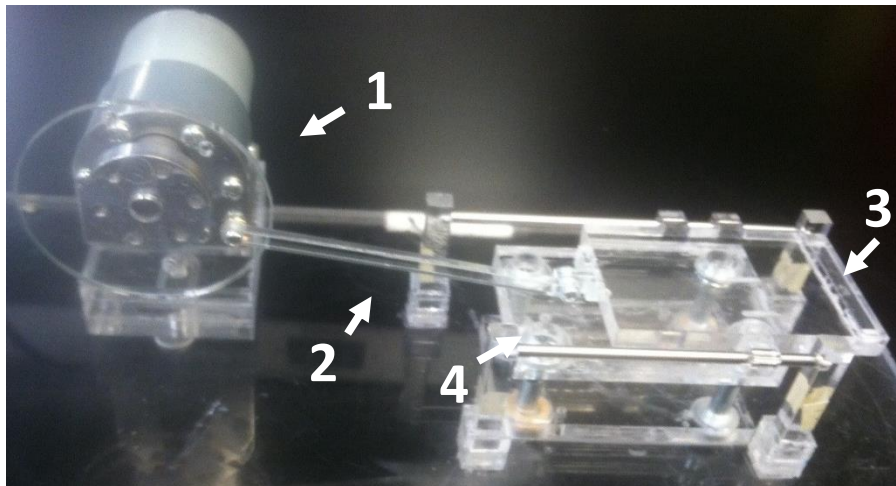


Figure 3.4: Automated flex tester, fabricated by Tyler Milhem at Pacific Diabetes Technologies. Image credit to Pacific Diabetes Technologies. Annotations added and described in the text.

In this device, a variable-speed motor (labeled 1 in Figure 3.4) drives a plate with holes drilled at different distances from its center. A shaft (2), hinged on each end, connects one of these holes to a movable plate (3) that slides horizontally on greased rails. The distance that this plate travels per revolution of the drive plate is determined by choice of hole in the drive plate. Samples are taped between the movable plate and a fixed base plate (4) in a bent position, so that the motion of the movable plate will move the created crease through the entire sample twice with each revolution of the drive plate. The fixed plate can be raised or lowered by adjusting the bolts that support it at each corner, thereby adjusting the bend radius to which samples are subjected. Unless otherwise noted, samples bent by automated testing in this work were tested with a 2 mm plate gap (giving a 1 mm bend radius) at 150 plate revolutions (300 bends) per minute, with deposited layers facing inward in order to induce compressive stress. Compressive stress is expected to cause adhesive failure, as explained in Chapter 2.4.2, and thereby served to test adhesion. As with manual bending, optical images and electrical resistance measurements were taken before and after device bending as well as periodically throughout the process.

3.5.4 Imaging and elemental analysis

Three types of microscopy were employed to characterize devices. Optical microscopy was used to inspect the quality of each step in device production and to provide a qualitative idea of device integrity, as well as to characterize the results of tests as described above. Use of a AmScope dissection scope allowed lighting of samples either from above, as traditionally performed, or from behind. Backlit images

are presented in the current work to highlight the formation of cracks in opaque layers; Figure 3.5 demonstrates the utility of backlit images to highlight flaws.

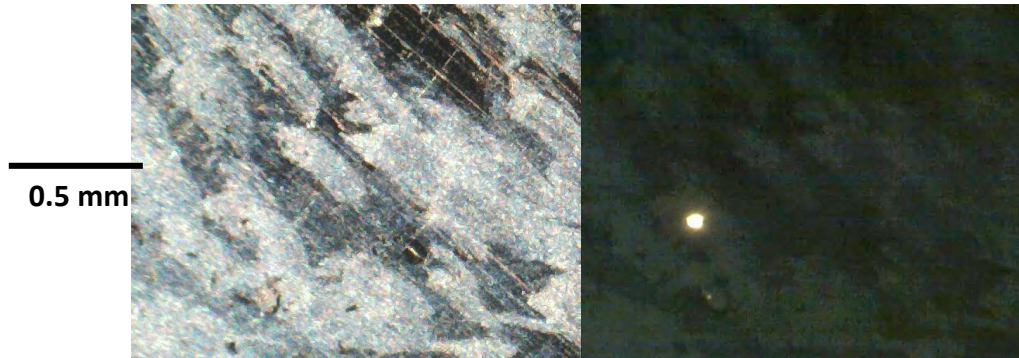


Figure 3.5: Top-lit (left) and backlit (right) images of the same area, highlighting the utility of backlit imaging to find defects in opaque materials.

Scanning electron microscopy (SEM) was used to examine samples at high magnification, allowing visualization of defects, failure modes, etched sidewalls, and cross-sections of device layers. SEM is performed by rastering an electron beam across a sample surface, collecting a resulting signal, and combining this signal with the known location of the beam in order to create an image. The signal most often used to create an image in SEM is generated by electrons emitted by atoms excited by the electron beam. These secondary electrons are collected and focused by an electromagnetic lens and directed to a detector. Generally the sample is located outside this lens, but small nonmagnetic samples, such as those used in the current work, can be placed within the lens in order to collect as many secondary electrons as possible. SEM in the current work was performed first using a FEI Quanta 600F environmental SEM system, then switching to a FEI Nova NanoSEM 230 high

resolution SEM to utilize immersion mode functionality. Both tools were used at the Oregon State Electron Microscopy and Imaging Facility.

Limited elemental analysis was performed using energy dispersive X-ray spectroscopy (EDAX), utilizing the electron beam produced by SEM. Along with secondary electrons, characteristic X-rays are also emitted by electrons within atoms excited by the electron beam. Collecting these X-rays and comparing their energies to known electron transitions within atomic systems allows identification of the elemental composition of a material. This technique was instrumental in identifying the interfaces where adhesion problems occurred, as explained in Chapter 4.

Transmission electron microscopy (TEM), a similar method to SEM, was applied to image the work presented in Chapter 7. Very thin slices of material can be placed between an electron beam and a detector, which generates a signal by collecting electrons transmitted through the material under observation instead of relying on secondary electrons. TEM is regularly used to collect images with resolution below 1 nm. TEM in the current work was performed by Sean Smith using a FEI Titan 80-200 TEM/STEM system at the Oregon State Microscopy and Imaging Facility.

3.5.5 Electrochemical response

The goal of these devices is to create an electrical signal proportional to only the concentration of glucose at the sensor location. This electrochemical response was measured by Chris Durgan and Dr. Xiaosong Du with OSU Chemical Engineering as well as representatives of Pacific Diabetes Technologies. A potentiostat system was used to apply a 0.6 V between sensing electrodes (+) and either an external silver-

silver chloride electrode (SSC) or the SSC included in the developed devices (-). Devices were then submerged in a phosphate buffered saline (PBS), chemicals of interest were added in a controlled manner, and the resulting oxidation current measured as a function of concentration. PBS was used in order to simulate the subcutaneous environment. Hydrogen peroxide (H_2O_2) was added for tests intending to directly examine oxidation at the electrode surface, glucose was added for experiments to directly test glucose-detection capability, and acetaminophen was added in tests examining the potential for interference.

4. Development of a Flexible Device Foundation

This chapter details the selection of a proper foundation for the fabrication of a flexible glucose sensor. Section 1 gives the general fabrication process used in this chapter. Section 2 discusses selection of a rigidization method to evaluate devices properly. Section 3 describes experiments using the materials originally envisioned for this project: PMDA-ODA polyimide film (PI), encapsulated by aluminum oxide (Al_2O_3), supporting a titanium (Ti) adhesion and conduction layer and capped off by a thin platinum/irridium 90/10 at.% (Pt/Ir) layer for catalysis. It was determined that Al_2O_3 was likely not appropriate for the bend radius required for our devices, however, and Section 4 explores elimination of the Al_2O_3 layer altogether, instead depositing Ti directly on PI. The PI-Ti interface still proved problematic, and Section 5 presents experiments using commercial gold-coated polymer substrates to circumvent this problem, eventually settling on gold-coated PI for device construction.

4.1 Device preparation

Samples in this chapter were all fabricated in a similar manner. Deviations to this process are listed in the relevant section. Preparations beginning with uncoated polymer substrates were sonicated successively in acetone and isopropyl alcohol (IPA) for 5 minutes each before being submerged in a bath of DI water. Samples were allowed to dry on a clean silicon wafer on a hotplate in open air at 65 °C before being baked in a Neytech Qex vacuum furnace at 200 °C and approximately 200 torr for 24 hours. Cleaned and baked polymer films were taped to glass slides and optionally

subjected to a plasma surface treatment (Plasma 1), and then loaded into a Gemstar Arradiance ALD system for Al_2O_3 deposition. Samples were mounted in the ALD chamber affixed with single-sided Kapton tape at each end so that samples bridged away from the substrate slightly, exposing both faces to Al_2O_3 deposition. ALD depositions occurred at 175 °C chamber temperature using trimethylaluminum (TMA) and water, pulsing TMA first and using 20 ms pulses and 10 s purges for both TMA and water, using 455 cycles to achieve approximately 50 nm of Al_2O_3 deposition on silicon witness coupons, as verified by a simple single-wavelength ellipsometer. The detailed ALD recipe is presented in Appendix 3. Samples were then re-affixed to glass slides and received a second plasma step (Plasma 2) in some preparations, followed by deposition, exposure, and development of S1818 photoresist to create patterning for metal liftoff according to the recipe in Chapter 5. One preparation was then exposed to a third post-patterning plasma treatment (Plasma 3).

Samples were transported from the MASC lab to MBI for sputtering. Ti and Pt/Ir were deposited successively, without breaking vacuum. Metal thicknesses were varied by adjusting deposition time. Finally, samples were returned to the MASC lab and sonicated in acetone long enough to lift off unwanted material. Sonication time for liftoff varied depending on thickness of the deposited metal layer, taking a maximum of ~1.3 hours for 50 nm Pt/Ir on 700 nm Ti down to a minimum of ~20 minutes for only 10 nm Pt/Ir.

4.2 Rigidization

Samples addressed in this section investigated a variety of rigidization methods to rigidize 25 or 50 μm Kapton-HN PMDA-ODA polyimide film, produced by E. I. du Pont de Nemours and Company, referred to herein as DuPont. Device stacks included Kapton, 50 nm Al_2O_3 , 100 nm Ti, and 50 nm Pt/Ir, with no surface treatments besides sonication in acetone and IPA. This device stack is shown in Figure 4.1.

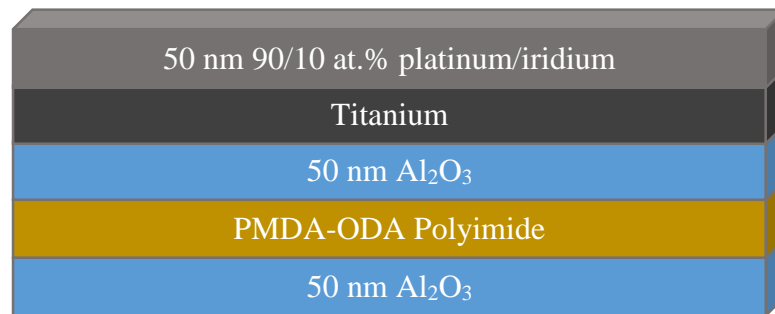


Figure 4.1: Device stack for Sections 1-3.

4.2.1 Initial rigidization methods

Several rigidizing methods were investigated before arriving at Gel-Pak DGL film as a workable solution. First attempts simply used single-sided Kapton adhesive tape to secure the edges of a PI film, the first substrate material examined, to a glass slide. This was sufficient for early experiments, but tape acted as a spacer between the substrate and a photomask and thus was determined to be inappropriate for multi-layer processes, especially when attempting to optimize sidewall profile for liftoff processing. Photoresist from photolithography processes also was able to seep

beneath taped samples, creating discoloration, contamination concerns, and the potential for offgassing in vacuum.

Samples were then adhered to glass slides using S1818 photoresist as an adhesive after moderate baking to drive out solvents, but all recipes tested failed to produce a film with both sufficient adhesive quality and a lack of offgassing, as evidenced by the formation of bubbles beneath the polyimide surface. Surprisingly, simply placing a wet sample of PI on a glass slide before baking steps worked very well to adhere PI to glass and maintain planarity even through most processing steps, though occasional wrinkling would occur during baking. The three aforementioned rigidization methods failed quickly upon sonication in acetone, however. Though samples could be reattached, devices demonstrated significant crack formation during this process.

To confirm that the observed cohesive failure was due to samples floating free during liftoff sonication, devices were fabricated on polyimide using water and photoresist affixing methods and compared to samples deposited directly on glass. Figure 4.2 shows the occurrence of different flaws, categorized by qualitative description, across samples prepared by each method.

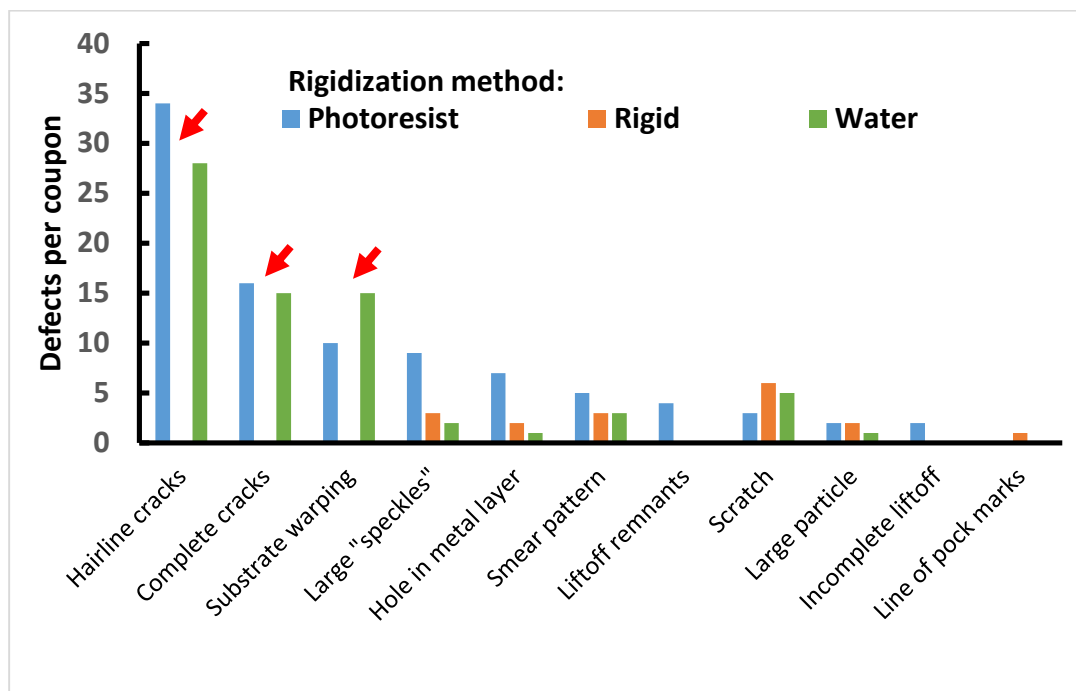


Figure 4.2: Occurrences of flaws in samples produced using different rigidization methods, sorted by qualitative appearance under optical microscopy. “Photoresist” refers to S1818 photoresist used as an adhesive, “rigid” refers to fabrication directly on glass, and “water” refers to the water affixing method discussed above. The lack of cracks in rigid devices, indicated by red arrows, motivated the use of a better rigidizing method.

The clear lack of cohesive failure in rigid devices was taken as evidence that a rigidizing solution able to withstand sonication in acetone was necessary, thus motivating examination of Gel-Pak DGL adhesive films.

4.2.2 Gel-Pak DGL film

Gel-Pak DGL film, introduced in Chapter 3, is available in several adhesive strengths. A film that is too weak will not maintain adhesion through sonication in acetone, while a film that is too strong will induce stress when attempting to remove a substrate. Initial devices used liftoff processing of thick (600 nm or greater) metal

layers and therefore required sonication times often exceeding one hour, requiring these devices to use the strongest film available (labeled X8). This adhesive strength made device removal problematic, however, as microscope observations and electrical measurements of early samples occasionally demonstrated crack formation and electrical failure resulting from the peeling process if the handler was not careful.

Two experiments were performed to select the appropriate gel adhesive strength for device production. First, 12.7 μm thick Linqtape PMDA-ODA polyimide film, manufactured by CAPLINQ Corporation, was applied to glass slides using gel films of three different adhesive strengths, labeled X0, X4, and X8 from weakest to strongest. Approximately 200 nm of silver were then evaporated onto each sample before patterning them into 77 individual leads of 7 different lengths (and 50 μm width per coupon). The electrical resistance of each trace was measured before and after peeling each sample from its gel. In the case of X8 gel, a unique removal method was evaluated alongside simple peeling, in which a piece of paper was maneuvered beneath the substrate as a kind of “saw” to separate the sample from the gel with a minimum of bending or tensile stress. Gel adhesion through acetone sonication was also evaluated by affixing blank Linqtape samples to glass slides using samples of X0, X4, and X8 gel. These samples were then immersed in acetone and sonicated until first adhesive failure was observed.

No damage or measurable resistance change was observed removing evaporated silver samples from any strength of gel, and so the experiment was later repeated with 150 nm thermally evaporated gold on 12.7 μm Kapton, using material described in

Section 4, in an attempt to recreate the failures observed in previous samples. Even in the case of gold, however, no significant resistance change or visible cracking was observed despite reports from PDT. The amount of sonication time observed before adhesive failure differed between gel strengths, however. Table 4.1 summarizes these results by providing both the average resistance change and sonication time to adhesive failure for each system examined.

Table 4.1: Evaluation of Gel-Pak adhesive strengths

Gel strength	Avg. resistance change after coupon removal	Sonication time to adhesive failure (m)
X0	Not discernable from noise, regardless of removal method	5-15
X4		25-30
X8		>60

Gold samples only required liftoff processing of 10 nm Pt/Ir , which meant that gel films were only required to withstand ~20 minutes of sonication in acetone, thus suggesting that there was nothing to lose by stepping down from X8 to X4 strength gel despite of the lack of observed damage with X8. Previously observed damage was attributed to either fragile device construction, especially in the case of samples using Al₂O₃ adhesion layers, or simply rougher handling. Non-uniform adhesive quality between gold and polyimide across the Sheldahl-coated film may also explain the appearance of earlier damage.

4.3 Al₂O₃ interlayers

Having solved most mid-process failures using an improved rigidization solution, focus shifted to bending performance of processed devices. The George group at the University of Colorado has extensively analyzed ALD Al₂O₃ on polyimide surfaces, and has shown that even Al₂O₃ layers as thin as 5 nm will crack under bending radiuses of 2.59 mm, far less extreme than the 0.25 mm radius required for the current application [140]. This raised the question of whether ALD Al₂O₃ would provide a suitable foundation for our devices.

4.3.1 Thicker Ti to compensate for Al₂O₃ failure

The first attempt at device construction with the Gel-Pak rigidization solution used 25 um Kapton-HN, which received 100 nm Ti and 50 nm Pt/Ir. These devices survived processing much more effectively than devices prepared with other rigidization methods, but still demonstrated significant cohesive failure upon bending around a 18g needle (radius 0.635 mm) by hand, as demonstrated in Figure 4.3. The device stack was as represented in Figure 4.1.

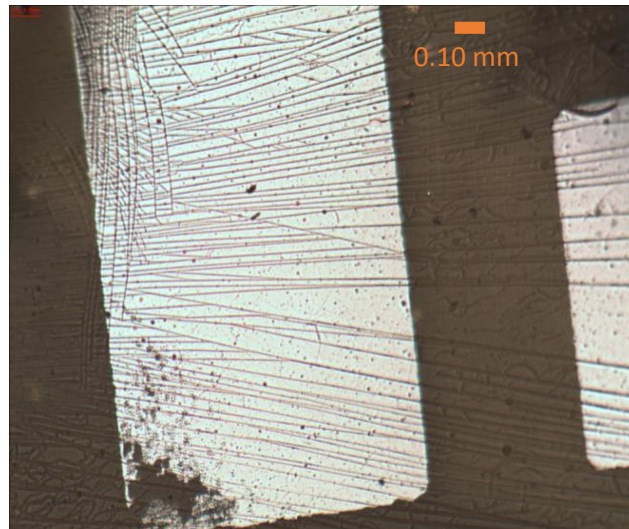


Figure 4.3: Top-lit optical microscopy image showing widespread cohesive failure present in initial samples.

Figure 4.3 demonstrates cracking that extends between isolated metal features, implying cracking of the underlying Al_2O_3 layer. The polyimide itself was observed to tolerate folding completely in half without demonstrating cohesive failure.

The first solution explored for this problem was to apply thicker layers of Ti, hoping that increased cohesive strength of the metal layers would improve the cohesive strength of the overall stack and outweigh the negative effects of increased device thickness as presented in Chapter 2. 50 nm of Al_2O_3 and 20, 50, 160, and 270 nm of Ti were deposited, using 12.7 μm CAPLINQ Linqtape PMDA-ODA polyimide film and no Pt/Ir for the 20 nm Ti sample and 12.7 μm Norton-S PMDA-ODA polyimide film and 50 nm Pt/Ir for 60, 170, and 280 nm Ti. New providers for polyimide films were utilized due to DuPont's stipulation that devices must not be used for human implantation without their consent. Device stack was still as represented in Figure 4.1.

These samples with varying metal thicknesses were patterned into 8 mm traces of 1.00, 0.50, 0.30, and 0.03 mm width and repeatedly bent by hand around an 18g needle, radius 0.635 mm, which was meant to be less extreme than the 0.25 mm radius targeted for the application. Simple 2-point electrical resistance measurements were taken with a Fluke 83 multimeter before bending and after certain numbers of bends. The resulting data is shown in Figure 4.4.

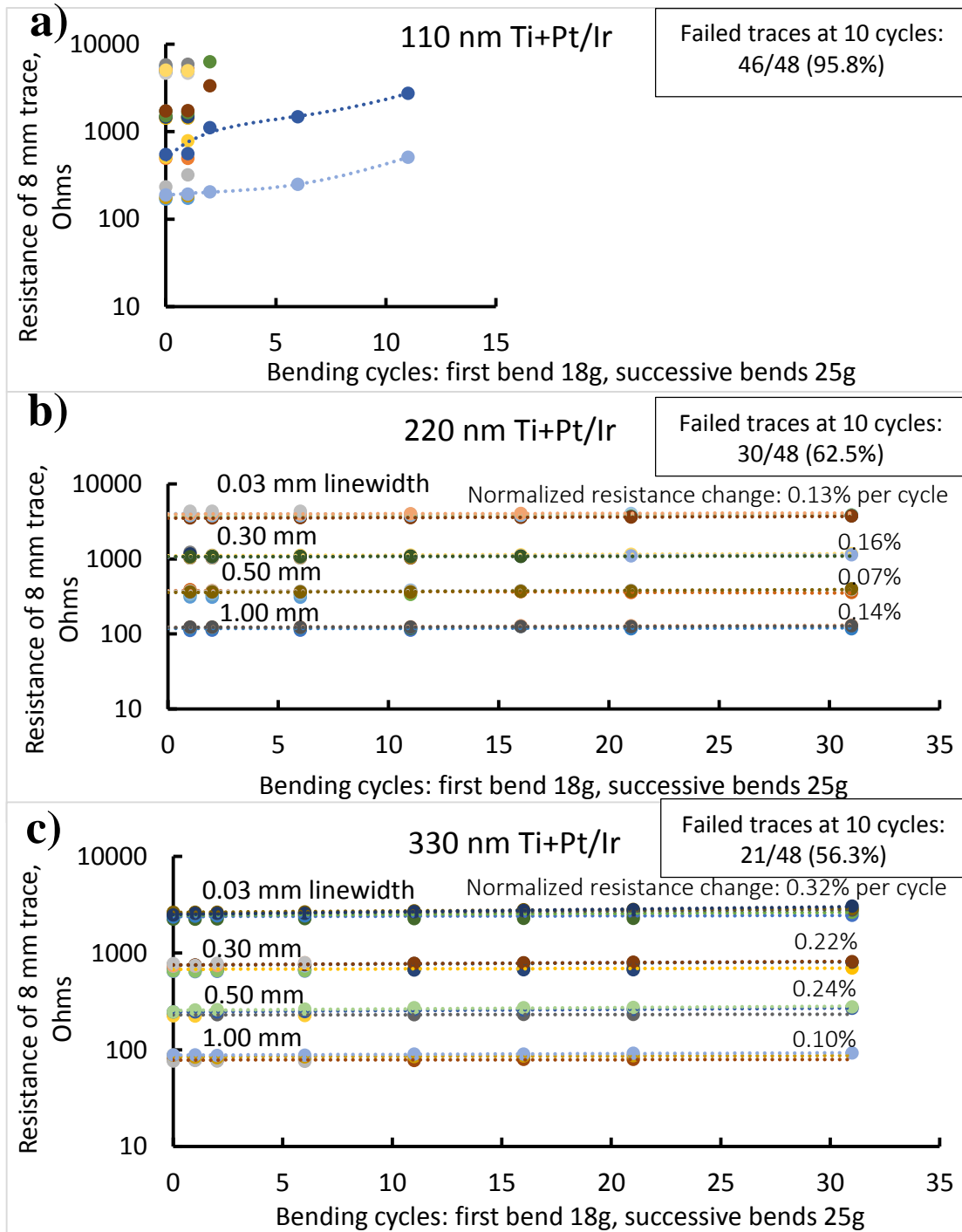


Figure 4.4: Bending of varied metal thickness / 50 nm Al₂O₃ / 12.7 μm Norton PI, using an 18g needle. Line widths of 0.03, 0.30, 0.50, and 1.00 mm were tested for each thickness. Resistance change for traces that did not fail is approximated as linear and reported as percentage change per bend, normalized to unbent resistance values. Insets show number of completely failed traces after 10 cycles. Not shown: 20 nm Ti on 50 nm Al₂O₃ on Linqtape, in which case all leads failed by 10 bends.

Figure 4.4 demonstrates that thicker metal stacks did generally tolerate more bends before complete electrical failure, but at the cost of a higher resistance change per bend. This observation suggests that devices with metal layers on brittle, failure-prone underlayers may benefit from increasing metal thickness in order to extend device lifetime, though more work needs to be done to establish this as a general concept. This approach would also only be useful for devices that are relatively insensitive to changes in trace resistance. If true in the general case, however, this observation suggests a subtle exception to the common wisdom that thinner layers are optimal for flexible devices, as explained in Chapter 2. Use of Al_2O_3 was abandoned for the current project (a decision more thoroughly justified in Section 4) and was no longer immediately relevant, however, and this trend was not explored in more depth.

4.3.2 Surface treatments for interfacial adhesion

Devices fabricated by any preparation discussed so far failed to maintain electrical conductivity after bending around a 26g needle, radius 0.23 mm, which was more representative of the target bend radius of 0.25 mm than an 18g needle (radius 0.635 mm) used previously. An array of samples were created to investigate the effects of surface treatments between processing steps, as research has shown that improved adhesive properties between layers can help distribute stress and delay cohesive failure [66, 68]. These samples used 12.7 μm Norton-S film and followed construction as described in Section 1 and Figure 4.1, using processing parameters as shown in Table 4.2.

Al ₂ O ₃ thickness (nm)	Ti thickness (NM)	Pt thickness (nm)	Pre-ALD plasma gas	Pre-ALD plasma time (m)	Pre-ALD plasma power (W)	Post-ALD plasma time (m)	Post-ALD plasma power (W)	Post-pattern plasma gas	Post-pattern plasma time (m)	Post-pattern plasma power (W)
50	600	50	-	-	-	-	-	-	-	-
50	600	50	Ar	1	300	-	-	-	-	-
50	600	50	Ar	5	300	-	-	-	-	-
50	600	50	Ar	1	300	1	300	-	-	-
50	600	50	Ar	1	300	5	300	-	-	-
50	600	50	Ar	1	300	1	300	O ₂	1	50
50	600	50	O ₂	0.5	50	-	-	-	-	-
50	600	50	O ₂	0.5	50	-	-	-	-	-
50	600	50	O ₂	0.5	50	-	-	-	-	-
50	600	50	O ₂	0.5	50	-	-	-	-	-

Table 4.2: Sample preparations exploring surface treatments to improve mechanical stability in devices using Al₂O₃ interlayers.

For all preparations represented in Table 4.2, widespread cohesive failure was still observed after bending once around a 26g needle. SEM imaging explored failed sites in more detail, and revealed extensive adhesive failure around sites that displayed cohesive failure. Bending tests did not clearly differentiate between any of the samples prepared, as it was impossible to ensure that each sample was bent exactly the same. Figure 4.5 displays representative results of bend tested samples.

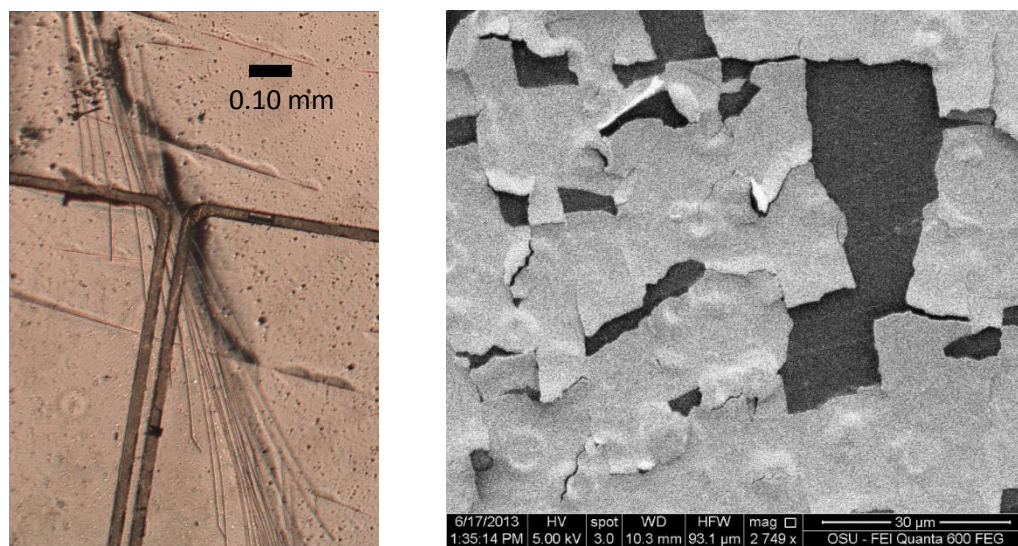


Figure 4.5: Representative images of failed 50 nm Pt/Ir on 600 nm Ti on 50 nm Al_2O_3 with no intermediate surface treatments.

Left: Top-lit optical microscope image showing shattering/cracking extending between isolated metal features.

Right: SEM image. Delamination and shattering occurs near cohesive failure locations.

4.3.3 Investigation of adhesive failure

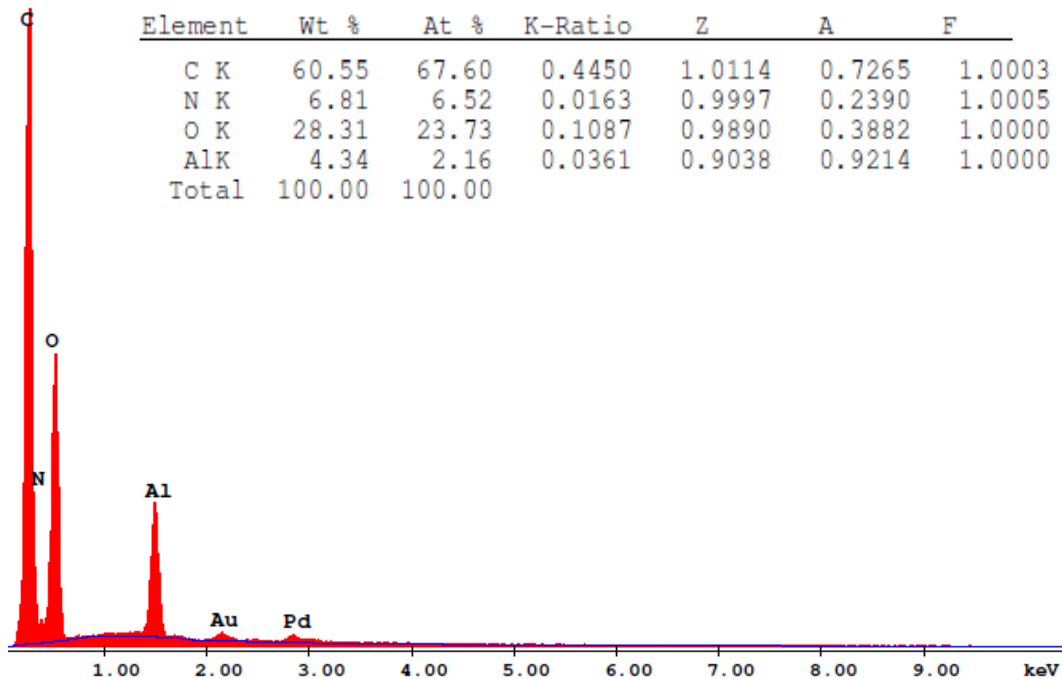
It was expected that adhesive failure would likely occur at the PI- Al_2O_3 interface, as similar problems have been reported due to CTE mismatch [141]. Further, Al_2O_3 deposited on polymeric substrates has been reported to provide good adhesion to Ti in other circumstances [134]. It was hoped that experimental confirmation of the

interface at which adhesive failure occurred would give some insight into the cause of device failure. EDAX was performed on both the backside of metals removed via tape test and the surface that those metals left behind. Figure 4.6 displays the resulting EDAX spectra for a sample initially composed of 50 nm Pt/Ir / 600 nm Ti / 50 nm Al₂O₃ / 12.7 μm Norton film that received no plasma treatment. These spectra clearly indicate the presence of Al on the PI surface and not on the back of removed metal, demonstrating that the Al₂O₃ remains behind and thus the Al₂O₃-Ti interface was weaker than the Al₂O₃-PI interface. The strong C, O, and N signatures on the surface from which metal was removed are signals from the PI itself, as X-rays collected by EDAX were generated from a penetration depth greater than the 50 nm Al₂O₃ layer that was present. The same elements on the spectra from the removed metal itself are likely from either the tape used to remove it or contamination during sample preparation. Gold and palladium signatures on both samples are due to a thin coat of sputtered Au/Pd for SEM imaging.

The signal appearing to indicate vanadium (K_{α1,2} at 4.95 keV [142]) in the delaminated metal is from an unknown source. The closest probable emissions are L-lines of cerium and praseodymium (which are even more unexpected), and no vanadium processes were recorded on any tool log associated with the fabrication process. The Ti target, obtained from Kurt J. Lesker company, was guaranteed to have extremely low vanadium content. Vanadium does not represent the sample holder, as a layer of conductive copper tape was used to affix samples to the sample holder and thus a copper signature would have been visible before a signal from the

sample chuck. Contamination in the SEM chamber or other locations should also have shown up on both spectra.

a) Substrate surface beneath delaminated metal



b) Backside of delaminated metal

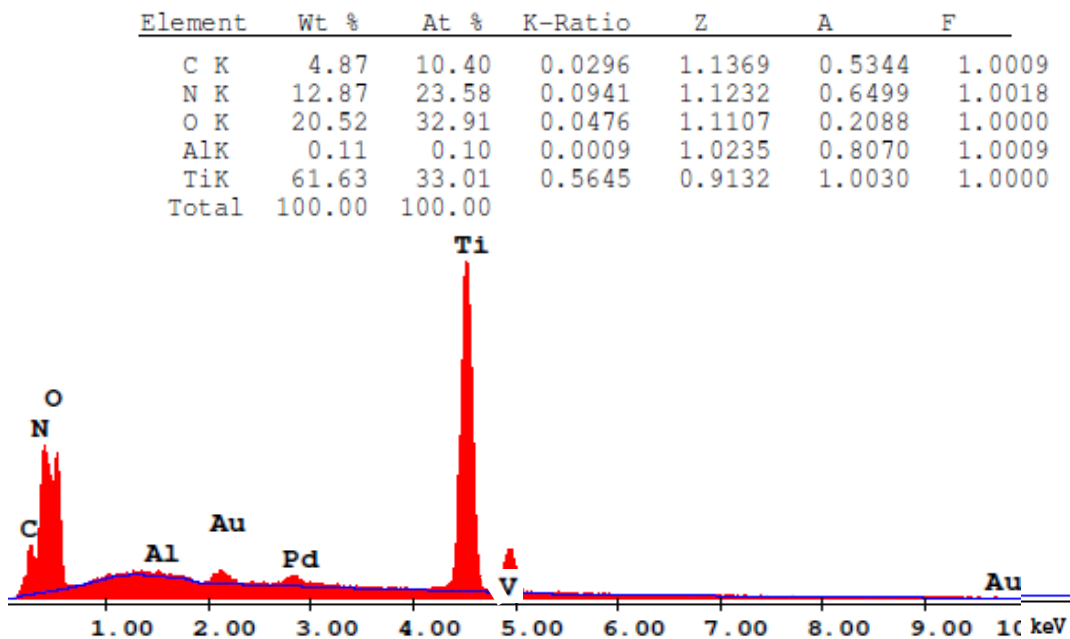


Figure 4.6: EDAX spectra of a) the substrate surface exposed by delaminated metal and b) the backside of the delaminated metal itself. Initial device stack was 50 nm Pt/Ir on 600 nm Ti on 50 nm Al₂O₃ on 12.7 μm Norton. Delaminated metal was removed using Scotch tape. The presence of aluminum on the substrate surface indicates failure at the Al₂O₃-Ti interface.

It is possible that the observed failure at the Al₂O₃-Ti is not an intrinsic property of the material system, but was simply due to a fabrication process gone awry. This is suggested somewhat by the apparent presence of Vanadium, though a specific cause has not been identified. Before further exploration into the Al₂O₃-Ti interface, however, observations presented in the next section suggested getting rid of Al₂O₃ altogether.

4.3.4 Effect of Al₂O₃ thickness

In order to examine whether Al₂O₃ was necessary in the first place, samples were fabricated without Al₂O₃ as well as with 5 or 50 nm of Al₂O₃ on Norton film treated with a 5 m, 300W Ar plasma before ALD (or metallization, in the case of no Al₂O₃). Devices were then bent around a 26g needle, radius 0.23 mm (compared to the target 0.25 mm), and un-bent portions were scratched 20 times with a hand-held razor while applying light pressure. The results are shown in Figure 4.7.

Figure 4.7 presents a clear trend of improved mechanical properties with reduced Al₂O₃ thickness. Widespread cracking can be seen in the bent 50 nm Al₂O₃ sample, as had been visible for all other samples with 50 nm Al₂O₃. Several, but far fewer, cracks are visible for 5 nm Al₂O₃. Only a crease, with no visible cracking at all, is visible for samples with no Al₂O₃. Scratch tests showed a similar trend, demonstrating that more metal seemed to delaminate with increased Al₂O₃ thickness. This result, combined with the observations presented so far, motivated avoiding Al₂O₃ completely for device fabrication. More research may be useful on this topic, however, as addressed in Chapter 6.

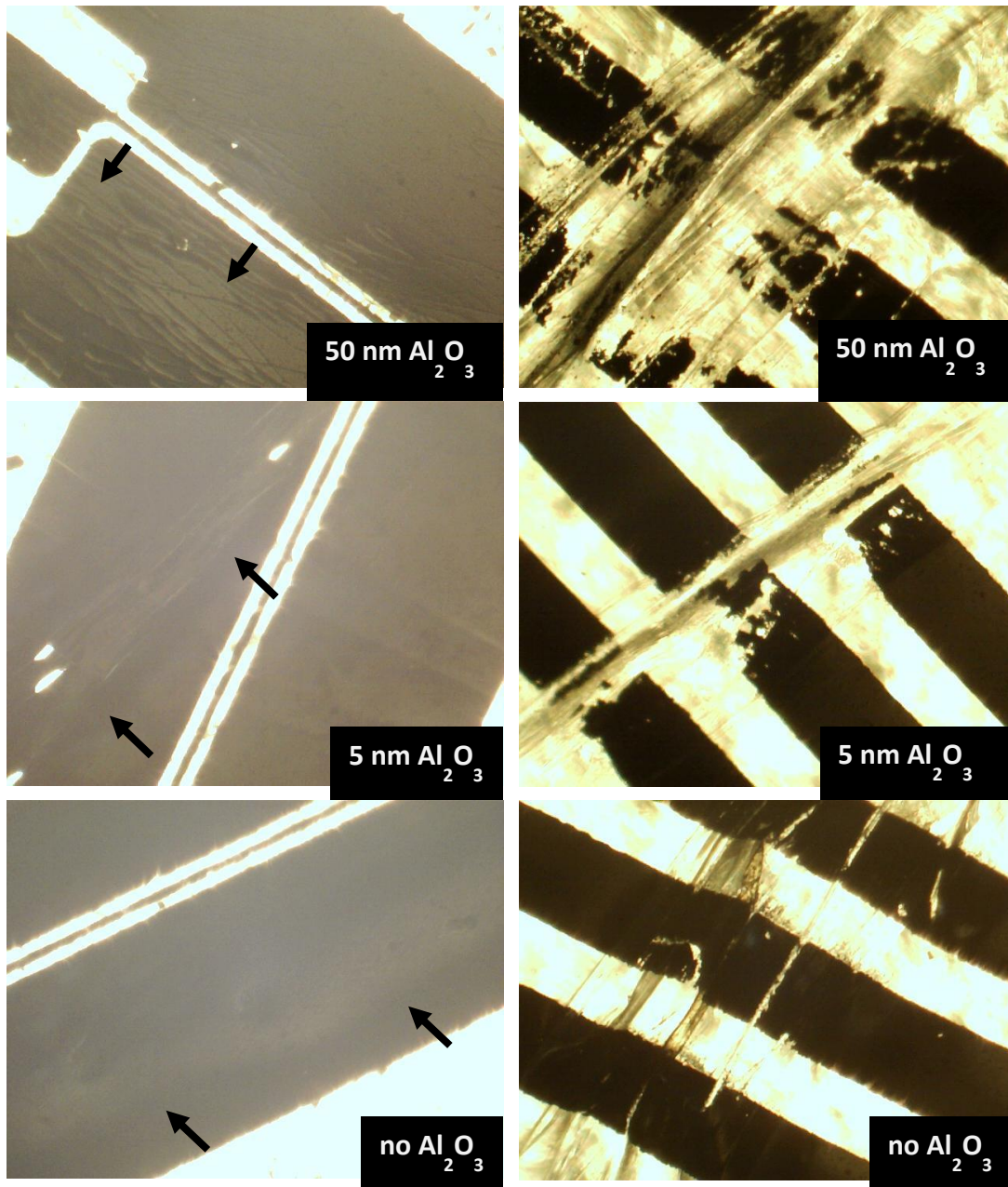


Figure 4.7: Backlit optical images of manual bend (left) and scratch (right) test results for devices prepared with 50 nm Pt/Ir on 600 nm Ti on x Al₂O₃ on 12.7 μ m Norton-S. Bending was performed once around a 26g needle. Performance in both tests was observed to improve with decreasing Al₂O₃ thickness. All samples used a 5m, 300W Ar plasma in before ALD or metal deposition, chosen as described in the Section 4.4.

4.4 Titanium deposition on polyimide

After the results presented in Figure 4.7 demonstrated that avoiding the use of an Al_2O_3 layer altogether appeared to improve mechanical integrity, focus shifted to optimization of direct deposition of Ti on PI, resulting in the simple device stack shown in Figure 4.8.



Figure 4.8: Device stack for Section 4.

Before arriving at the plasma treatment used for in Figure 4.7, other surface treatments were investigated to find which most improved surface energy of PI. Linqtape samples were cleaned as in Section 4.1 and applied to glass slides using Kapton adhesive tape, plasma treatments were performed, and surface energy was then evaluated using contact angle measurements as described in Chapter 3.5. One non-plasma surface treatment was also tested by submerging non-rigidized Linqtape samples into 10 wt.% KOH for 30 or 60 minutes, intending to create a potassium polyamate surface [132]. These samples were then washed with water to remove excess KOH and transferred to 10 wt.% HCl to create a surface of polyamic acid, which has shown improved adhesive properties through leveraging Lewis acid-base interactions [132]. Other chemical treatments reported in literature including exposure to sulfurous or acidic vapors [66], but safety and equipment concerns made most

chemical treatments more complicated than was considered practical for the current work.

Oxygen plasma treatments below 100 W were performed in a Plasma Etch Inc. model PE-50 plasma asher. Oxygen flow rate was 10 sccm and base pressure was 150 mTorr. The specific tool used is also commonly applied to ash photoresist and other organic contaminants, and thus contamination was a concern, though such was never demonstrated. This tool was used to apply 0.5, 1, 5, and 10 minute plasma durations at plasma powers of 25, 50, or 75 W. Not every combination of these parameters was examined, as trends indicated by intermediate results informed further experiments.

Argon and oxygen plasma treatments above 100W were performed in a Plasma-Therm I.P. System VII Batchtop reactive ion etch system. Base pressure reached approximately 3 mTorr and flow rates were 25 sccm for oxygen and argon. Chamber pressure during plasma treatment was 20 mTorr for argon and 100 mTorr for oxygen. 1, 2, and 5 minute treatments were performed at either 150 or 300 W. No other work occurred on this tool during the duration of the current work, though the tool was used previously for reactive dry etching of nickel and ion bombardment removal of Pt/Ir. Again, intermediate results informed further experiments, and thus not every combination of these process parameters was investigated.

Figure 4.9 shows contact angle measurements for untreated Linqtape and Linqtape treated with 5m, 300W Ar plasma. Preparations tested and resulting contact angles are given in Table 4.2 and Figure 4.10. Lower contact angles indicate higher surface energies, which should lead to better adhesion.

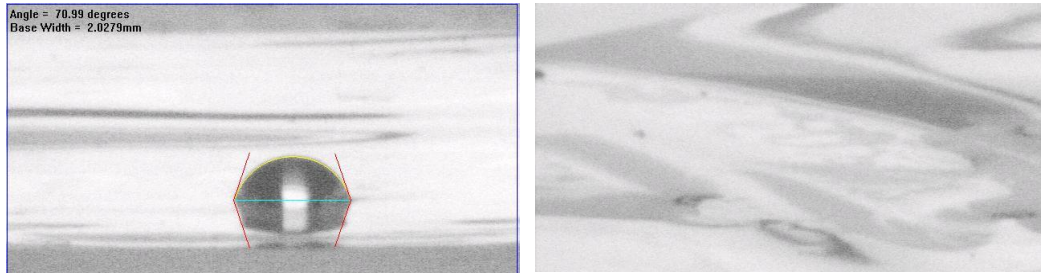


Figure 4.9: Contact angle measurements for (left) rinsed polyimide and (right) polyimide treated with 5 m, 300 W argon plasma. The plasma-treated surface was hydrophilic enough that that contact angle measurement was not possible.

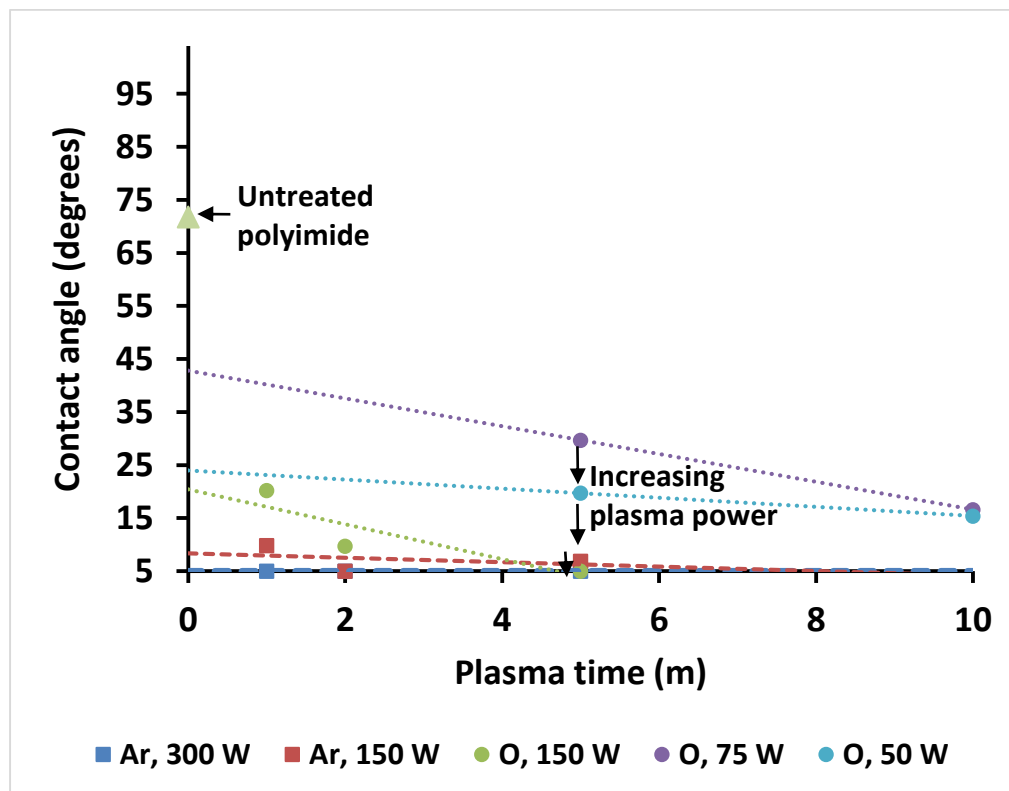


Figure 4.10: Plasma treatment of polyimide. Contact angle decreases with increasing plasma power and duration, and is lower for argon plasmas than oxygen plasmas.

Table 4.2: Results of contact angle measurements on polyimide surfaces, averaged across three drops per preparation. Continued on the next page.

*: 300W oxygen plasmas produced visible discoloration and were not examined for surface energy.

Treatment	Time (m)	Power (W)	Contact angle (°)
Ar	5	300	< 5
Ar	2	300	< 5
Ar	1	300	< 5
Ar	5	150	6.9
Ar	2	150	< 5
Ar	1	150	9.8
O ₂	5	300	*
O ₂	2	300	*
O ₂	1	300	*
O ₂	5	150	< 5
O ₂	2	150	9.7
O ₂	1	150	20.2
O ₂	10	75	16.6
O ₂	5	75	29.7
O ₂	10	50	15.4
O ₂	5	50	19.7
KOH + HCl	60	-	56.1
KOH + HCl	30	-	60.3
Rinsed only	0	0	71.8

Table 4.2 demonstrates that all measured treatments demonstrated improved surface energy as indicated by a reduction in contact angle. This translated to an improvement in bending performance, as demonstrated by the lack of cracking in the plasma treated sample shown in Figure 4.11.

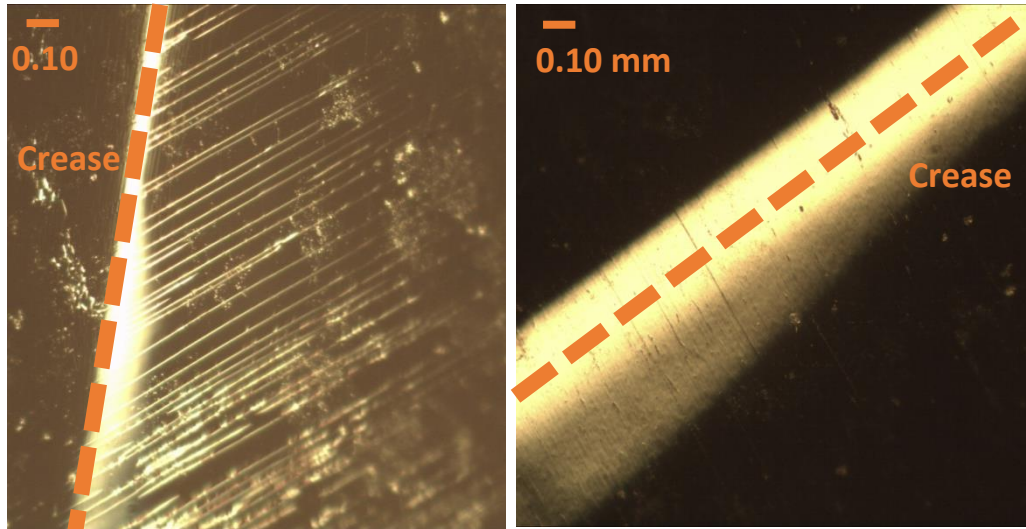


Figure 4.11: Top-lit optical microscopy images of metallized polyimide after bending to a radius of 0.23 mm. Sample at left received no plasma treatment while sample at right received 10 m, 50 W oxygen plasma before titanium deposition. Metal stack: 50 nm Pt/Ir / 50 nm Ti. Orange coloration is due to microscope lighting.

KOH treatments demonstrated only a small improvement in surface energy, and thus were not pursued further. A plot of contact angle vs. time for all other treatments is shown in Fig. 4.xx. It is seen that plasma treatments proved much more effective, and demonstrated increased surface energy with increasing plasma duration and power at least up to 5m and 300 W, in agreement with literature [66, 134]. Plasma duration was not increased further because additional improvements in surface energy could not be detected by the goniometer used, and extended argon plasmas on

polyimide were expected to etch away the surface as it was modified, thus limiting potential benefits. Further, literature suggests that improvements in adhesion to PI level off for similarly high-powered argon plasmas around 5 minutes and begin to drop off if performed much longer than 7 minutes [68].

PI appears to respond more favorably to argon plasmas than oxygen plasmas, as performed for 2 and 5 minutes at 150 W. For treatments of only 1 minute the effects are within experimental error. For the purposes of this work, argon treatment appeared to be superior for another reason: 300 W plasma treatments with argon for durations of 1, 2, or 5 minutes all produced surfaces that were so hydrophilic, and thus energetic, that contact angle could not be accurately measured with the goniometer used. Oxygen plasmas performed at 300W resulted in noticeable blackening of the polyimide surface, which was avoided in order to maintain a known surface.

To test this optimized surface treatment, Linqtape samples were metallized according to the process in Section 1, skipping ALD Al_2O_3 and using a 5 m, 300W plasma before metallization (Plasma 1). These samples appeared to work well considering bend and scratch tests shown previously in Figures 4.7 and 4.11, but Pacific Diabetes Technologies still reported problems with cracking and delamination when attempting to work with devices. Other materials evaluated in parallel with the PI-Ti system showed more promise at this point, and thus further investigation of this interface was put on hold.

4.5 Gold-coated polymer substrates

Commercial options are available for obtaining metallized polyimide films, and several such options were pursued in an attempt to bypass engineering of the PI interface and continue with device fabrication.

4.5.1 Polymer substrates

Sheldahl™, a Multek Corporation brand, provided evaluation samples of BoPET, LCP, and PI, as introduced in Chapter 3, each of which they had treated with a proprietary adhesion-promoting technique and coated with 150 nm of thermally evaporated gold. PDT then evaluated each material by mechanical flex testing (described in Chapter 3.5.3) and imaging.

PDT's findings were that Au/BoPET demonstrated poor Au-polymer adhesion after bending. BoPET also is not preferable for processing in acetone and has a comparatively low maximum temperature tolerance of 200°C, even under gentle physical requirements [143], and thus was not used for attempted device processing. Au/LCP showed superior adhesion compared Au/BoPET, but the LCP substrate itself proved to be rougher and more difficult to process, especially during alignment steps. Au/PI was found to provide superior polymer-gold adhesion and processing compatibility for the purposes of the current work. The biocompatibility of PI has also been previously established [144], further motivating the choice to continue work with PI.

4.4.2 Gold-coated polyimide

Though gold is known to help catalyze the decomposition of H_2O_2 [145, 146], Some of our collaborators (Chris Durgan and Dr. Xiaosong Du with OSU Dept. of Chemical Engineering) determined that the catalytic activity of gold was not sufficient for our application, and thus a catalytic Pt/Ir layer was still necessary. They also determined that 10 nm Pt/Ir was just as effective for catalysis as 50 nm Pt/Ir while requiring less material and reducing device thickness. Figure 4.12 demonstrates the resulting device stack examined in this section.



Figure 4.12: Device stack for Section 4, not shown to scale.

Pt/Ir deposition on a gold surface was not expected to be problematic, but a series of surface treatments were still explored to ensure optimal surface energy before deposition. Gold-coated Kapton samples were affixed with Kapton adhesive tape onto glass slides, rinsed thoroughly with acetone and IPA, dried, and treated (Plasma 1) with a preparation listed in Table 4.3 before taking contact angle measurements. Devices would be patterned for liftoff after receiving initial surface treatments, and exposure to photoresist and developer solutions in this process was expected to modify surface energy. This was addressed by examining the effects of a post-patterning plasma (Plasma 2) on some samples by putting them through the liftoff procedure after the first plasma treatment, except no mask was used so that all photoresist was exposed and developed to leave a bare surface for contact angle

measurement. The second plasma treatment was then applied and contact angle measurements performed. Figure 4.13 displays contact angle measurements for untreated gold and gold after 5 m, 50 W O₂ plasma, simulated liftoff patterning, and 30 s, 50 W O₂ plasma. Table 4.3 and Figure 4.14 display plasma treatments investigated and resulting contact angles.

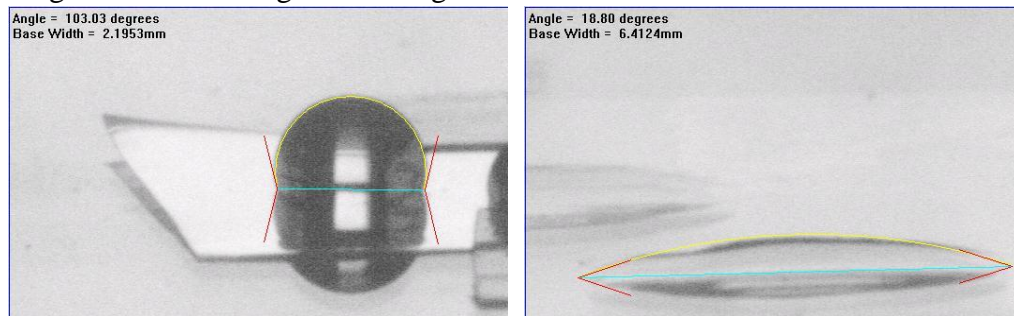


Figure 4.13: Contact angle measurements for (left) rinsed gold and (right) gold treated sequentially with 5 m, 50 W O₂ plasma, simulated liftoff processing, and 30 s, 50 W O₂ plasma.

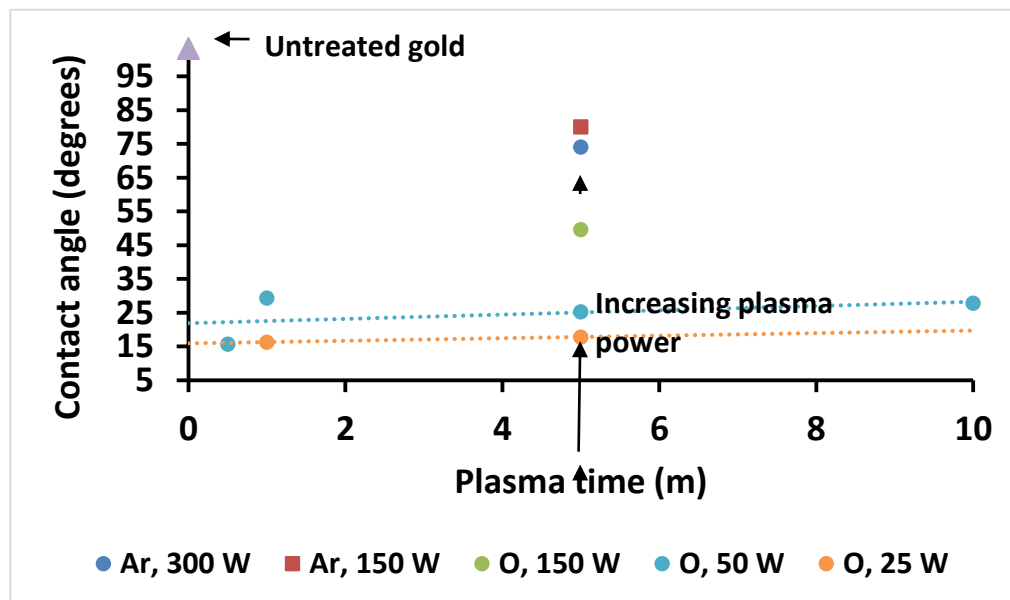


Figure 4.14: Plasma treatment of Au / PI. Contact angle *increases* with increasing plasma power and duration, and is lower for oxygen plasmas than argon plasmas.

Table 4.3: Surface treatments and resulting contact angles for 150 nm gold on 12.7 μ m Kapton polyimide.
Contact angle measurements averaged over three drops per sample.

Plasma 1			Photoresist?	Plasma 2			Contact angle (degrees)
Plasma gas	Time (m)	Power (W)		Plasma gas	Time (m)	Power (W)	
O ₂	0.5	50	-	-	-	-	15.7
O ₂	1	25	-	-	-	-	16.3
O ₂	5	25	-	-	-	-	17.8
O ₂	5	50	-	-	-	-	25.3
O ₂	10	50	-	-	-	-	27.8
O ₂	1	50	-	-	-	-	29.3
O ₂	5	150	-	-	-	-	49.6
Ar	5	300	-	-	-	-	74.1
Ar	5	150	-	-	-	-	80.0
Rinsed only	-	-	-	-	-	-	103.2
O ₂	5	50	Yes	O ₂	0.5	50	19.6
O ₂	5	50	Yes	O ₂	5	25	19.6
O ₂	5	50	Yes	O ₂	1	50	21.9
O ₂	5	50	Yes	O ₂	1	25	22.5
O ₂	5	50	Yes	O ₂	5	50	23.0
O ₂	5	50	Yes	-	-	-	71.0

As with PI, all surface treatments on gold showed a considerable improvement in surface energy compared to surfaces that had only been rinsed. The utility of Plasma 2 was also demonstrated by the large difference in contact angle between a surface treated with Plasma 1 and a surface treated with the same plasma and then exposed to photolithographic processing without receiving a Plasma 2.

While PI responded somewhat similarly to Ar and O₂ plasma treatments, the difference for gold was much more pronounced. Only two Ar plasmas were investigated on the gold surface, but in the case of 5 m, 150 W plasmas, contact angle was nearly twice as high after Ar treatment than after O₂ treatment. Increasing the power to 300 W resulted in even higher contact angle for Ar plasma. This result, combined with a rash of problems with the tool used for Ar treatment, encouraged the use of low powered O₂ plasmas for gold surfaces. The final surface treatment settled on was 5 m, 50 W O₂ for Plasma 1 and 30 s, 50 W O₂ for Plasma 2. Other surface treatments appeared to improve surface energy slightly more than the chosen recipe for Plasma 1, but the 5 m exposure time was expected to be better for breaking up potential organic contaminants. The short time used for Plasma 2 was selected in order to avoid damaging the photoresist pattern.

Devices were made using this new recipe and characterized by bend and scratch testing. All gold devices survived 1 bend around a 26g needle flawlessly, though scratch testing did successfully remove metals from the PI surface, as shown in Figure 4.15. Pt/Ir was never observed to delaminate from gold, however, indicating

that surface treatments at the gold-Pt/Ir interface were facilitating the formation of a strong interface.

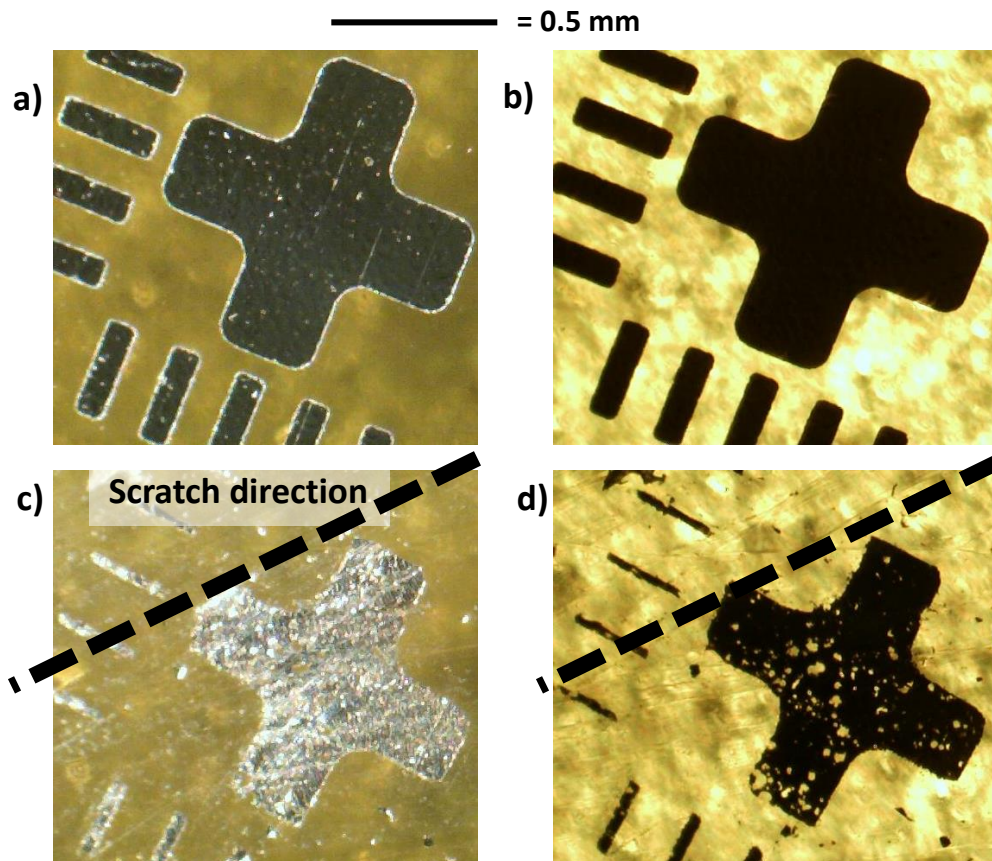


Figure 4.15: Scratch tests performed on 10 nm Pt-Ir / 150 nm Au / 12.7 μm Kapton polyimide. Au surface received 10m, 50 W oxygen plasma before Pt/Ir deposition. Dashed lines are approximately parallel to scratch direction.

a and b) top- and back-lit optical microscope images of unscratched pattern.
 c and d) top- and back-lit optical microscope images of metal pattern after being scratched 20 times with a razor using light pressure.

PDT confirmed the improved quality of Au/PI samples, reporting improved device durability through wrapping and electrochemical testing. Some delamination was observed in certain cases during electrochemical testing, but such instances of delamination were all observed to be near locations where handling damage was present, and thus were attributed to handling accidents. Further device layers, such as

an SU-8 polymer encapsulation layer as explained in Chapter 5, were also expected to help stabilize the metal surfaces for actual sensor construction and use.

4.6 Conclusion

This chapter identified Gel-Pak DGL film as a workable rigidization method for device construction, as it successfully keeps PI samples planar and attached to glass slides through all processing steps while facilitating easy removal after processing. It was found that an Al_2O_3 interlayer appears to be detrimental to mechanical integrity during bending, as devices fabricated without Al_2O_3 demonstrated significantly improved cohesive integrity after bending. Increasing cohesive strength by increasing metal thickness did extend the number of bends required to induce complete electrical failure in electrodes fabricated on Al_2O_3 , but better results were obtained by eliminating the Al_2O_3 layer.

Surface treatments were then explored to optimize adhesion of sputtered Ti to PI, which successfully improved bending and scratch test performance, but was still did not perform sufficiently well for sensor fabrication. Commercially sourced gold-coated polymer substrates were then examined and it was found that of the choices investigated, PI appears to be the most well-suited for the current work. Surface treatments were then optimized to maximize adhesion of Pt/Ir sputtered films to the gold surface. Pt/Ir on gold-coated PI performed well in bend and scratch testing as well as for actual device fabrication and use, allowing device design to proceed (as detailed in Chapter 5).

Secondary observations presented in the course of this work may also warrant future investigation. First, thicker metal layers appeared to improve device resilience to bending when compensating for cohesive failure of underlying layers, which appears to represent an exception to established flexible design wisdom as presented in Chapter 2. Second, it may be useful to review current work and establish a physical basis for why PI and gold surfaces show opposite trends in surface energy resulting from treatment with different plasma gasses, durations, and powers, in order to predict more effectively how those surfaces might be improved and how other materials might react to similar treatments.

5. Process development for sensor fabrication

This chapter presents a process for the fabrication of flexible catheters with integrated glucose sensors, representing the core of the current work. Section 1 describes device layout and gives a high-level overview of the developed process flow. Section 2 describes development and optimization of individual process steps. Section 3 presents characterization of the devices produced by this process, demonstrating mechanical integrity through repeated bending and a linear relationship between glucose concentration and output current. Section 4 summarizes the results of the work presented in this chapter.

5.1 Layout and process flow

Figure 5.1 displays the second mask of the fabrication process, which is simply the inverse of the first mask. This pattern provides the foundation of the entire device and thus serves to represent overall device layout. Specifically, this mask is used for gold etching in the polarity shown (black areas are unetched) and Pt/Ir liftoff in opposite polarity. The complete mask set and previous mask iterations are included in Appendix 1. This section will refer often to Figure 5.1.

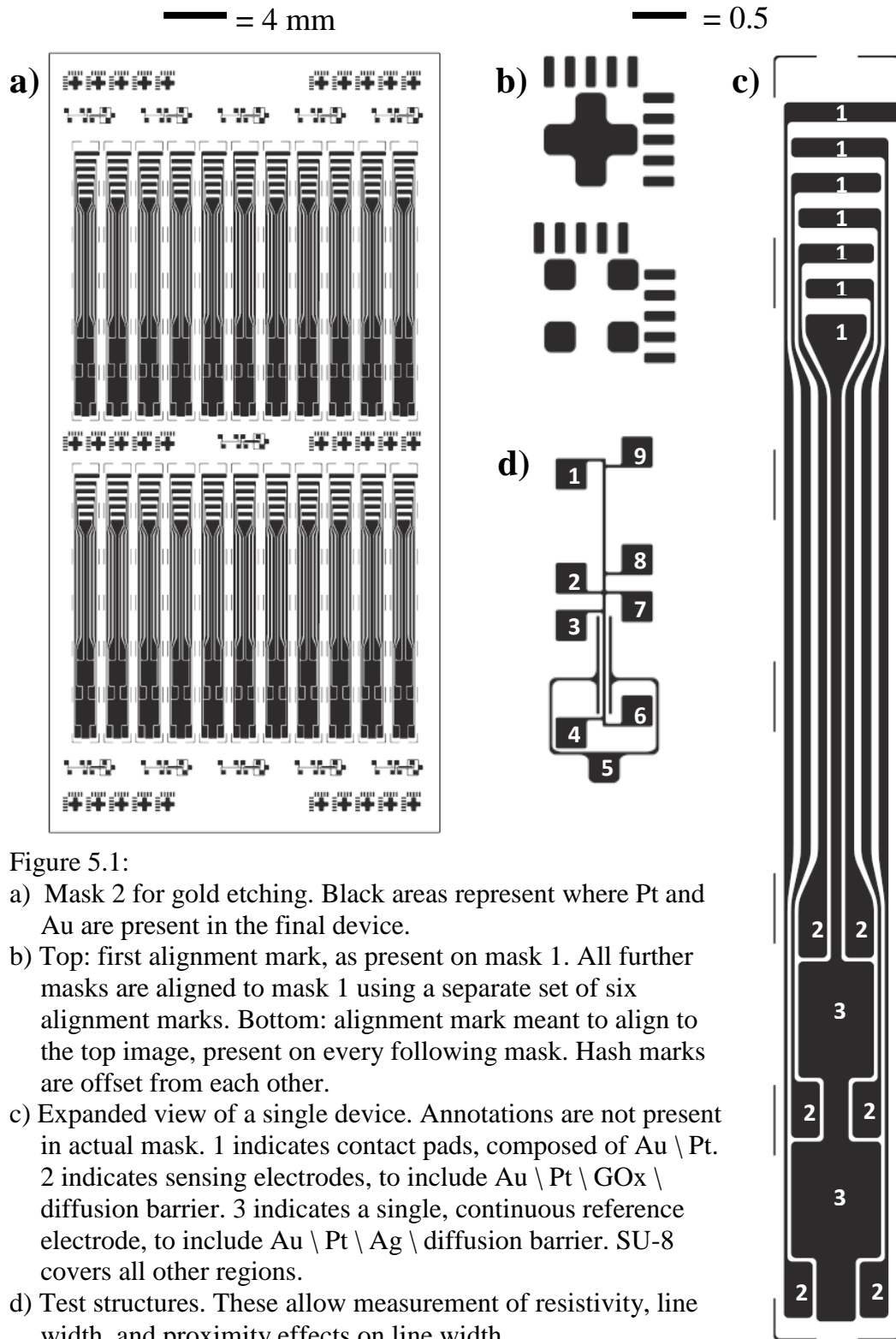


Figure 5.1:

- Mask 2 for gold etching. Black areas represent where Pt and Au are present in the final device.
- Top: first alignment mark, as present on mask 1. All further masks are aligned to mask 1 using a separate set of six alignment marks. Bottom: alignment mark meant to align to the top image, present on every following mask. Hash marks are offset from each other.
- Expanded view of a single device. Annotations are not present in actual mask. 1 indicates contact pads, composed of Au \ Pt. 2 indicates sensing electrodes, to include Au \ Pt \ GOx \ diffusion barrier. 3 indicates a single, continuous reference electrode, to include Au \ Pt \ Ag \ diffusion barrier. SU-8 covers all other regions.
- Test structures. These allow measurement of resistivity, line width, and proximity effects on line width.

5.1.1 Device layout

The regions labeled with a 2 in Figure 5.1c form three pairs of sensing electrodes per individual device. One electrode of each pair generates a signal dependent on both glucose concentration and interferant activity, while the other electrode detects a signal due only to interferants. Ideally, subtracting the interferant signal from the glucose signal will provide a signal that is only dependent on glucose concentration, as described in Chapter 2. Each sensor pair references the same silver / silver chloride (SSC) electrode, labeled 3, but otherwise functions as an independent glucose sensing unit. The redundancy provided by this feature allows for averaging and ensures that the failure of one sensor will not be catastrophic. Failure of the reference electrode would render all sensing pairs unusable, however, and thus the trace to this electrode is both the shortest and widest of the seven traces in each device, making it least prone to failure. The fact that each sensing pair is located at a different implanted depth also allows measurement of glucose concentration as a function of both depth in the subcutaneous layer and distance from the point where glucose-control hormones are introduced. This information will be relevant for the design of future device iterations.

Trace length was chosen such that all three sensing pairs pass through the dermis and are exposed to subcutaneous fluids, based on the intended angle of insertion and average dermal thickness in the human abdomen. Bends and joints in traces comply to a 30 μm minimum local radius of curvature in order to help avoid stress concentration as described in Chapter 2.4.3. Once a crack nucleates, it must spread across the majority of a metal trace before significantly affecting conductivity

[147, 148], and thus the increased trace width in the region between the device contacts and the actual sensing pads is intended to extend device lifetime in addition to decreasing trace resistivity.

Each sensing electrode provides a planar surface area of approximately 0.32 mm², not accounting for rounded corners or surface roughness. The total reference electrode area by the same measurement is approximately 4.74 mm², giving a ratio of 2.47 of reference electrode area to total working electrode area per device. The surface area of the reference electrode is larger than that of the working electrodes in order to reduce the effect of signal degradation or drift resulting from local interactions with trace redox products from the sensing electrodes, as well as to decrease the contact resistance between the reference electrode and subcutaneous fluids.

Two features besides actual devices were included in mask designs in order to aid fabrication. Alignment marks are useful to ensure proper registration between device layers. The first mask lays down a series of alignment marks represented by the top image in Figure 5.1b. This image will be referred to as a “plus.” Each successive mask aligns to a different plus mark using its own mating mark, represented by the bottom image in Figure 5.1b. This image will be referred to as a “box.” Overlaying the box on each successive mask with the appropriate plus laid down by the first mask forms a continuous image, and any misalignment between the mask and coupon will be evident as deformities in this image. The presence of

alignment marks between the two rows of 11 devices allowed fabrication of either one or two sets of devices at once, depending on coupon size and processable area.

Test structures, shown in Figure 5.1d, are included in the overall mask layout in order to assist in characterization of the quality of each deposited layer. This structure includes options for four-point resistance measurements to determine sheet resistance (“Greek Cross” structure, pads 2, 3, 7, and 8), line width (pads 1, 2, 8, and 9), and line width after potential effects from the proximity of nearby features (pads 3, 4, 6, and 7). Pad 5 is included to test for proper isolation between lines, though it could be used for testing capacitance between adjacent lines if high-frequency signals become relevant in later iterations. Test structures similar to these are commonly applied to facilitate statistical process control methods in industry. Measurements made with these structures were not actively applied in this work, but may be used for future process optimization and control.

The contact pad at the top of each trace, represented by a 1 in Figure 5.1c, is intended to be connected to external devices using a proprietary method developed by PDT. Each metal pad is exposed for contact, and the surrounding polyimide is covered by SU-8 polymer.

All device layouts were created using Solidworks 2013 Educational Edition, utilizing scripts created by the author to create rounded corners and smooth transitions in line width.

5.1.2 Process flow

This section presents the developed procedure for production of glucose sensing catheters, and will provide justification for the overall process flow presented in Table 5.1. Optimization of individual steps will be presented in Section 5.2. Devices discussed in the current work underwent processing in MASC facilities before being transferred first to OSU Chemical Engineering for GOx printing and later to Pacific Diabetes Technologies for final processing and testing (as noted in Table 5.1). Images taken after selected process steps are shown in Figure 5.2, and a more detailed run sheet through step 17 is available in Appendix 2.

Table 5.1: Process flow

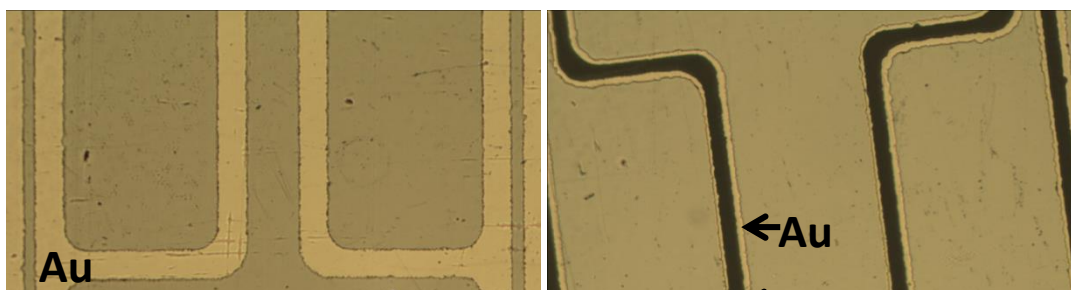
*: Process under development by OSU Chemical Engineering. Process sequence or parameters may change with future work.

** : Process under development by Pacific Diabetes Technologies. Process sequence or parameters may change with future work.

†: Results of this step are imaged in Figure 5.2.

#	Process	Detail
1	Cut material	Begin with 150 nm evaporated gold on 12.7 μm Kapton
2	Rigidize	Apply to glass carrier using Gel-Pak DGL X4 film
3	Clean 1	Sequential rinses with acetone and isopropyl alcohol
4	Plasma 1	5m, 50 W oxygen plasma for activation of gold surface
5	Photo 1	Apply mask for Pt/Ir liftoff
6	Plasma 2	30s, 50W oxygen plasma to refresh gold surface
7	Pt/Ir sputter	Sputter 10 nm of 90/10 at.% Pt/Ir
8 [†]	Pt/Ir liftoff	Sonicate in acetone to remove Pt/Ir
9	Clean 2	Sequential rinses with acetone and isopropyl alcohol
10	Photo 2	Apply mask for gold etch
11 [†]	Etch 1	Gold etch, KI-based etchant
12	Clean 3	Sequential rinses with acetone and isopropyl alcohol
13	Ag evap.	Evaporate 200 nm silver
14	Photo 3	Apply mask for silver etch
15 [†]	Etch 2	Silver etch, base piranha solution
16	Clean 4	Sequential rinses with acetone and isopropyl alcohol
17 [†]	Photo 4	SU-8 application and patterning
18*	Chloridize	Partially chloridize Ag with FeCl_3
19*	GOx print	Apply GOx using EDHP
20*	iGOx print	Apply inactive GOx using EDHP
21*	PFSA spin	Deposit PFSA diffusion barrier
22**	PDMS spin	Deposit silicone protective barrier
23**	Wrap	Apply proprietary wrapping method
24**	Connectorize	Apply “clothespin” connectors
25**	Fixturing	Mount sensors for use

— = 0.2 mm



Previous chapters detailed the process that eventually led to the use of Kapton of the thinnest thickness commonly available, 12.7 μm , coated with 150 nm of thermally evaporated gold by Sheldahl™ (step 1 in Table 5.1). This material is received as a flexible film, and thus in the developed process this film is first rigidized for processing (step 2), utilizing a glass slide to carry samples through the

fabrication process. The gold surface is rinsed sequentially with acetone and isopropyl alcohol (3) to dissolve or mechanically rinse away surface contamination and then exposed to an oxygen plasma (4) as developed in Chapter 4 to remove further organic contaminants and activate the gold surface for Pt/Ir adhesion. S1818 positive photoresist is then spun onto the gold surface and exposed to UV light through the inverse of Mask 2, shown in Figure 5.1, and exposed regions are then selectively removed using a developer solution (5). A second, quick oxygen plasma (6) is then used to “refresh” the surface energy of the exposed portions of the gold surface. This second plasma step, also motivated in Chapter 4, was kept short to avoid damaging the photoresist pattern.

10 nm of Pt/Ir is then sputtered across the entire sample (7) and unwanted material is removed by sonication in acetone (8), washing away the S1818 liftoff mask and removing the Pt/Ir adhered to it. Pt/Ir deposition and patterning is performed before gold etch in order to ensure a highly planar surface for Pt/Ir patterning and liftoff, as liftoff processes are generally more sensitive to resist uniformity than wet-etch, though the presence of a 150 nm step was not expected to be significant. This also guaranteed that Pt/Ir would not be deposited on bare polyimide, avoiding the adhesion problems that would likely result. After Pt/Ir liftoff, samples are rinsed again with acetone and isopropyl alcohol (9) and patterned for gold wet etch (10). Gold etching is then accomplished using a KI-based etchant (11), samples are cleaned using the same solvent rinse as used previously (12), and a blanket of 200 nm of silver is evaporated across the entire substrate (13). S1818 is

applied again to pattern mask silver for wet etching (14), and silver is etched with a “base piranha” solution of 1:1:27 H_2O_2 : NH_4OH : DI water (15). Another solvent rinse is performed (16) before applying and patterning SU-8 polymer (17) for passivation and well formation for GOx printing.

Chris Durgan, Xiaosong Du, and others in Dr. Greg Herman’s lab in the OSU Chemical Engineering department continue device fabrication by performing Ag chloridization by exposing the sample surface to FeCl_3 for an amount of time calibrated to chloridize half of the available silver (18), forming a functional Ag/AgCl reference electrode. Active and inactive GOx enzyme is then printed onto working electrodes (19 and 20), though the deposition process for inactive GOx enzyme is still under development. (Active GOx generates detectable H_2O_2 from glucose in the body, as discussed in Chapter 2.. The entire device excluding contact pads is then covered with an approximately 7 μm layer of PFSA deposited from a spun solution of 30 wt.% PFSA (21) to create a layer to selectively control diffusion of glucose and thus avoid current saturation. This layer also serves to help block potential interferents.

Pacific Diabetes Technologies (PDT) then applies a silicone, glucose-permeable passivation layer (22) to protect the entire device against mechanical damage. After this final device layer is applied, devices are wrapped into cylinders (23) using a proprietary method developed by Peter Hannaway and PDT. Electrical contact is then made using a proprietary “clothespin” method (24) that involves clamping a specially-designed connector onto device contact pads and applying a Z-

axis conductive adhesive material. Finally, completed devices are mounted on needles for implantation (25).

The functions of each material listed are described in Chapter 2.2, while the optimization of individual steps follows in Section 2.

5.2 Process development

Rigidization solutions and substrate materials were selected in Chapter 4. This section presents the development of process steps to take gold-coated polyimide and turn it into a finished device.

5.2.1 Metal deposition

Pt/Ir was deposited via sputtering by Tyler Klarr or Dr. Xiaosong Du. Initially, the maximum allowed sputter power (300 W) was applied to generate the plasma for Pt/Ir deposition, intending to maximize deposition rate to save time and avoid incorporation of potential contaminants. Blanket samples of polyimide demonstrated significant induced curvature after high-power deposition, however, and concerns were raised about causing potential crystallization of the target material. Deposition power was halved for the final process in order to reduce induced strain and to avoid damaging the target.

The final Pt/Ir thickness of 10 nm was chosen after mechanical and electrochemical testing performed by Chris Durgan, Dr. Xiosong Du, and Matt Bates, along with some automated tests performed at PDT. Devices were fabricated using 0, 10, 30, and 50 nm of Pt/Ir on Sheldahl samples of 150 nm gold on 12.7 μm Kapton. Each preparation was tested for mechanical stability by being either bent on an

automated flex tester, soaked in a phosphate buffer solution (PBS) while under 0.6 V bias relative to a grounded electrode placed in the PBS solution, or first soaked under bias and then bent. Further, each preparation was tested in a hydroxide solution in order to measure resulting oxidation current. Results indicated that all samples performed similarly in mechanical tests, while all preparations that included Pt/Ir showed similar oxidation currents much greater than those observed for uncoated gold. 10 nm Pt/Ir was thus selected to keep the metal stack thin and preserve source material.

Silver was deposited using a straightforward thermal evaporation process as described in Chapter 3.2.1. Silver thickness of 200 nm was chosen in order to keep the silver layer thin and flexible while remaining thick enough to facilitate creation of a reliable Ag/AgCl reference electrode, as the lifetime of this electrode is related to the amount of material available to be consumed by the reaction described in Chapter 2.2.4.

Silver chloridization was performed by Chris Durgan and Dr. Xiaosong Du, who determined that an approximately 50 s exposure to FeCl_3 should be sufficient to chloridize approximately 100 nm of silver. Silver thickness and chloridization ratio may both be adjusted depending on the performance of the SSC electrode in further studies.

5.2.4 Patterning

As discussed in Chapter 3.3, photolithographic patterning can be used to create masks for both liftoff and etch patterning, and both types of patterning were utilized

in the final fabrication process. Shipley S1818 positive photoresist was applied in both cases, but recipes differed as described below.

A standard recipe for wet etch masking on silicon or other rigid substrates was available for use, and required only slight modification for application to polyimide. Deviations from planarity present in rigidized polyimide samples cause a spun photoresist layer vary in thickness across a substrate. Increasing ultraviolet exposure dose by approximately 14% by increasing exposure time from the prescribed 7 s to 8 s helped ensure complete exposure of thicker regions. Larger UV doses were not demonstrated to be problematic for wet etch, as feature size did not change appreciably. Instead, larger doses had the added benefit of helping to negate the effect of edge beading, where surface tension causes spun resist to build up at the edge of a coupon. Longer exposure times cause even these thicker regions to become soluble to developer, thereby expanding the available patternable area per coupon. Effects of frequent photoresist use by other MASC users later required a further increase of exposure time to 9 s to compensate for solvent evaporation and concentration of the photoresist solution, which led to thicker spun resist layers. The final wet etch masking process parameters, applied for masking of both gold and silver layers, is given in Table 5.2 below. Figure 5.3 displays sidewalls generated by this method, demonstrating well-defined edges and near-vertical sidewalls.

Table 5.2: Wet etch masking recipe

Process step	Parameters
Spin S1818 photoresist	3000 RPM, 5000 RPM/s ramp, 30 s
Pre-exposure bake	3 m at 85 °C
Exposure	9 s
Post-exposure bake	3 m at 85 °C
Develop	~30 s in 1:4 315 developer : DI water
Rinse and dry	Rinse with DI water, blow dry with N ₂

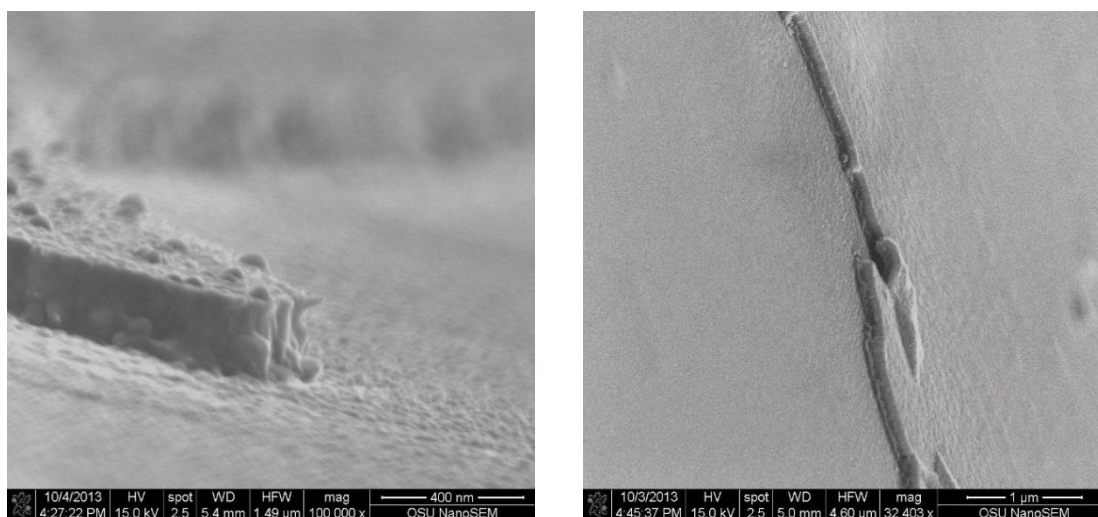


Figure 5.3: Results of wet etching of Ag on Au (left, scale bar 400 nm) and Au on PI (right, scale bar 1 μ m) masked by the recipe given in Table 5.2 and etched as explained in Section 5.2.4. Lumpy appearance of Ag material is a relic of sample preparation. Images are taken at patterning defects to image edge slope.

Au

Liftoff patterning required more optimization than wet-etch patterning. Positive photoresist produces a sidewall profile that is not ideal for liftoff processing

(explained in Chapter 3.3.2), and thus care was required to optimize process

Au

parameters to compensate. First, in order to ensure easy photoresist removal, pre-exposure bake was reduced to 1 m so that some solvent would remain in the resist.

This was the minimum amount of time required to prevent sticking between the photoresist layer and a photomask. Nitrogen gas was blown across the resist surface after baking in order to dry out the surface and further discourage sticking. Sidewall slope increases with exposure time, so exposure dose was minimized, using an exposure time of 6.5 s plus an extra 1 s in cases where old resist or other factors resulted in incomplete development. Post-exposure bake was skipped entirely, again in order to leave the resist in an easily-removed state, and development time was minimized to approximately 20 s in order to maintain tall sidewalls and reduce sidewall sloping. The resulting recipe, applied Pt/Ir liftoff, is given in Table 5.3. Figure 5.4 presents an etch profile generated by this recipe.

Table 5.3: Liftoff patterning recipe.

Process step	Parameters
Spin S1818 photoresist	3000 RPM, 5000 RPM/s ramp, 30 s
Pre-exposure bake	1 m at 85 °C followed by N ₂ dry
Exposure	6.5-7.5 s
Post-exposure bake	-
Develop	~20 s in 1:4 315 developer : DI water
Rinse and dry	Rinse with DI water, blow dry with N ₂

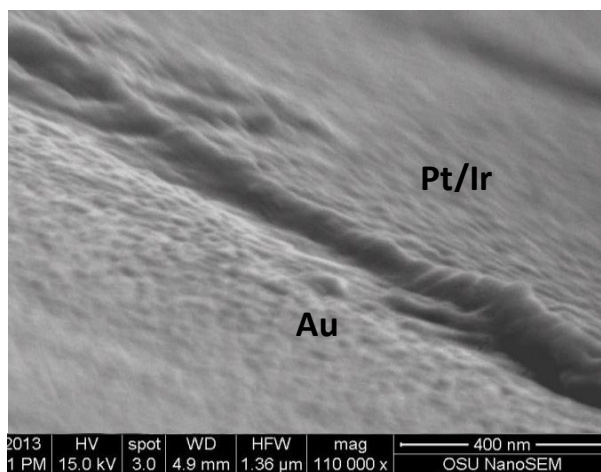


Figure 5.4: Edge resulting from liftoff of Pt/Ir on an Au surface. Pt/Ir, only approximately 10 nm thick, is visible only due to the presence of “fences” of peeled-up material at pattern edges, as expected from liftoff processing.

5.2.5 Etching

Wet etch chemistries are presented in Chapter 3.3.2. Wet etch recipe development was straightforward, applying recipes found in literature with proper dilution by DI water to generate etch times of approximately 1 m for the metal thicknesses used. No successful wet chemistry was found to etch Pt/Ir, however.

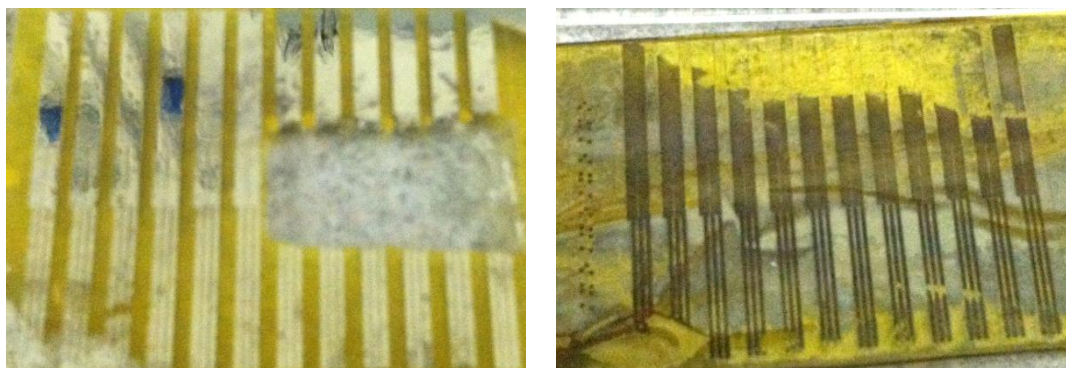


Figure 5.5

Left: Devices after successful Pt/Ir and Ti etches. Removed section was used for SEM.

Right: Devices after unsuccessful Ti and Pt/Ir etch. Dark, silvery residue was determined to be due to Pt/Ir redeposition. Dark color of device pattern is due to nearly etching away the entire device stack from extended dry etching. Bright area is bare polyimide where residue has been wiped away with a latex glove.

Etching via ion bombardment was attempted for patterning of Pt/Ir, but resulted in extensive Pt/Ir redeposition as shown in Figure 5.5. The observed failure of each of these methods motivated use of liftoff processing for Pt/Ir.

5.2.6 Passivation and well formation

Once metal deposition was complete, a layer of SU-8 polymer was deposited for passivation and well formation as described in Chapter 3.1.5. SU-8 thickness was optimized to be thick enough to provide effective boundaries for GOx deposition via EDHP printing while not being thicker than necessary in order to preserve effective

bending performance. SU-8 thickness was tuned to approximately 2 μm by selecting an appropriate formulation (SU-8 2) and adjusting spin speed as recommended by Microchem Corp.

The standard SU-8 recipe was found to produce poor adhesion to polyimide and would fracture or bubble after deposition, assumed to be due to thermally induced stress. Adhesion was improved by more than doubling exposure time, from 9 s to 20 s, and increasing post-exposure bake to encourage strong cross-linking of SU-8 polymers. Thermal stresses were reduced first by adding 1 m warm-up and cool-down steps to each baking step and second by covering samples with a plastic lid during heating in order to reduce temperature differentials between substrate and ambient conditions. Also, samples were allowed 1 m to cool to ambient temperature before submersion in developer solution. The resulting recipe is given in Table 5.4. The result of these optimizations was a visibly uniform, flexible, and resilient layer, as shown in Figure 5.2. SU-8 sidewalls are displayed in Figure 5.6.

Table 5.4: SU-8 recipe, optimized for adhesion to polyimide.

Process step	Parameters
Spin S1818 photoresist	500 RPM, 100 RPM/s ramp, 10 s, then 2000 RPM, 300 RPM/s ramp, 30 s
Pre-exposure bake	1 m at 65 °C, 3 m at 95 °C, 1 m at 65 °C
Exposure	20 s
Post-exposure bake	2 m at 65 °C, 1 m at 95 °C, 1 m at 65 °C, 1 m at ambient temperature
Develop	40-50 s in SU-8 developer
Rinse and dry	Rinse with IPA, blow dry with N ₂
Hard bake	15 m at 115 °C

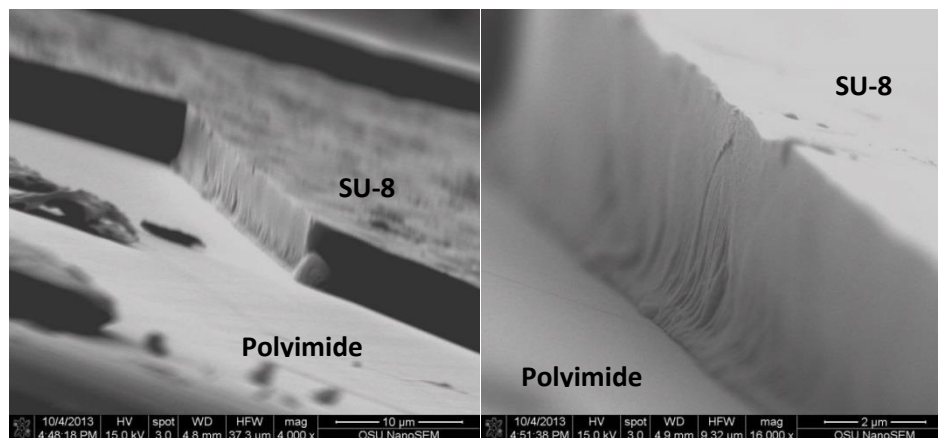


Figure 5.6: SU-8 topology, displaying vertical sidewalls, clean edges, and a relatively smooth surface. Imaged SU-8 is $\sim 7 \mu\text{m}$ thick, but this layer was reduced to $2 \mu\text{m}$ in the final process.

In addition to electrical isolation, chemical passivation, and well formation for GOx deposition, SU-8 was expected to help place active layers closer to a stress-neutral region during bending. Samples with and without SU-8 layers were bent by hand around a 26g needle as described in Chapter 3.5.3, and results are presented in Figure 5.7. Older Pt/Ir on Ti samples were used for this test instead of gold to conserve gold-coated material.

The results in Figure 5.7 clearly demonstrate an improvement in resistance change with bending, especially for wide traces. The only difference between the samples investigated is the presence or absence of SU-8, indicating that this improvement demonstrates the stabilizing effect of SU-8.

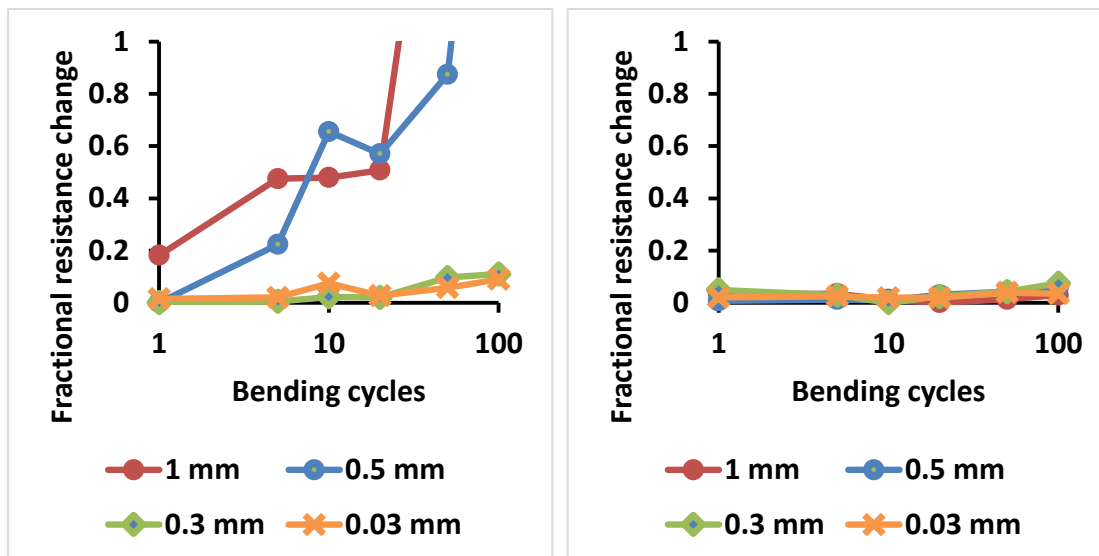


Figure 5.7: Average change in electrical resistance for 8 mm long traces of multiple widths after repeated bending of samples without (left) and with (right) a 2 μm layer of SU-8, demonstrating the utility of SU-8 in stabilizing a metal stack under mechanical stress. Each graph represents the average of 6 traces of 1.0 and 0.5 mm width, 12 traces of 0.3 mm width, and 18 traces of 0.03 mm width. Resistance change is normalized by unbent resistance values, and negative values are assumed to be due to noise and set to zero. Bending was performed by hand around a 18g needle, inducing tensile strain in the metal layer. Device stack: 50 nm Pt/Ir / 100 nm Ti / 25 μm Kapton.

5.2.7 Glucose oxidase and diffusion barrier

Chris Durgan and Dr. Xiosong Du experimented with ink compositions and deposition parameters in order to develop a method for depositing active GOx via electrohydrodynamic printing (EDHP). The recipe developed for the current work results in highly uniform GOx layers with well-defined edges, producing patterns such as those displayed in Chapter 3.2.3.

Chris Durgan and Dr. Xiosong Du have also evaluated formulations of sPEEK and PFSA for use as diffusion barrier materials. Their work has determined that a 30 wt.% formulation of PFSA spun at 1700 RPM on top of printed GOx provides

superior linearity in electrochemical response over the desired glucose concentration range as well as high selectivity against interference by acetaminophen, as demonstrated in Figure 5.8. This result was achieved after testing a range of recipes for both GOx and diffusion barrier deposition, including different material compositions and deposition parameters. The linear relationship between output current and glucose concentration enables straightforward interpretation of sensor output, and the selectivity for glucose over acetaminophen helps ensure that output is representative of only glucose concentration. This figure also serves to demonstrate the effectiveness of these devices in sensing glucose overall, though an external reference electrode was used for the data displayed as use of the internal SSC is still

under development.

The thickness of the spun PFSA layers is approximately 7 μm , which is on the order of the substrate thickness. Depending on the mechanical properties of PFSA, and assuming that layers this thick do not fracture when bent, the PFSA layer may aid the SU-8 in helping to place the active device layers in a stress-neutral zone.

5.2.8 Device encapsulation and fixturing

PDT is developing a method to apply a silicone protective layer that will further protect the final product from mechanical damage while still allowing glucose diffusion. Further, they have developed a method of cutting devices from a coupon

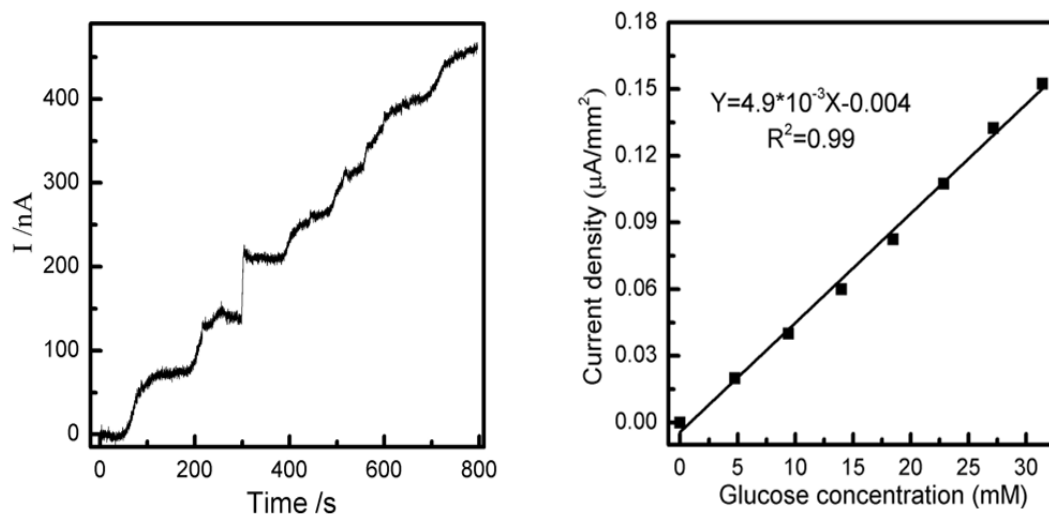


Figure 5.8: Output of a planar sensor as a function of glucose concentration. Sensor was placed in PBS solution and biased at 0.6 V with respect to an external SSC electrode and drops of glucose were added over time. 0-30 mM covers the entire clinically relevant range of glucose concentration. Credit Dr. Xiaosong Du and Chris Durgan.

Left: Absolute current as a function of experimental duration.

Right: Current density as a function of glucose concentration, showing a very linear response to added glucose.

and rolling them into sealed catheters, as well as a method of electrical connection utilizing a z-axis conductive adhesive. Finally, once devices have been encapsulated, rolled, and electrically connected to a breakout board, PDT will mount them on a needle for implantation. These techniques are proprietary and still under development, and thus are not presented in detail here.

5.3 Durability characterization

The electrical response to glucose concentration demonstrated in Figure 5.8 demonstrates that the device developed in the present work successfully detects glucose as intended, though further work needs to be done to test the SSC reference electrode to verify that the device can operate as a self-contained unit. Fabrication and use of integrated SSC reference electrodes are well established, so obtaining a functional SSC is expected to be straightforward. In order to examine whether devices are likely to continue functioning after bending, insertion into a body, and exposure to mechanical stresses while in the body, automated flex testing was performed on devices that had been completed through SU-8 deposition (step 17 in Table 5.1). These devices mostly survived over 62,000 bending cycles at a bend radius of 1 mm and bending rate of 150 cycles per minute, though one trace out of 50 failed at 10 bends, and three more failed at 10,000 bends due to handling errors. Figure 5.9 displays the electrical results of these bend tests, and Figure 5.10 displays optical microscope images taken before and after bending.

The fact that 46 out of 50 traces examined remained within 3% of their initial resistance value after more than 60,000 bends gives strong evidence of their

mechanical resilience. The 50 traces examined, specified in the caption to Figure 5.9, are the longest and therefore most failure-prone traces in each device. The images in Figure 5.10 depict the device that showed the most apparent damage out of all devices examined, and even in this case – as well as all others examined – no complete cracks were observed in the imaged regions, though top-lit images indicate that hairline cracks (or possibly scratches) may occur in the Pt/Ir devices. In order to ensure that devices were not simply cracked and pushed back into contact with each other, as likely occurred for the one failed trace at 10 bends, resistance measurements taken at 10,000 bends and onward were done while pulling the device apart so as to separate any cracked regions.

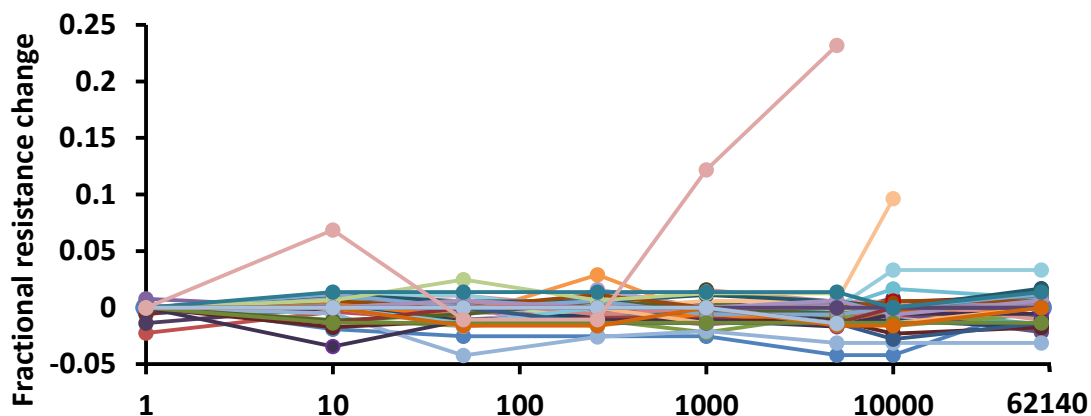


Figure 5.9: Fractional resistance change for traces on a coupon patterned as displayed in Figure 5.1, processed through SU-8 deposition (step 17 in Table 5.1). The 4 longest traces to working electrodes plus the reference electrode were measured across 10 devices, for a total of 50 examined traces. After 62,140 bending cycles, only 4 traces displayed a resistance change in excess of 3% of their starting value, and these were likely the result of handling errors that occurred at 10 and 10,000 bending cycles.

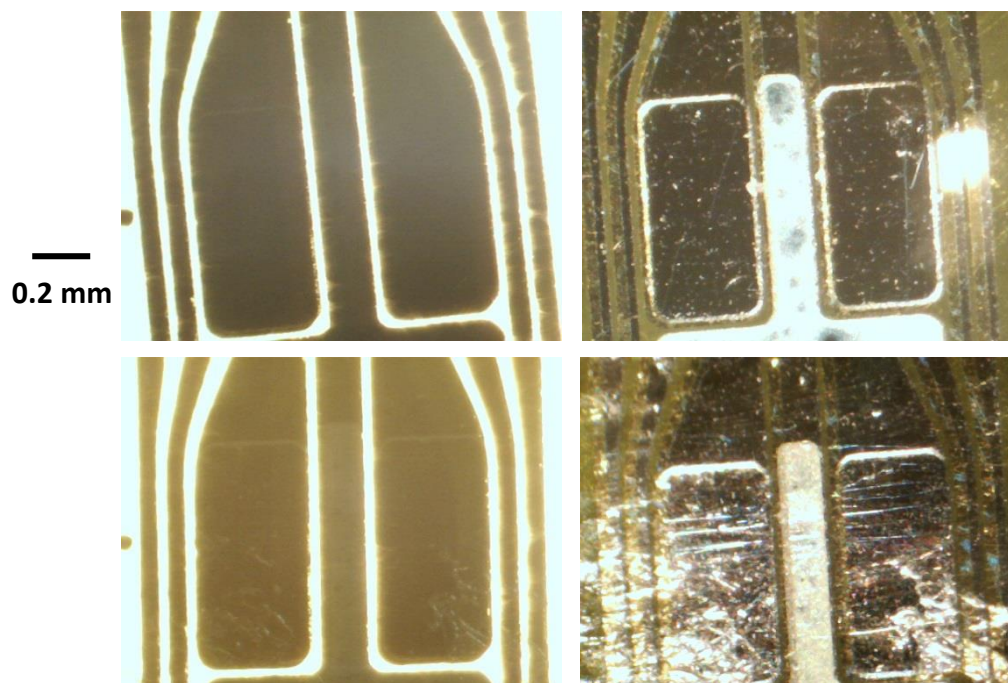


Figure 5.10: Optical microscopy images before and after repeated bending. Top images are before bending, bottom images are after 62,140 bending cycles. Left images are back-lit, right images are top-lit. Displayed images show the most damage of any device investigated. Though devices are obviously worse for wear and some hairline cracks or scratches are visible from top-lit images, backlit images show that no cracks appear to extend through the entire device.

5.4 Conclusion

Collaboration between OSU Electrical and Computer Engineering as represented by the author, Dr. Souvik Kundu, and Dr. John Conley; OSU Chemical Engineering as represented by Chris Durgan, Dr. Xiaosong Du, and Dr. Greg Herman; and PDT has resulted in the development of functional process to produce the foundation for flexible, implantable glucose sensing catheters. These devices have been demonstrated to provide linear glucose response across the clinically relevant range of glucose concentrations, and have been shown to survive repeated bending from planar form to a 1 mm bend radius for at least 62,000 bending cycles. It should be noted that each cycle represents 2 instances of bending and returning to a planar state, effectively indicating that most devices survived 124,000 individual bends – hopefully, this is much more mechanical stress than will occur in actual application.

Work still remains to finalize these devices, and some directions for such work are presented in Chapter 6.2.

6. Summary and Future work in flexible electronics

Work presented in the preceding chapters describes investigation into fabrication techniques for flexible devices, culminating in the design of a flexible glucose sensor and catheter. The foundation of this catheter has been proven to be mechanically resilient, and devices in a planar form have proven to successfully generate an electrical signal with a linear dependence on glucose concentration throughout the clinically relevant range. This work indicates that the most significant challenges in fabrication of a flexible glucose sensor have been overcome, but work remains to prove functionality of the finalized devices. Work leading up to the creation of this device has also indicated a number of directions for more general research. Section 1 of this chapter provides suggestions to investigate trends identified in Chapter 4. Section 2 describes potential design and process optimizations for future iterations of the fabrication process presented in Chapter 5, and Section 3 briefly addresses ongoing work aiming toward the realization of a full artificial endocrine pancreas.

6.1 Further investigation of metal/polyimide adhesion

Chapter 4 provides evidence that Al_2O_3 films deposited by a standard TMA- H_2O ALD process should be used only in devices that are not intended to tolerate curvature radiuses approaching the critical bend radiuses identified in [140]. Cracking in the Al_2O_3 layer appears to negate any adhesive benefits and assumedly destroys functionality as a passivation layer, and further experiments would be helpful in better characterizing these effects. Such experiments could explore whether the adhesive benefits of Al_2O_3 are actually lost at the critical bend radius reported by

George's group, and thereby investigate the utility of critical bend radius as a metric for flexible device design. Another option would be to generalize the relationship between adhesive quality and critical bend radius to other material systems.

Chapter 4 also provides evidence that thinner metal layers do not always improve bending performance in a device, as the increased cohesive strength of thicker layers can compensate for failure in underlying layers. Further research could better characterize the material system observed here; other material systems could be explored to generalize the current results; or new work could identify an optimal thickness for metal layers on brittle substrates, balancing the benefits of increased cohesive strength with increased stress within a layer.

Chapter 4 ended with an investigation the capabilities of available facilities for adhering titanium to polyimide surfaces. This is a relatively well-studied topic [66, 68, 149, 150], but it may be useful for the MASC lab to continue to explore surface treatments on polyimide to establish capabilities for expanded processing of flexible devices. In particular, literature has demonstrated the utility of in-situ plasma cleaning of a substrate before sputter deposition, known as reverse sputtering [66, 68, 151–154], for improving surface energy and adhesion for these and similar surfaces.

6.2 Improvements in glucose sensor design and processing

6.2.1 Mask layout

The current mask iteration presented in Figure 5.1 and Appendix 1 utilized a 50 μm minimum feature size. 30 μm minimum feature size proved to be too narrow to lift off thick metal layers (maximum 50 nm Pt/Ir / 700 nm Ti) with the simple liftoff

process used in the current work, but the use of only 10 nm Pt/Ir should allow the minimum feature size to be reduced again if desired. Other liftoff methodologies described in Chapter 3.3.2 utilizing negative resists and two-step processes would also allow smaller feature sizes, even for thicker layers.

Misalignment tolerances should be adjusted before final device production in order to ensure reproducibility for large-scale production. Observations made during early iterations indicated that $\pm 10 \mu\text{m}$ tolerances in both planar dimensions were larger than necessary, and no problems were anticipated or observed to result from minor misalignments. Because the addition of misalignment tolerance renders less surface area usable for sensing on the final device, the decision was made to omit misalignment tolerance in the current device iteration. Misalignment tolerances can be reintroduced once information has been collected on the amount of surface area that can be used for this purpose.

The current mask set uses inverse polarities of the same photomask for both Pt/Ir liftoff and Au wet etching. These different patterning methods result in different feature sizes for the same exposed area, causing Pt/Ir features to be narrower than the corresponding Au features beneath them. This is beneficial in that it introduces several microns of misalignment tolerance, but it does not allow feature size and misalignment tolerance to be tuned separately. Creating separate masks for each process would decouple control of each feature. Further, separate mask designs would allow deposition of Pt/Ir only on sensing electrodes instead of throughout the entire device if desired for future iterations.

6.2.2 Processing

In-house deposition of polyimide films may be worth investigation. This would increase process control by allowing substrate customization, would reduce dependence on external processes, could potentially lower production costs, and may provide a rigidization solution that improves upon the planarity and process compatibility currently provided by Gel-Pak DGL film. Literature provides a range of PI formulations for reference, meaning that this would not require extensive original research.

Liftoff processing by any method tends to leave vertical “fences” of partially removed material at feature edges, often requiring industrial processes to introduce planarization steps. These structures have not been shown to be problematic in the current work, but may represent points where delamination could begin, may interfere with planarity, or may generate metal flakes that migrate through subsequent processing steps. Liftoff processing could be avoided altogether with an appropriate etch process, as attempted but not accomplished in the current work. There are no known wet etchants for Pt/Ir other than aqua regia, but the use of reactive process gases (and a suitable resist) for dry etching and ion bombardment remains a possibility.

Test structures were included in the presented mask set in order to characterize the quality of deposited metal layers. These were not employed in the current work, as simple four-point probe measurements sufficed to evaluate metal quality. Test structures deposited and patterned as actual devices may be a more informative tool

to analyze metal sheet resistance and line width for the purposes of large-scale production, however.

6.3 Toward an artificial pancreas

The true test for the devices developed in the current work will be actual application to glucose sensing in living bodies, first in pig tests scheduled to begin in early 2014 and later in clinical trials with human patients. The ultimate goal is to facilitate creation of a complete artificial pancreas, which is obviously composed of more parts than a catheter and sensor. Work continues at Pacific Diabetes Technologies to address the other components of this project, including an automated device wrapping solution and connectorization scheme, development of control electronics to process the electrical output of the current work, and methods to deliver glucagon and insulin to the developed catheter.

7. Modeling Atomic Layer Deposition in Porous Substrates

This chapter describes the development of a model to describe the penetration of ALD precursors into aerogel structures. This chapter exists mostly independently of the other work presented in this thesis. Section 1 of this chapter briefly motivates the work to follow. Section 2 describes the importance of ALD in cellulose nanocrystalline aerogels and describes prior work in modeling ALD processes in high-aspect-ratio structures. Section 3 extends prior work by describing a model for ALD of aluminum oxide (alumina, or Al_2O_3) in aerogels. Section 4 describes testing of the developed model against actual Al_2O_3 deposition in carbon nanocrystal (CNC) aerogels, and Section 5 describes the results of these experiments. Sections 3-5 detail work that has been submitted for publication and co-authored by the current author. Section 6 presents potential areas of future inquiry on this topic.

7.1 Introduction

ALD, as described in Chapter 3.2.2, is unique among material deposition technologies for its ability to produce extremely highly conformal and high quality films [114, 115, 117]. These qualities motivate the use of ALD in a range of applications separate from traditional electronics manufacturing, including protection of jewelry against tarnishing [116, 155] and enhancement of the biocompatibility of artificial implants [156]. Further novel applications of ALD are the subject of current research [116, 155]. One such application is the protection of aerogels composed of cellulose nanocrystals (CNCs) against oxidative decomposition. The current work develops a model to facilitate ALD in this application.

7.2 Background

7.2.1 Aerogels and other porous materials

Porous materials are valued for their high ratio of surface area to volume, causing such materials to be of interest for applications including supercapacitors [157–159] or catalytic materials in sensing or filtering applications [160–162]. Further, porous materials either contain trapped gasses or force gasses to flow in along extremely tortuous paths, thereby tending to provide excellent thermal insulation [163–166].

Aerogels are a form of highly porous material that also offers high strength to weight ratios, depending on composition. Aerogel structures have been fabricated from silica, carbon, alumina, and other materials by replacing the liquid components of an appropriate gel with gas via supercritical drying [167]. This work focused on aerogels formed from solution-processed carbon nanocrystals (CNCs), which have been widely suggested for use as additive reinforcements in polymer materials [168, 169]. CNCs are known to be sensitive to oxidation, however, and application as a polymer additive typically requires temperatures that are likely to destroy unprotected CNC aerogels [170].

Oxidation is not a concern if a material will not be exposed to oxygen, however, motivating deposition of an oxygen diffusion barrier to prevent oxidation of CNC aerogels. Oxygen diffuses easily through many materials, and thus fabrication of a conformal barrier to prevent oxygen diffusion is not a simple task. The low thickness and high quality and conformality of this application motivating the use of ALD for this purpose. Previous work has investigated ALD coatings to protect other

carbonaceous structures against oxidation, in one case increasing the oxidation onset temperature of carbon fibers by 60 °C [171].

The standard ALD cycle, described in Chapter 3.2.2, must be modified somewhat to account for diffusion time in complex substrates. An exposure or “soak” step can be added after precursor introduction (pulse) and before excess precursor removal (purge) to facilitate this diffusion, and a longer pulse is also required to coat the greater surface areas involved and to drive diffusion into the porous structure. A longer purge is also required to allow excess precursor to diffuse back out to avoid gas-phase precursor interactions. Temperature, pressure, and other parameters unique to each process also affect optimal pulse, soak, and purge times, making process optimization a non-trivial affair. Materials and tool time required for experimental arrays can be expensive, thus motivating development of a method to model ALD in nanostructured substrates.

7.2.2 Atomic layer deposition in porous substrates

Roy G. Gordon *et al.* in 2003 described the requirements for complete coverage of a surface by ALD and developed a model describing the exposure required to achieve these conditions for planar surfaces and substrates with cylindrical pores [172]. This work concluded that the exposure necessary for one ALD pulse to achieve complete coverage of a cylindrical pore, $(Pt)_{total}$, could be expressed as

$$(Pt)_{total} = S\sqrt{2\pi mkT}[1 + (19/4)a + (3/2)a^2] \quad (\text{Eq 7.1})$$

where P refers to precursor partial pressure, t refers to exposure time, and the product $(Pt)_{total}$ refers to precursor dose in Langmuirs, where 1 Langmuir = 10^{-6} torr s. S then

refers to the saturation dose, or dose of precursor material required to coat an entire surface expressed in molecules per m^2 ; m is the molecular mass of the precursor in kg; k is Boltzmann's constant ($1.38 \times 10^{-23} \text{ J K}^{-1}$); T is the absolute temperature; and a is the aspect ratio of the cylindrical pore, defined by $a = Lp/4A$ where L is the depth, p the perimeter, and A the cross-sectional area of the pore. The subscript of $(Pt)_{total}$ refers to the fact that Equation 9.2.1 is the product of two terms: $S(2\pi mkT)^{1/2}$ gives the exposure time required to coat a planar surface, while $[1 + (19/4)a + (3/2)a^2]$ is the factor by which exposure time must be increased to account for diffusion into the cylindrical pore.

Recently, Angel Yanguas-Gil and J. W. Elam published an analytical model of ALD in nanostructured substrates that applies to arbitrary geometries and reduces to the model proposed by Gordon et al in the case of cylindrical pores [173]. This model gives the critical time, t_c , to coat a feature of length L as

$$t_c = \frac{L^2}{D} \frac{1}{\gamma} \left(1 - \frac{\log(1-c)}{\alpha} \right) \quad (7.2)$$

where D is the precursor diffusivity in the given substrate, γ is the precursor excess number, α is the Damkoeler number, and c is the desired coverage fraction (0.9999 in the current work). The precursor excess number, γ , accounts for the ratio of available precursor molecules to available reaction sites, N_V / N_S , and is given explicitly as

$$\gamma = \frac{N_V}{N_S} = \frac{V}{S} n_0 s_0 \quad (7.3)$$

where V and S are the volume of open pores and surface area per unit spatial volume, n_0 is the precursor concentration at the substrate edge, and s_0 is the surface area

occupied by one adsorbed precursor molecule. The Damkoeler number, α , is the ratio of diffusion time to reaction time, and is given as

$$\alpha = \frac{t_{diff}}{t_{reac}} = \frac{1}{4} L^2 \bar{s} \frac{v_{th}}{D} \beta_0 \quad (7.4)$$

where \bar{s} is the surface area per unit volume, v_{th} is the root mean square thermal velocity of precursor molecules, and β_0 is the probability of adsorption when a precursor molecule encounters a suitable site.

7.3 Model development

In this work, the model developed by Yanguas-Gil and Elam [173] was applied to ALD Al_2O_3 in cellulose aerogels. ALD of Al_2O_3 using trimethylaluminum (TMA) and water is a well-studied system with a β_0 value of approximately 1, and thus β_0 was assumed to be exactly 1 in the current model. A critical assumption of the current work was that aerogel geometry – a chaotic network of tangled, loosely packed fibers – could be approximated by a three-dimensional cubic network of cylinders as shown in Figure 7.1. Assuming this simplified geometry allowed calculation of V and S using a cubic unit cell with vertices at the center of intersections between cylindrical fibers, as shown.

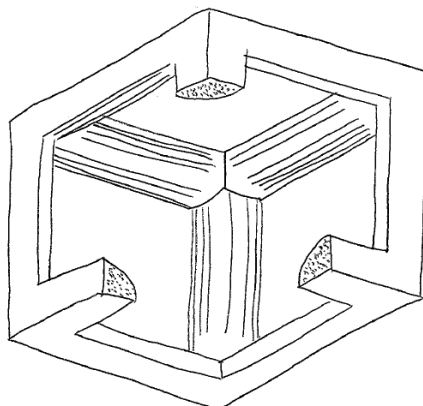


Figure 7.1: One unit cell for the open-pore cubic network of cylinders geometry applied to approximate aerogels. Near side is cut away to show interior. Drawn by Halley Farwood and used with permission.

Calculating V and S for the geometry shown in Figure 7.1 was done essentially by counting shapes. One fiber is represented as a cylinder, the three-dimensional solid representing the intersection of two cylinders is called a bicylinder, and that representing the intersection of three cylinders is called a tricylinder. 12 individual cylinders are each 1/4 represented in one unit cell. At all 8 corners of the unit cell, 3 unique intersections of two cylinders and 1 intersection of three cylinders occurs. This gives a total of 24 bicylinders and 8 tricylinders, each of which is only 1/8 represented in the unit cell. Finally, the geometry of one unit cell can be calculated by accounting for all cylinders, removing all bicylinders, and adding all tricylinders back in to correct for areas overlaps that had been accounted for multiple times. This process is given in Eqs. 7.5 and 7.6, which simplify to Eqs. 7.7 and 7.8.

$$V = V_{cell} - \left(\frac{12}{4} V_{cylinder} - 3 \frac{8}{8} V_{bicylinder} + \frac{8}{8} V_{tricylinder} \right) \quad (7.5)$$

$$S = \frac{12}{4} S_{cylinder} - 3 \frac{8}{8} S_{bicylinder} + \frac{8}{8} S_{tricylinder} \quad (7.6)$$

$$V = d^3 - 3\pi dr^2 + 16r^3 - 8(2 - \sqrt{2})r^3 \quad (7.7)$$

$$S = 6d\pi r - \sqrt{2}r^2 \quad (7.8)$$

In these equations, V_{cell} represents the total volume of space enclosed in one unit cell, r is average fiber radius including any deposition, and d represents the length of one edge of the cubic unit cell, taken as the average distance between aerogel fibers as observed by SEM, which varied per sample.

Precursor diffusion through this geometry was calculated using Knudsen diffusion theory, which is applicable in situations where the mean free path of gas particles is much less than the characteristic dimension of the system they are within. The ratio of mean free path to characteristic dimension is called the Knudsen number [174]. Calculating mean free path for a Boltzmann gas gives the equation for Knudsen number (Kn) given in Eq. 7.9,

$$Kn = \frac{kT}{\sqrt{2}\pi\sigma^2 pL} \quad (7.9)$$

where σ is the precursor molecular diameter (approximately 1 nm for TMA), p is total pressure, and L is the characteristic length of the system. Using a deposition temperature and pressure of 200 C and 1 mtorr along with an average fiber 50 nm for the characteristic size scale (as estimated from SEM imaging) gives a Knudsen number well above 1, meaning that Knudsen diffusion is a reasonable assumption.

Precursor diffusivity D was then calculated to first order in precursor density assuming Knudsen diffusion by applying Eq. 7.10,

$$D = \frac{3}{8n_0\sigma_{12}^2} \sqrt{\frac{kT}{2\pi} \left(\frac{1}{m_p} + \frac{1}{m_{gas}} \right)} \quad (7.10)$$

where n_0 is the number density of molecules obtained from the ideal gas law, σ_{12} is the average molecular radii of the precursor and its carrier gas (TMA and N₂, respectively), and m_p and m_{gas} are the molar masses of the precursor and carrier gas.

This equation for diffusivity was then divided by porosity to help account for the tortuosity of precursor diffusion in aerogels, which should increase with the thickness of the deposited film. The resulting expression for effective diffusivity D_{eff} is given in Eq. 7.11.

$$D_{eff} = D \frac{V}{d^3} \quad (7.11)$$

This diffusivity value was then incorporated into Eq. 7.2, the critical time to coat a feature as given by Yanguas-Gil and Elam. This critical time is intended as a lower bound for a single ALD pulse to coat a surface. The actual time required to transport precursor to a substrate will be more than this, and will vary depending on reactor design. For the current work, t_c was multiplied by a correction factor $F = 30$ to account for the transport time in the reactor used as well as variations in precursor and reactor pressure over time. Incorporating this correction factor and solving Equations 7.2 – 7.4 for L gave the expected penetration depth of a given ALD pulse as

$$L = F \sqrt{4D_{eff} \left(t\gamma + \frac{\log(1-c)}{\bar{v}_{th}\beta_0} \right)} \quad (7.12)$$

Planar silicon samples were used to determine average film growth per cycle (GPC), and the resulting thickness value was added to the radius of fibers less than L from the substrate surface after each simulated pulse. This equation was applied for each ALD pulse throughout a simulated deposition process, taking into account the modified geometry resulting from each pulse. Because fiber radius increases with each pulse, precursor diffusion becomes increasingly inhibited and the expected penetration depth L is reduced for each successive ALD cycle.

This modeling approach generates a thickness profile in a nanostructured substrate with three distinct regions. Near the substrate surface, film thickness is constant and defined primarily by the number of cycles multiplied by the expected GPC. This region is called the cycle-limited region, and extends from the substrate surface to L_{min} , the penetration depth of the final ALD cycle. From L_{min} to L_{max} , the penetration depth of the first ALD cycle, is a region in which film thickness continually decreases with increasing distance from the substrate surface. This is called the diffusion-limited region: because fiber radiuses effectively increase throughout deposition, fewer ALD cycles are able to penetrate into deeper regions, and these regions thus have a thinner coating. Beyond L_{max} is a third region with approximately zero coating thickness, as little if any precursor material is expected to penetrate to this depth.

7.4 Experimental application to ALD in CNC aerogels

The accuracy of the currently developed model was tested by depositing Al_2O_3 onto and within CNC aerogels prepared according to published methods [174, 175],

detailed explicitly in [167]. Morphological features of CNC aerogels were obtained using Brunauer-Emmett-Teller (BET) gas adsorption/desorption measurements performed by Christian Buesch with the OSU Forestry Department. Varying ALD parameters, given in Table 7.1, were used to test the model under different circumstances. Resulting film thickness profiles were then characterized by transmission electron microscopy (TEM), scanning electron microscopy (SEM), and electron probe microanalysis (EPMA).

Table 7.1: ALD parameters for Al₂O₃ deposition in CNC aerogels

ALD cycles	Pulse time (s)	Exposure and purge time (s)	Temperature (°C)
272	0.02	30	150
272	0.18	600	150
272	1.00	600	80

7.5 Results

Modification of aerogels by 50 cycles or more of ALD Al₂O₃ was clearly visible by eye, and conformal coating of individual aerogel fibers was clearly established with TEM imaging. Figure 7.2 displays these images.

The three thickness regimes predicted by the developed model are characterized respectively by a region of constant, depth-independent film thickness; diminishing film thickness with depth; and zero film thickness past a certain maximum depth. These three regimes were observed with EPMA elemental analysis observations of aluminum content, shown in Figure 7.3, and SEM imaging of fiber radiuses, shown in

Figure 7.4.

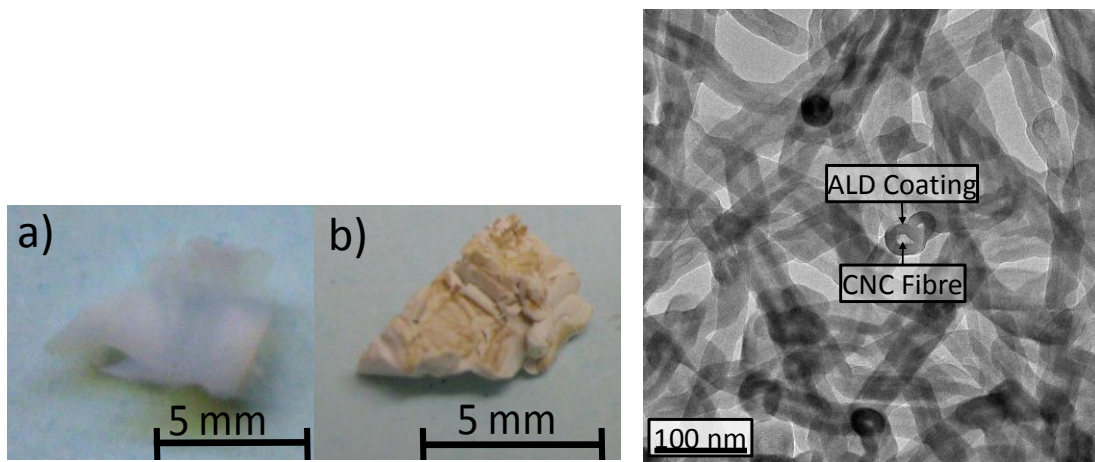


Figure 7.2: ALD coatings on CNC aerogels, reproduced from [177]

- a) Photograph of uncoated CNC aerogel.
- b) Photograph of CNC aerogel coated with ALD Al₂O₃.
- c) Cross-sectional TEM image of CNC aerogel coated with ALD Al₂O₃ using 50 cycles, 500 ms pulses, and 120 s exposures and purges. Image taken near aerogel surface.

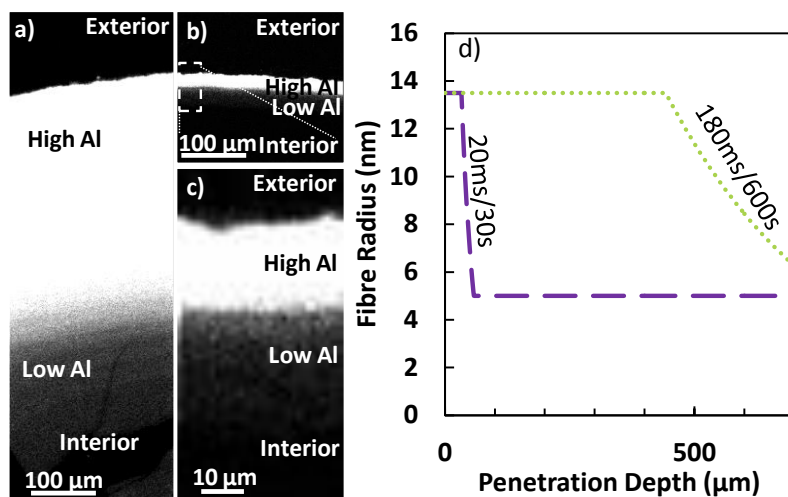


Figure 7.3: Comparison of experimental and modeled ALD Al₂O₃ thickness profiles. Cycle-limited, diffusion-limited, and uncoated regions are apparent in both experimentally observed and modeled profiles. Reproduced from [177].

a, b, and c) Cross-sectional EPMA images of CNC aerogel coated with 50 cycles of ALD Al₂O₃ at 150 °C using (a) 180 ms pulses and 600 s exposures and purges or (b, c) 20ms pulses and 30s purges.

d) Modeled thickness profiles for displayed pulse/(exposure and purge) times, showing similar thickness profiles to those observed experimentally.

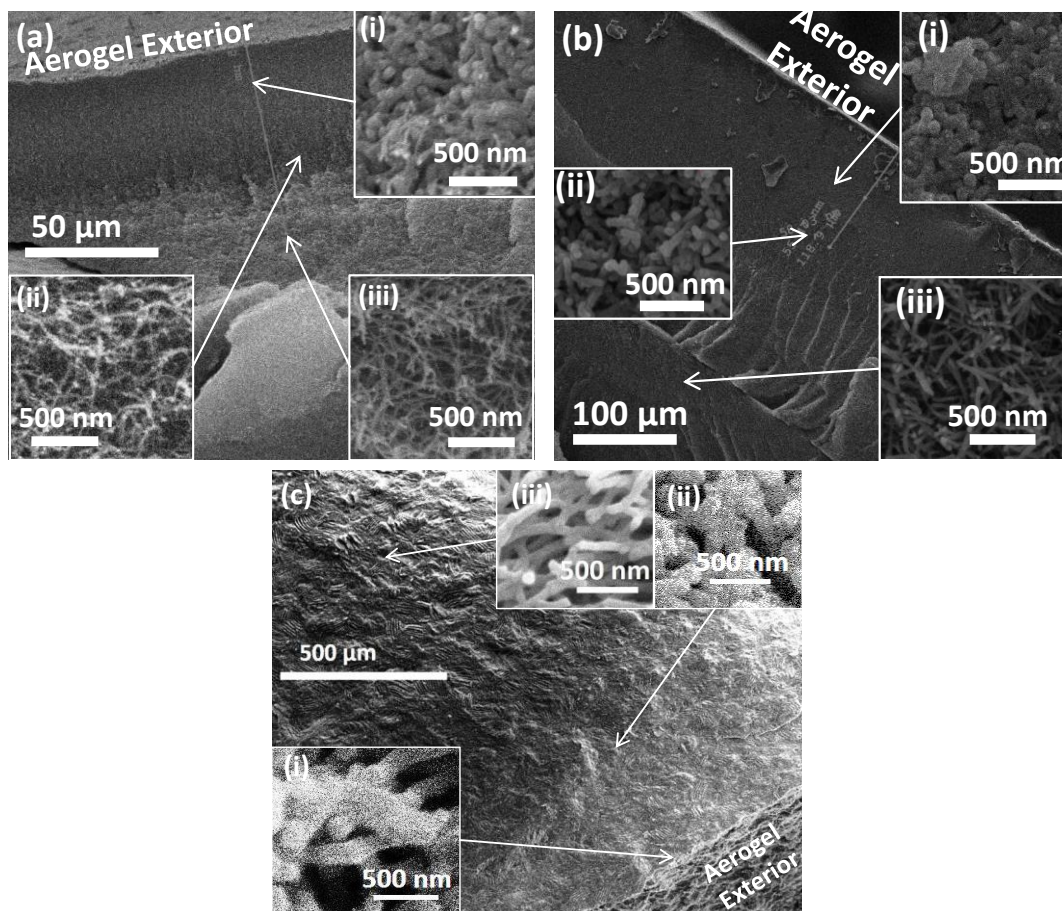


Figure 7.4: SEM of fractured CNC aerogels coated with 272 cycles of ALD Al_2O_3 using different deposition parameters. Insets show morphology in each of the three thickness regimes observed. Deposition parameters and depths from the aerogel surface for inset images are as follows:

a) 20 ms pulses and 30 s exposures and purges, at 150 °C.

Insets: (i) 10 μm , (ii) 45 μm , and (iii) 70 μm .

b) 180 ms pulses and 600 s exposures and purges, at 150 °C.

Insets: (i) 50 μm , (ii) 120 μm , and (iii) 300 μm .

c) 1000 ms pulses and 600 s exposures and purges, at 80 °C. Substrate showed a more open morphology than (a) or (b). Insets: (i) 10 μm , (ii) 390 μm , and (iii) 1220 μm

Reproduced from [177].

Figures 7.3 and 7.4, in addition to the presence of the three predicted thickness regimes, demonstrate the effectiveness of extended pulse and exposure times in order

to increase ALD penetration depth. The difference between 1000 ms pulse / 600 s exposure and purge and 180 ms pulse / 600 s exposure and purge indicates that increasing pulse time, and thereby introducing more precursor material, can effectively increase penetration depth.

Finally, to test the accuracy of the model, fiber radiuses at different depths within coated aerogel samples were measured in SEM images and plotted against depth from the aerogel surface. These measurements were compared to modeled thickness profiles, as displayed in Figure 7.5.

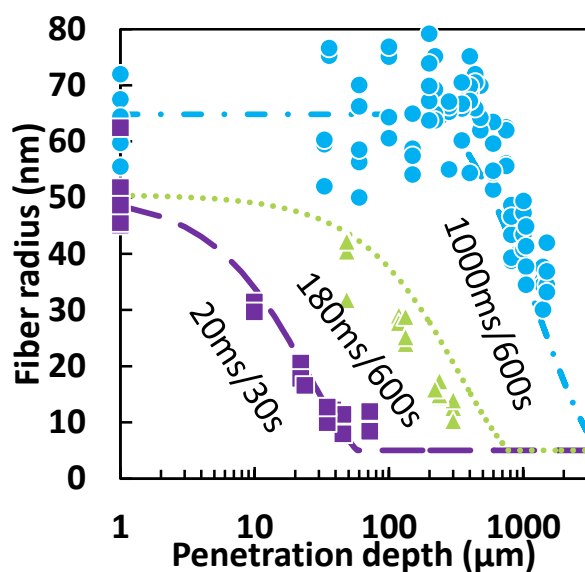


Figure 7.5: Fiber radius as a function of depth from the aerogel surface for ALD Al_2O_3 using the displayed pulse / (exposure and purge) times. Minimum thickness values represent uncoated fibers, and increasing thickness is due to ALD Al_2O_3 coating. Lines represent modeled thickness parameters, and points represent thicknesses measured with SEM imaging. Reproduced from [177].

Figure 7.5 appears to show a good fit between modeled and experimentally observed thickness profiles. All cases examined show the presence of three thickness regimes – cycle-limited, diffusion-limited, and uncoated – in both modeled and

observed thickness profiles. Modeled profiles transition between thickness regimes in much the same way as observed profiles, though a slight mismatch in absolute thickness values is observed in the case of 180 ms pulses and 600 s exposures and purges. The most likely reason identified for this mismatch is a difference in aerogel composition, possibly average fiber radius, between this sample and others, though this was not verified. It is also possible that the modeling fit parameter F may have some dependency on the ratio of pulse to exposure and purge time.

True aerogel structures are significantly more complex than the modeled geometry, but the close correspondence between predicted and experimentally observed thickness profiles suggests that a three-dimensional cubic network of cylinders may function as an appropriate analogue for aerogels in computational models of ALD in porous substrates.

7.6 Conclusion and future work

The work presented in this chapter demonstrates that representing an aerogel as a cubic network of cylinders allows the analytical model of ALD in nanostructured substrates developed by Yanguas-Gil and Elam [173] to predict ALD thickness profiles with encouraging accuracy. This conclusion opens doors for a number of research thrusts to expand the current work.

The current model assumes a value of 1 for β_0 , the reaction probability when a precursor molecule encounters an available surface site. This is a reasonable assumption for the TMA-H₂O ALD process, but applying the current model to other ALD processes with values of $\beta_0 < 1$ would help confirm its completeness. Also,

Yanguas-Gil and Elam provide a modification to the cited model to account for the effects of non-coating precursor decomposition during an ALD cycle. Testing systems known to involve significant precursor decomposition against this model would represent a useful investigation of the completeness of their work.

The demonstrated applicability of the current model to a structure as morphologically complex as aerogels should encourage exploration of other geometries. Possible materials of interest may include nanoparticle composites, potentially modeled as close-packed spheres with an appropriate size distribution (typically lognormal [176–178]); powders, modeled as loosely-packed solids according to the expected fracture mode of the powdered material; nanowire arrays, as grown or after sonication and annealing; or more well-defined geometries such as micromachined pores or microchannels of the sort applied in chemical and biological engineering.

Future research related specifically to the current work should aim to resolve the correction factor F into physically meaningful components, possibly including tool-dependent precursor transport time, exponential decay of precursor partial pressure throughout an extended pulse, and variation in chamber pressure throughout exposure steps. Also, the observed mismatch between predicted and observed thickness profiles in the case of one set of ALD parameters should be investigated to determine whether fault lies with incorrect given values (such as aerogel fiber thickness) or inaccuracy within the model itself. Additional ALD depositions under different parameters using the current model will likely be necessary for both of these purposes, as well as more

thoroughly exploring the model in general. Further, accuracy for the aerogel model may be improved by taking into account the expected distribution of fiber radiuses instead of only the approximate average value.

Bibliography

- [1] “A Full-Color Screen That Bends | MIT Technology Review.” [Online]. Available: <http://www.technologyreview.com/news/413732/a-full-color-screen-that-bends/>. [Accessed: 21-Oct-2013].
- [2] “Thin Displays as Wristbands | MIT Technology Review.” [Online]. Available: <http://www.technologyreview.com/news/421222/thin-displays-as-wristbands/>. [Accessed: 21-Oct-2013].
- [3] C. for D. and R. Health, “Artificial Pancreas Device System (APDS) - Types of Artificial Pancreas Device Systems.” [Online]. Available: <http://www.fda.gov/MedicalDevices/ProductsandMedicalProcedures/HomeHealthandConsumer/ConsumerProducts/ArtificialPancreas/ucm259555.htm>. [Accessed: 11-Nov-2013].
- [4] D. G. Gardner, D. M. Shoback, and F. S. Greenspan, *Greenspan's basic & clinical endocrinology*. New York; Toronto: McGraw-Hill Medical, 2011.
- [5] “CDC - 2011 National Diabetes Fact Sheet - Publications - Diabetes DDT.” [Online]. Available: <http://www.cdc.gov/diabetes/pubs/factsheet11.htm?loc=diabetes-statistics>. [Accessed: 07-Nov-2013].
- [6] “FASTSTATS - Leading Causes of Death.” [Online]. Available: <http://www.cdc.gov/nchs/fastats/lcod.htm>. [Accessed: 07-Nov-2013].
- [7] “Type 2 diabetes - MayoClinic.com.” [Online]. Available: <http://www.mayoclinic.com/health/type-2-diabetes/DS00585>. [Accessed: 10-Dec-2013].
- [8] “Champ Lyons: An Incomplete Life.” [Online]. Available: <http://www.ncbi.nlm.nih.gov/pmc/articles/PMC1514522/>. [Accessed: 28-Oct-2013].
- [9] L. C. Clark and C. Lyons, “ELECTRODE SYSTEMS FOR CONTINUOUS MONITORING IN CARDIOVASCULAR SURGERY,” *Ann. N. Y. Acad. Sci.*, vol. 102, no. 1, pp. 29–45, 1962.
- [10] “REFLECTANCE METER BACKGROUND OF PRIOR ART,” 3,604,815Sep-1971.
- [11] N. S. Oliver, C. Toumazou, A. E. G. Cass, and D. G. Johnston, “Glucose sensors: a review of current and emerging technology,” *Diabet. Med. J. Br. Diabet. Assoc.*, vol. 26, no. 3, pp. 197–210, Mar. 2009.
- [12] P. H. Sönksen, S. L. Judd, and C. Lowy, “HOME MONITORING OF BLOOD-GLUCOSE,” *The Lancet*, vol. 311, no. 8067, pp. 729–732, Apr. 1978.
- [13] S. Walford, E. A. M. Gale, S. P. Allison, and R. B. Tattersall, “SELF-MONITORING OF BLOOD-GLUCOSE,” *The Lancet*, vol. 311, no. 8067, pp. 732–735, Apr. 1978.
- [14] T. S. Danowski and J. H. Sunder, “Jet injection of insulin during self-monitoring of blood glucose,” *Diabetes Care*, vol. 1, no. 1, pp. 27–33, Feb. 1978.

- [15] Y. Ikeda, N. Tajima, N. Minami, Y. Ide, J. Yokoyama, and M. Abe, "Pilot study of self-measurement of blood glucose using the dextrostix-eyetone system for juvenile-onset diabetes," *Diabetologia*, vol. 15, no. 2, pp. 91–93, Aug. 1978.
- [16] J. S. Skyler, I. A. Lasky, D. L. Skyler, E. G. Robertson, and D. H. Mintz, "Home blood glucose monitoring as an aid in diabetes management," *Diabetes Care*, vol. 1, no. 3, pp. 150–157, Jun. 1978.
- [17] "Consensus statement on self-monitoring of blood glucose," *Diabetes Care*, vol. 10, no. 1, pp. 95–99, Feb. 1987.
- [18] L. M. C. Welschen, E. Bloemendal, G. Nijpels, J. M. Dekker, R. J. Heine, W. A. B. Stalman, and L. M. Bouter, "Self-monitoring of blood glucose in patients with type 2 diabetes who are not using insulin: a systematic review," *Diabetes Care*, vol. 28, no. 6, pp. 1510–1517, Jun. 2005.
- [19] W. A. Davis, D. G. Bruce, and T. M. E. Davis, "Does self-monitoring of blood glucose improve outcome in type 2 diabetes? The Fremantle Diabetes Study," *Diabetologia*, vol. 50, no. 3, pp. 510–515, Jan. 2007.
- [20] W. A. Davis, D. G. Bruce, and T. M. E. Davis, "Is Self-Monitoring of Blood Glucose Appropriate for All Type 2 Diabetic Patients? The Fremantle Diabetes Study: Response to Kolb et al.," *Diabetes Care*, vol. 30, no. 1, pp. 184–185, Jan. 2007.
- [21] A. Tengblad, E. Grodzinsky, K. Lindström, S. Mölsted, L. Borgquist, and C. Johan Östgren, "Self-monitoring of blood glucose and glycaemic control in type 2 diabetes," *Scand. J. Prim. Health Care*, vol. 25, no. 3, pp. 140–146, Jan. 2007.
- [22] R. C. of P. of L. National Collaborating Centre for Chronic Conditions (Great Britain), *Type 2 diabetes: national clinical guideline for management in primary and secondary care (update)*. London: Royal College of Physicians, 2008.
- [23] D. D. Cunningham, J. A. Stenken, and Wiley InterScience (Online service), *In vivo glucose sensing*. Hoboken, N.J.: Wiley, 2010.
- [24] "The Effect of Intensive Treatment of Diabetes on the Development and Progression of Long-Term Complications in Insulin-Dependent Diabetes Mellitus," *N. Engl. J. Med.*, vol. 329, no. 14, pp. 977–986, 1993.
- [25] D. Keilin and E. F. Hartree, "The use of glucose oxidase (notatin) for the determination of glucose in biological material and for the study of glucose-producing systems by manometric methods," *Biochem. J.*, vol. 42, no. 2, p. 230, 1948.
- [26] J. Raba and H. A. Mottola, "Glucose Oxidase as an Analytical Reagent," *Crit. Rev. Anal. Chem.*, vol. 25, no. 1, pp. 1–42, Sep. 1995.
- [27] "Electrochemical Reactions." [Online]. Available: <http://chemed.chem.purdue.edu/genchem/topicreview/bp/ch20/electro.php>. [Accessed: 29-Oct-2013].
- [28] R. H. Petrucci, *General chemistry: principles and modern applications*, 9th ed. Upper Saddle River, N.J: Pearson/Prentice Hall, 2007.
- [29] D. KEILIN and E. F. HARTREE, "Specificity of glucose oxidase (notatin)," *Biochem. J.*, vol. 50, no. 3, pp. 331–341, Jan. 1952.

- [30] D. Moatti-Sirat, V. Poitout, V. Thomé, M. N. Gangnerau, Y. Zhang, Y. Hu, G. S. Wilson, F. Lemonnier, J. C. Klein, and G. Reach, "Reduction of acetaminophen interference in glucose sensors by a composite Nafion membrane: demonstration in rats and man," *Diabetologia*, vol. 37, no. 6, pp. 610–616, Jun. 1994.
- [31] L. J. Sammartano, R. W. Tuveson, and R. Davenport, "Control of sensitivity to inactivation by H₂O₂ and broad-spectrum near-UV radiation by the *Escherichia coli* katF locus," *J. Bacteriol.*, vol. 168, no. 1, pp. 13–21, 1986.
- [32] M. D. Gouda, "Thermal Inactivation of Glucose Oxidase: MECHANISM AND STABILIZATION USING ADDITIVES," *J. Biol. Chem.*, vol. 278, no. 27, pp. 24324–24333, May 2003.
- [33] P. F. Greenfield, J. R. Kittrell, and R. L. Laurence, "Inactivation of immobilized glucose oxidase by hydrogen peroxide," *Anal. Biochem.*, vol. 65, no. 1–2, pp. 109–124, May 1975.
- [34] A. V. Rao, P. D. Sima, J. R. Kanofsky, and T. Ramasarma, "Inactivation of glucose oxidase by diperoxovanadate-derived oxidants," *Arch. Biochem. Biophys.*, vol. 369, no. 1, pp. 163–173, Sep. 1999.
- [35] E. I. Karaseva, E. I. Tarun, and D. I. Metelitsa, "An ultrasonic inactivation of *Aspergillus niger* glucose oxidase in aqueous solutions," *Appl. Biochem. Microbiol.*, vol. 45, no. 1, pp. 9–16, Jan. 2009.
- [36] "Hyperglycemia in diabetes: Tests and diagnosis - MayoClinic.com." [Online]. Available: <http://www.mayoclinic.com/health/hyperglycemia/DS01168/DSECTION=tests-and-diagnosis>. [Accessed: 20-Nov-2013].
- [37] G. Piechotta, J. Albers, and R. Hintsche, "Novel micromachined silicon sensor for continuous glucose monitoring," *Biosens. Bioelectron.*, vol. 21, no. 5, pp. 802–808, Nov. 2005.
- [38] M. Metzger, G. Leibowitz, J. Wainstein, B. Glaser, and I. Raz, "Reproducibility of Glucose Measurements Using the Glucose Sensor," *Diabetes Care*, vol. 25, no. 7, pp. 1185–1191, Jul. 2002.
- [39] H. R. Murphy, G. Rayman, K. Lewis, S. Kelly, B. Johal, K. Duffield, D. Fowler, P. J. Campbell, and R. C. Temple, "Effectiveness of continuous glucose monitoring in pregnant women with diabetes: randomised clinical trial," *BMJ*, vol. 337, no. sep25 2, pp. a1680–a1680, Sep. 2008.
- [40] G. J. Janz and D. J. G. Ives, "Silver, Silver Chloride Electrodes," *Ann. N. Y. Acad. Sci.*, vol. 148, no. 1, pp. 210–221, 1968.
- [41] D. T. Lykken and P. H. Venables, "Direct Measurement of Skin Conductance: A Proposal for Standardization," *Psychophysiology*, vol. 8, no. 5, pp. 656–672, 1971.
- [42] W. M. Haynes, D. R. Lide, and Bruno, *CRC handbook of chemistry and physics: a ready-reference book of chemical and physical data*. Boca Raton, Fla.; London: CRC, 2012.
- [43] A. W. J. Cranny and J. K. Atkinson, "Thick film silver-silver chloride reference electrodes," *Meas. Sci. Technol.*, vol. 9, no. 9, p. 1557, 1998.

- [44] “Chloride test - blood: MedlinePlus Medical Encyclopedia.” [Online]. Available: <http://www.nlm.nih.gov/medlineplus/ency/article/003485.htm>. [Accessed: 20-Nov-2013].
- [45] W. S. Wong and A. Salleo, *Flexible electronics: materials and applications*, vol. 11. Springer, 2009.
- [46] F. A. Shirland, “The history, design, fabrication and performance of CdS thin film solar cells,” *Adv. Energy Convers.*, vol. 6, no. 4, pp. 201–221, Oct. 1966.
- [47] R. L. Crabb and F. C. Treble, “Thin Silicon Solar Cells for Large Flexible Arrays,” *Nature*, vol. 213, no. 5082, pp. 1223–1224, Mar. 1967.
- [48] K. A. Ray, “Flexible Solar Cell Arrays for Increased Space Power,” *IEEE Trans. Aerosp. Electron. Syst.*, vol. AES-3, no. 1, pp. 107–115, Jan. 1967.
- [49] T. P. Brody, “The thin film transistor—A late flowering bloom,” *IEEE Trans. Electron Devices*, vol. 31, no. 11, pp. 1614–1628, Nov. 1984.
- [50] T. P. Brody, “The birth and early childhood of active matrix — A personal memoir,” *J. Soc. Inf. Disp. - J SOC INF DISP*, vol. 4, no. 3, 1996.
- [51] Y. Hamakawa, “Recent advances in amorphous silicon solar cells,” *Sol. Energy Mater.*, vol. 8, no. 1–3, pp. 101–121, Nov. 1982.
- [52] P. E. Glaser, “Solar power from satellites,” *Phys. Today*, vol. 30, no. 2, p. 30, 1977.
- [53] T. Moriizumi, “Merocyanine-dye photovoltaic cell on a plastic film,” *Appl. Phys. Lett.*, vol. 38, no. 2, p. 85, 1981.
- [54] P. Nath and M. Izu, “Performance of large area amorphous Si based single and multiple junction solar cells,” in *IN: Photovoltaic Specialists Conference, 18th, Las Vegas, NV, October 21-25, 1985, Conference Record (A87-19826 07-44). New York, Institute of Electrical and Electronics Engineers, Inc., 1985, p. 939-942.*, 1985, vol. -1, pp. 939–942.
- [55] M. Yano, K. Suzuki, K. Nakatani, and H. Okaniwa, “Roll-to-roll preparation of a hydrogenated amorphous silicon solar cell on a polymer film substrate,” *Thin Solid Films*, vol. 146, no. 1, pp. 75–81, Jan. 1987.
- [56] S. D. Theiss and S. Wagner, “Amorphous silicon thin-film transistors on steel foil substrates,” *IEEE Electron Device Lett.*, vol. 17, no. 12, pp. 578–580, Dec. 1996.
- [57] N. D. Young, G. Harkin, R. M. Bunn, D. J. McCulloch, R. W. Wilks, and A. G. Knapp, “Novel fingerprint scanning arrays using polysilicon TFT’s on glass and polymer substrates,” *IEEE Electron Device Lett.*, vol. 18, no. 1, pp. 19–20, Jan. 1997.
- [58] P. M. Smith, P. G. Carey, and T. W. Sigmon, “Excimer laser crystallization and doping of silicon films on plastic substrates,” *Appl. Phys. Lett.*, vol. 70, no. 3, p. 342, 1997.
- [59] “LG Display expected to provide OLEDs for iWatch.” [Online]. Available: <http://www.koreaherald.com/view.php?ud=20131029000985>. [Accessed: 30-Oct-2013].
- [60] “LG announces ‘self-healing’ G Flex, calls it first ‘real’ curved smartphone,” *The Verge*. [Online]. Available:

- <http://www.theverge.com/2013/10/27/5036288/lg-g-flex-officially-announced>. [Accessed: 30-Oct-2013].
- [61] “Samsung Highlights Innovations in Mobile Experiences Driven by Components, in CES Keynote.” [Online]. Available: <http://www.samsung.com/global/business/semiconductor/news-events/press-releases/detail?newsId=12521>. [Accessed: 30-Oct-2013].
- [62] M. S. posted S. 5th and 2013 at 7:39 AM 65, “Samsung announces the world’s first curved UHD TVs at IFA 2013,” *Engadget*. [Online]. Available: <http://www.engadget.com/2013/09/05/samsung-reveals-the-world-s-first-curved-uhd-tvs-at-ifa-2013/>. [Accessed: 30-Oct-2013].
- [63] C. Denison, “LG’s insane 77-inch Ultra HD curved OLED leaves no box unchecked,” *Digital Trends*. [Online]. Available: <http://www.digitaltrends.com/home-theater/lg-unveils-a-eyeful-of-tv-awesome-with-77-inch-curved-ultra-hd-oled-television/>. [Accessed: 30-Oct-2013].
- [64] J. W. Hutchinson and Z. Suo, “Mixed Mode Cracking in Layered Materials,” in *Advances in Applied Mechanics*, vol. Volume 29, John W. Hutchinson and Theodore Y. Wu, Ed. Elsevier, 1991, pp. 63–191.
- [65] O. Knotek, R. Elsing, G. Krämer, and F. Jungblut, “On the origin of compressive stress in PVD coatings — an explicative model,” *Surf. Coat. Technol.*, vol. 46, no. 3, pp. 265–274, Sep. 1991.
- [66] M. Ghosh, *Polyimides: Fundamentals and Applications*. CRC Press, 1996.
- [67] O. B. Soroka, “Evaluation of residual stresses in PVD-coatings. Part 1. Review,” *Strength Mater.*, vol. 42, no. 3, pp. 287–296, May 2010.
- [68] *Adhesion promotion techniques: technological applications*. New York: M. Dekker, 1999.
- [69] S. Kawahara, Y. Kano, and S. Akiyama, “Estimation of Critical Surface Tension and Interfacial Interaction of Poly(vinyl ethylene-co-1,4-butadiene)/Terpene Resin Blends by Contact Angle,” *Polym. J.*, vol. 24, no. 2, pp. 145–155, Feb. 1992.
- [70] H. . Fox and W. . Zisman, “The spreading of liquids on low energy surfaces. I. polytetrafluoroethylene,” *J. Colloid Sci.*, vol. 5, no. 6, pp. 514–531, Dec. 1950.
- [71] H. . Fox and W. . Zisman, “The spreading of liquids on low-energy surfaces. II. Modified tetrafluoroethylene polymers,” *J. Colloid Sci.*, vol. 7, no. 2, pp. 109–121, Apr. 1952.
- [72] H. . Fox and W. . Zisman, “The spreading of liquids on low-energy surfaces. III. Hydrocarbon surfaces,” *J. Colloid Sci.*, vol. 7, no. 4, pp. 428–442, Aug. 1952.
- [73] W. A. Zisman, *Contact angle, wettability and adhesion: the Kendall award symposium honoring William A. Zisman, Los Angeles, Calif., April 2-3, 1963*. American Chemical Society, 1964.
- [74] H. Schonhorn and L. H. Sharpe, “Surface energetics, adhesion, and adhesive joints. IV. Joints between epoxy adhesives and chlorotrifluoroethylene copolymer and terpolymer (aclar),” *J. Polym. Sci. A*, vol. 3, no. 9, pp. 3087–3097, 1965.
- [75] A. H. Firester and M. G. Kane, “Macroelectronics: a progress report,” in *Defense and Security*, 2005, pp. 24–30.

- [76] B. Mimoun, V. Henneken, P. M. Sarro, and R. Dekker, "Ultra-flexible devices for 360 μm diameter guidewires," in *Micro Electro Mechanical Systems (MEMS), 2012 IEEE 25th International Conference on*, 2012, pp. 472–475.
- [77] Flexible Circuit Technologies (FCT), "Flexible Design Guide." .
- [78] "Lenthor Engineering - Flexible Circuit Design Guide." [Online]. Available: <http://www.lenthor.com/design-guide/>. [Accessed: 25-Nov-2013].
- [79] Teledyne Electronic Technologies, Printed Circuit Technology Business Unit, "designguide.pdf." .
- [80] All Flex Flexible Circuits, "dg2012_web.pdf." .
- [81] C. Li, C. H. Ahn, L. A. Shutter, and R. K. Narayan, "Toward real-time continuous brain glucose and oxygen monitoring with a smart catheter," *Biosens. Bioelectron.*, vol. 25, no. 1, pp. 173–178, Sep. 2009.
- [82] Y.-L. Loo, T. Someya, K. W. Baldwin, Z. Bao, P. Ho, A. Dodabalapur, H. E. Katz, and J. A. Rogers, "Soft, conformable electrical contacts for organic semiconductors: High-resolution plastic circuits by lamination," *Proc. Natl. Acad. Sci.*, vol. 99, no. 16, pp. 10252–10256, 2002.
- [83] D. Thompson, O. Tantot, H. Jallageas, G. E. Ponchak, M. M. Tentzeris, and J. Papapolymerou, "Characterization of liquid crystal polymer (LCP) material and transmission lines on LCP substrates from 30 to 110 GHz," *IEEE Trans. Microw. Theory Tech.*, vol. 52, no. 4, pp. 1343–1352, 2004.
- [84] K. Jain, M. Klosner, M. Zemel, and S. Raghunandan, "Flexible Electronics and Displays: High-Resolution, Roll-to-Roll, Projection Lithography and Photoablation Processing Technologies for High-Throughput Production," *Proc. IEEE*, vol. 93, no. 8, pp. 1500–1510, 2005.
- [85] I.-C. Cheng and S. Wagner, "Overview of Flexible Electronics Technology," in *Flexible Electronics*, W. S. Wong and A. Salleo, Eds. Springer US, 2009, pp. 1–28.
- [86] H. Kavak, C. Gruber, H. Shanks, A. Landin, A. Constant, and S. Burns, "Thin film transistors on polyimide substrates," *J. Non-Cryst. Solids*, vol. 266–269, Part 2, pp. 1325–1328, May 2000.
- [87] Y. Kuo, *Proceedings of the Second Symposium on Thin Film Transistor Technologies*. The Electrochemical Society, 1995.
- [88] Y. Kuo, "Thin Film Transistors with Graded SiN x Gate Dielectrics," *J. Electrochem. Soc.*, vol. 141, no. 4, pp. 1061–1065, Apr. 1994.
- [89] P. C. P. Cheung, A. A. Berlin, D. K. Biegelsen, R. K.-H. Lau, and M. H. Yim, "Thin film structure machining and attachment," 621051403-Apr-2001.
- [90] K. M. Vaeth, D. DeMejo, E. Dokyi, M. Evans, J. Jech, M. Lehmann, R. Link, and J. Sechrist, "MEMS-Based Inkjet Drop Generators from Plastic Substrates," 2007. [Online]. Available: <http://orst.library.ingentaconnect.com/content/ist/nipdf/2007/00002007/00000001/art00070>. [Accessed: 06-Nov-2013].
- [91] K. M. Vaeth, "Continuous Inkjet Drop Generators Fabricated From Plastic Substrates," *J. Microelectromechanical Syst.*, vol. 16, no. 5, pp. 1080–1086, 2007.

- [92] B. Murari, B. Vigna, S. Sassolini, F. Ratti, and A. Alessandri, "Process for manufacturing a group comprising at least two elements, one ...," 663883628-Oct-2003.
- [93] M. C. Cortizo and M. F. L. de Mele, "Cytotoxicity of copper ions released from metal," *Biol. Trace Elem. Res.*, vol. 102, no. 1–3, pp. 129–141, Dec. 2004.
- [94] G. G. Wallace, T. E. Campbell, and P. C. Innis, "Putting function into fashion: Organic conducting polymer fibres and textiles," *Fibers Polym.*, vol. 8, no. 2, pp. 135–142, 2007.
- [95] B.-J. de Gans, P. C. Duineveld, and U. S. Schubert, "Inkjet printing of polymers: state of the art and future developments," *Adv. Mater.*, vol. 16, no. 3, pp. 203–213, 2004.
- [96] G. Eda, G. Fanchini, and M. Chhowalla, "Large-area ultrathin films of reduced graphene oxide as a transparent and flexible electronic material," *Nat. Nanotechnol.*, vol. 3, no. 5, pp. 270–274, May 2008.
- [97] S. Bae, H. Kim, Y. Lee, X. Xu, J.-S. Park, Y. Zheng, J. Balakrishnan, T. Lei, H. Ri Kim, Y. I. Song, Y.-J. Kim, K. S. Kim, B. Özyilmaz, J.-H. Ahn, B. H. Hong, and S. Iijima, "Roll-to-roll production of 30-inch graphene films for transparent electrodes," *Nat. Nanotechnol.*, vol. 5, no. 8, pp. 574–578, Aug. 2010.
- [98] S. Bertolazzi, J. Brivio, and A. Kis, "Stretching and Breaking of Ultrathin MoS₂," *ACS Nano*, vol. 5, no. 12, pp. 9703–9709, Dec. 2011.
- [99] Q. H. Wang, K. Kalantar-Zadeh, A. Kis, J. N. Coleman, and M. S. Strano, "Electronics and optoelectronics of two-dimensional transition metal dichalcogenides," *Nat. Nanotechnol.*, vol. 7, no. 11, pp. 699–712, Nov. 2012.
- [100] H. Wang, L. Yu, Y.-H. Lee, Y. Shi, A. Hsu, M. L. Chin, L.-J. Li, M. Dubey, J. Kong, and T. Palacios, "Integrated Circuits Based on Bilayer MoS₂ Transistors," *Nano Lett.*, vol. 12, no. 9, pp. 4674–4680, Sep. 2012.
- [101] S. Metz, A. Bertsch, D. Bertrand, and P. Renaud, "Flexible polyimide probes with microelectrodes and embedded microfluidic channels for simultaneous drug delivery and multi-channel monitoring of bioelectric activity," *Biosens. Bioelectron.*, vol. 19, no. 10, pp. 1309–1318, May 2004.
- [102] F. Schmitz and M. Nienhaus, "Use of polyimide for adhesive layers, lithographic method for producing ...," 674681908-Jun-2004.
- [103] C. Kergueris, J.-P. Bourgoin, S. Palacin, D. Esteve, C. Urbina, M. Magoga, and C. Joachim, "Electron transport through a metal-molecule-metal junction," *Phys. Rev. B*, vol. 59, no. 19, pp. 12505–12513, May 1999.
- [104] S. Metz, R. Holzer, and P. Renaud, "Polyimide-based microfluidic devices," *Lab. Chip*, vol. 1, no. 1, p. 29, 2001.
- [105] S. H. Kim, S. H. Cho, N.-E. Lee, H. M. Kim, Y. W. Nam, and Y.-H. Kim, "Adhesion properties of Cu/Cr films on polyimide substrate treated by dielectric barrier discharge plasma," *Surf. Coat. Technol.*, vol. 193, no. 1–3, pp. 101–106, Apr. 2005.
- [106] T. O. Kääriäinen, P. Maydannik, D. C. Cameron, K. Lahtinen, P. Johansson, and J. Kuusipalo, "Atomic layer deposition on polymer based flexible packaging

- materials: Growth characteristics and diffusion barrier properties,” *Thin Solid Films*, vol. 519, no. 10, pp. 3146–3154, Mar. 2011.
- [107] H. F. Hildebrand, C. Veron, and P. Martin, “Nickel, chromium, cobalt dental alloys and allergic reactions: an overview,” *Biomaterials*, vol. 10, no. 8, pp. 545–548, Oct. 1989.
- [108] G. M. Keegan, I. D. Learmonth, and C. Case, “A Systematic Comparison of the Actual, Potential, and Theoretical Health Effects of Cobalt and Chromium Exposures from Industry and Surgical Implants,” 20-Oct-2008. [Online]. Available: <http://informahealthcare.com/doi/abs/10.1080/10408440701845534>. [Accessed: 20-Nov-2013].
- [109] S. J. Yun, Y.-W. Ko, and J.-W. Lim, “Passivation of organic light-emitting diodes with aluminum oxide thin films grown by plasma-enhanced atomic layer deposition,” *Appl. Phys. Lett.*, vol. 85, no. 21, pp. 4896–4898, 2004.
- [110] M. D. Groner, S. M. George, R. S. McLean, and P. F. Carcia, “Gas diffusion barriers on polymers using Al₂O₃ atomic layer deposition,” *Appl. Phys. Lett.*, vol. 88, no. 5, p. 051907, 2006.
- [111] P. F. Carcia, R. S. McLean, M. D. Groner, A. A. Dameron, and S. M. George, “Gas diffusion ultrabarrriers on polymer substrates using Al₂O₃ atomic layer deposition and SiN plasma-enhanced chemical vapor deposition,” *J. Appl. Phys.*, vol. 106, no. 2, p. 023533, 2009.
- [112] R. Cooper, H. P. Upadhyaya, T. K. Minton, M. R. Berman, X. Du, and S. M. George, “Protection of polymer from atomic-oxygen erosion using Al₂O₃ atomic layer deposition coatings,” *Thin Solid Films*, vol. 516, no. 12, pp. 4036–4039, Apr. 2008.
- [113] W. Kern, *Thin Film Processes II*. Academic Press, 1991.
- [114] S. M. George, “Atomic Layer Deposition: An Overview,” *Chem. Rev.*, vol. 110, no. 1, pp. 111–131, Jan. 2010.
- [115] M. Leskelä and M. Ritala, “Atomic layer deposition (ALD): from precursors to thin film structures,” *Thin Solid Films*, vol. 409, no. 1, pp. 138–146, 2002.
- [116] M. Ritala and J. Niinistö, “Industrial applications of atomic layer deposition,” *ECS Trans.*, vol. 25, no. 8, pp. 641–652, 2009.
- [117] R. L. Puurunen, “Surface chemistry of atomic layer deposition: A case study for the trimethylaluminum/water process,” *J. Appl. Phys.*, vol. 97, no. 12, p. 121301, Jun. 2005.
- [118] J. Kiihamäki, H. Kattelus, M. Blomberg, R. Puurunen, M. Laamanen, P. Pekko, J. Saarilahti, H. Ritala, and A. Rissanen, “Low-Temperature Processes for MEMS Device Fabrication,” in *Advanced Materials and Technologies for Micro/Nano-Devices, Sensors and Actuators*, Springer, 2010, pp. 167–178.
- [119] O. M. Nayfeh, “Graphene Transistors on Mechanically Flexible Polyimide Incorporating Atomic-Layer-Deposited Gate Dielectric,” *IEEE Electron Device Lett.*, vol. 32, no. 10, pp. 1349–1351, 2011.
- [120] J. Perelaer, P. J. Smith, D. Mager, D. Soltman, S. K. Volkman, V. Subramanian, J. G. Korvink, and U. S. Schubert, “Printed electronics: the

- challenges involved in printing devices, interconnects, and contacts based on inorganic materials,” *J. Mater. Chem.*, vol. 20, no. 39, pp. 8446–8453, 2010.
- [121] L. T. Le, M. H. Ervin, H. Qiu, B. E. Fuchs, and W. Y. Lee, “Graphene supercapacitor electrodes fabricated by inkjet printing and thermal reduction of graphene oxide,” *Electrochem. Commun.*, vol. 13, no. 4, pp. 355–358, 2011.
- [122] V. Dua, S. P. Surwade, S. Ammu, S. R. Agnihotra, S. Jain, K. E. Roberts, S. Park, R. S. Ruoff, and S. K. Manohar, “All-Organic Vapor Sensor Using Inkjet-Printed Reduced Graphene Oxide,” *Angew. Chem. Int. Ed.*, vol. 49, no. 12, pp. 2154–2157, 2010.
- [123] P. Calvert, “Inkjet printing for materials and devices,” *Chem. Mater.*, vol. 13, no. 10, pp. 3299–3305, 2001.
- [124] P. M. Dentinger, W. M. Clift, and S. H. Goods, “Removal of SU-8 photoresist for thick film applications,” *Microelectron. Eng.*, vol. 61, pp. 993–1000, 2002.
- [125] R. Engelke, J. Mathuni, G. Ahrens, G. Gruetzner, M. Bednarzik, D. Schondelmaier, and B. Loechel, “Investigations of SU-8 removal from metallic high aspect ratio microstructures with a novel plasma technique,” *Microsyst. Technol.*, vol. 14, no. 9–11, pp. 1607–1612, 2008.
- [126] A. Del Campo and C. Greiner, “SU-8: a photoresist for high-aspect-ratio and 3D submicron lithography,” *J. Micromechanics Microengineering*, vol. 17, no. 6, p. R81, 2007.
- [127] K. R. Williams and R. S. Muller, “Etch rates for micromachining processing,” *Microelectromechanical Syst. J. Of*, vol. 5, no. 4, pp. 256–269, 1996.
- [128] K. R. Williams, K. Gupta, and M. Wasilik, “Etch rates for micromachining processing-part II,” *J. Microelectromechanical Syst.*, vol. 12, no. 6, pp. 761–778, Dec. 2003.
- [129] P. A. Köllensperger, W. J. Karl, M. M. Ahmad, W. T. Pike, and M. Green, “Patterning of platinum (Pt) thin films by chemical wet etching in Aqua Regia,” *J. Micromechanics Microengineering*, vol. 22, no. 6, p. 067001, Jun. 2012.
- [130] C. W. Ammen, “Collectors and Separators,” in *Recovery and Refining of Precious Metals*, Springer, 1984, pp. 174–186.
- [131] W. Yu and T.-M. Ko, “Surface characterizations of potassium-hydroxide-modified Upilex-S® polyimide at an elevated temperature,” *Eur. Polym. J.*, vol. 37, no. 9, pp. 1791–1799, Sep. 2001.
- [132] S. Park, E. Lee, and S. Kwon, “Influence of surface treatment of polyimide film on adhesion enhancement between polyimide and metal films,” *Bull.-KOREAN Chem. Soc.*, vol. 28, no. 2, p. 188, 2007.
- [133] S.-C. Park and Y.-B. Park, “Effect of Ar+ Radiofrequency Plasma Treatment Conditions on the Interfacial Adhesion Energy Between Atomic-Layer-Deposited Al₂O₃ and Cu Thin Films in Embedded Capacitors,” *J. Electron. Mater.*, vol. 37, no. 10, pp. 1565–1573, Oct. 2008.
- [134] T. O. Kääriäinen, D. C. Cameron, and M. Tanttari, “Adhesion of Ti and TiC Coatings on PMMA Subject to Plasma Treatment: Effect of Intermediate Layers of Al₂O₃ and TiO₂ Deposited by Atomic Layer Deposition,” *Plasma Process. Polym.*, vol. 6, no. 10, pp. 631–641, 2009.

- [135] Y.-S. Lin and H.-M. Liu, "Enhanced adhesion of plasma-sputtered copper films on polyimide substrates by oxygen glow discharge for microelectronics," *Thin Solid Films*, vol. 516, no. 8, pp. 1773–1780, Feb. 2008.
- [136] P. R. Woodward, "Contact angle measurements using the drop shape method," *First Ten Angstroms Inc Portsm. VA*, 1999.
- [137] N. J. Chou, D. W. Dong, J. Kim, and A. C. Liu, "An XPS and TEM study of intrinsic adhesion between polyimide and Cr films," *J. Electrochem. Soc.*, vol. 131, no. 10, pp. 2335–2340, 1984.
- [138] D01 Committee, "Test Methods for Measuring Adhesion by Tape Test," ASTM International, 2009.
- [139] D01 Committee, "Test Method for Pull-Off Strength of Coatings Using Portable Adhesion Testers," ASTM International, 2009.
- [140] S.-H. Jen, J. A. Bertrand, and S. M. George, "Critical tensile and compressive strains for cracking of Al₂O₃ films grown by atomic layer deposition," *J. Appl. Phys.*, vol. 109, no. 8, pp. 084305–084305, 2011.
- [141] S.-H. Jen, S. M. George, R. S. McLean, and P. F. Carcia, "Alucone Interlayers to Minimize Stress Caused by Thermal Expansion Mismatch between Al₂O₃ Films and Teflon Substrates," *ACS Appl. Mater. Interfaces*, vol. 5, no. 3, pp. 1165–1173, Feb. 2013.
- [142] N. US Department of Commerce, "NIST Atomic Spectra Database." [Online]. Available: <http://www.nist.gov/pml/data/asd.cfm>. [Accessed: 15-Dec-2013].
- [143] "DuPont Teijin Films - USA - Information Center." [Online]. Available: <http://usa.dupontteijinfilms.com/informationcenter/technicalinfo.aspx>. [Accessed: 12-Nov-2013].
- [144] R. R. Richardson Jr, J. A. Miller, and W. M. Reichert, "Polyimides as biomaterials: preliminary biocompatibility testing," *Biomaterials*, vol. 14, no. 8, pp. 627–635, 1993.
- [145] G. Bianchi, F. Mazza, and T. Mussini, "Catalytic decomposition of acid hydrogen peroxide solutions on platinum, iridium, palladium and gold surfaces," *Electrochimica Acta*, vol. 7, no. 4, pp. 457–473, 1962.
- [146] R. Zeis, T. Lei, K. Sieradzki, J. Snyder, and J. Erlebacher, "Catalytic reduction of oxygen and hydrogen peroxide by nanoporous gold," *J. Catal.*, vol. 253, no. 1, pp. 132–138, 2008.
- [147] K. Alzoubi, S. Lu, B. Sammakia, and M. Poliks, "Factor Effect Study for the High Cyclic Bending Fatigue of Thin Films on PET Substrate for Flexible Displays Applications," *J. Disp. Technol.*, vol. 7, no. 6, pp. 348–355, Jun. 2011.
- [148] K. Alzoubi, S. Lu, B. Sammakia, and M. Poliks, "Experimental and Analytical Studies on the High Cycle Fatigue of Thin Film Metal on PET Substrate for Flexible Electronics Applications," *IEEE Trans. Compon. Packag. Manuf. Technol.*, vol. 1, no. 1, pp. 43–51, Jan. 2011.
- [149] F. Faupel, C. H. Yang, S. T. Chen, and P. S. Ho, "Adhesion and deformation of metal/polyimide layered structures," *J. Appl. Phys.*, vol. 65, no. 5, p. 1911, 1989.

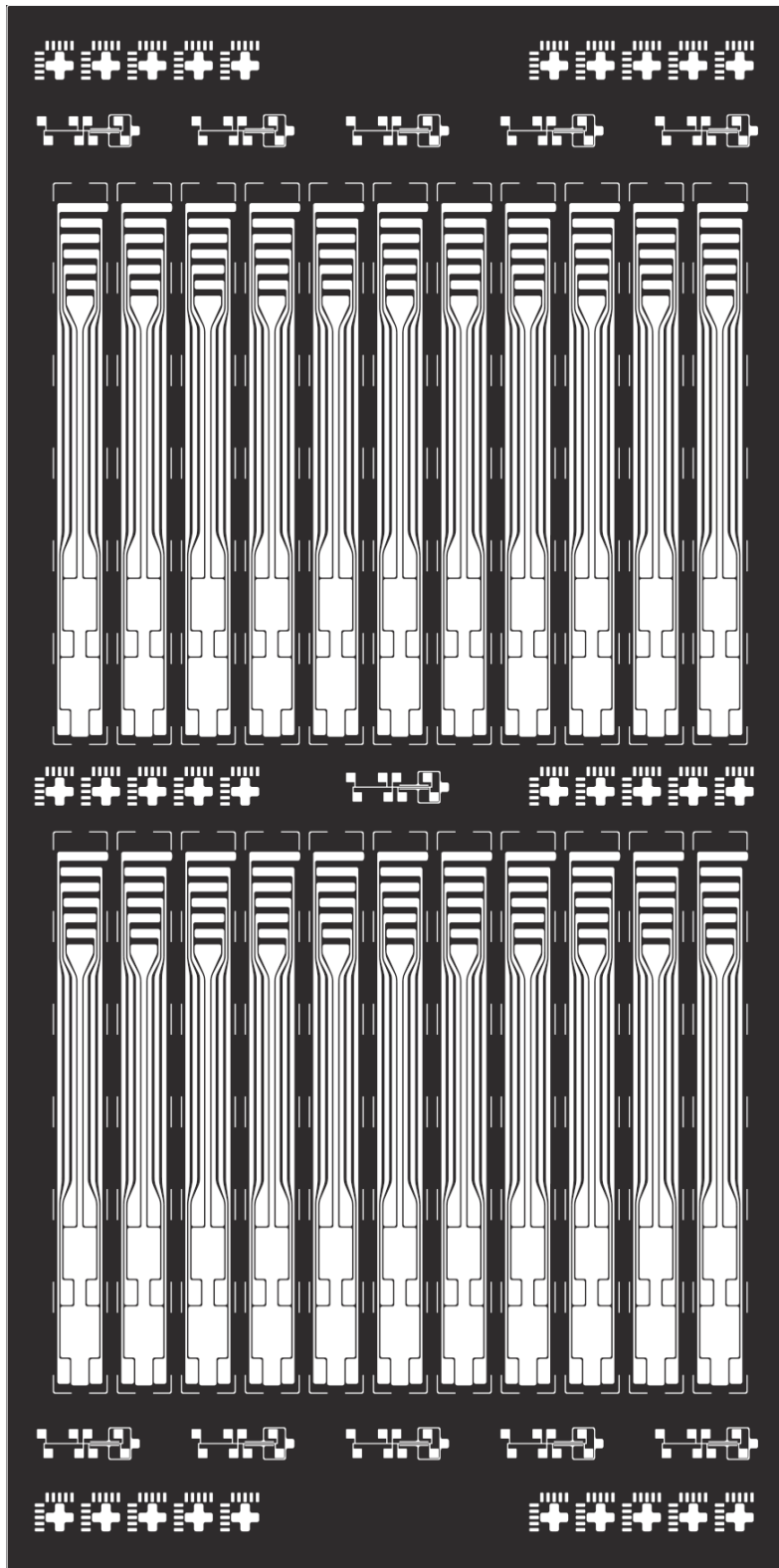
- [150] Y.-H. Kim, J. Kim, G. F. Walker, C. Feger, and S. P. Kowalczyk, "Adhesion and interface investigation of polyimide on metals," *J. Adhes. Sci. Technol.*, vol. 2, no. 1, pp. 95–105, 1988.
- [151] T. Ohmi, T. Ichikawa, T. Shibata, K. Matsudo, and H. Iwabuchi, "In situ substrate-surface cleaning for very low temperature silicon epitaxy by low-kinetic-energy particle bombardment," *Appl. Phys. Lett.*, vol. 53, no. 1, pp. 45–47, 1988.
- [152] S. Tanaka and H. Ito, *Method of manufacturing semiconductor device*. Google Patents, 2007.
- [153] W. R. Burger and R. Reif, "An optimized in situ argon sputter cleaning process for device quality low-temperature ($T \leq 800^\circ \text{C}$) epitaxial silicon: Bipolar transistor and pn junction characterization," *J. Appl. Phys.*, vol. 62, no. 10, pp. 4255–4268, 1987.
- [154] R. D. Arnell, P. J. Kelly, and J. W. Bradley, "Recent developments in pulsed magnetron sputtering," *Surf. Coat. Technol.*, vol. 188, pp. 158–163, 2004.
- [155] M. I. Putkonen, "ALD Applications Beyond Outside IC Technology-Existing and Emerging Possibilities," *ECS Trans.*, vol. 25, no. 4, pp. 143–155, 2009.
- [156] D. S. Finch, T. Oreskovic, K. Ramadurai, C. F. Herrmann, S. M. George, and R. L. Mahajan, "Biocompatibility of atomic layer-deposited alumina thin films," *J. Biomed. Mater. Res. A*, vol. 87A, no. 1, pp. 100–106, Oct. 2008.
- [157] Y. J. Lee, G.-P. Kim, Y. Bang, J. Yi, J. G. Seo, and I. K. Song, "Activated carbon aerogel containing graphene as electrode material for supercapacitor," *Mater. Res. Bull.*, vol. 50, pp. 240–245, Feb. 2014.
- [158] X. Wu and A.-W. Xu, "Carbonaceous hydrogels and aerogels for supercapacitors," *J. Mater. Chem. A*, 2013.
- [159] L. Borchardt, M. Oschatz, and S. Kaskel, "Tailoring porosity in carbon materials for supercapacitor applications," *Mater. Horiz.*, 2014.
- [160] T. Kristiansen, "Aerogels; a new class of materials for catalytic purposes," 2013.
- [161] R. Mueller, S. Zhang, B. Neumann, M. Bäumer, and S. Vasenkov, "Self-diffusion of carbon dioxide in samaria/alumina aerogel catalyst using high field NMR diffusometry," *J. Chem. Phys.*, vol. 139, no. 15, p. 154703, Oct. 2013.
- [162] K. L. Yeung and W. Han, "Zeolites and mesoporous materials in fuel cell applications," *Catal. Today*.
- [163] H. Maleki, L. Durães, and A. Portugal, "An overview on silica aerogels synthesis and different mechanical reinforcing strategies," *J. Non-Cryst. Solids*, vol. 385, pp. 55–74, 2014.
- [164] J. Cha, S. Kim, K.-W. Park, D. R. Lee, J.-H. Jo, and S. Kim, "Improvement of window thermal performance using aerogel insulation film for building energy saving," *J. Therm. Anal. Calorim.*, pp. 1–6.
- [165] L. Qiu, Y. M. Li, X. H. Zheng, J. Zhu, D. W. Tang, J. Q. Wu, and C. H. Xu, "Thermal-Conductivity Studies of Macro-porous Polymer-Derived SiOC Ceramics," *Int. J. Thermophys.*, pp. 1–14, 2013.

- [166] G. Zu, J. Shen, L. Zou, W. Wang, Y. Lian, Z. Zhang, and A. Du, "Nanoengineering Super Heat-Resistant, strong Alumina Aerogels," *Chem. Mater.*, 2013.
- [167] S. W. Smith, H. Chan, C. Buesch, J. Simonsen, and J. F. Conley, "Improved Temperature Stability of Atomic Layer Deposition Coated Cellulose Nanocrystal Aerogels," *MRS Proc.*, vol. 1465, May 2012.
- [168] R. J. Moon, A. Martini, J. Nairn, J. Simonsen, and J. Youngblood, "Cellulose nanomaterials review: structure, properties and nanocomposites," *Chem. Soc. Rev.*, vol. 40, no. 7, pp. 3941–3994, Jul. 2011.
- [169] A. K. Roy, W. Baumann, I. König, G. Baumann, S. Schulze, M. Hietschold, T. Mäder, D. J. Nestler, B. Wielage, and W. A. Goedel, "Atomic layer deposition (ALD) as a coating tool for reinforcing fibers," *Anal. Bioanal. Chem.*, vol. 396, no. 5, pp. 1913–1919, Mar. 2010.
- [170] C. R. W. N. Ding and E. X. Feng, "Thermal Degradation Behaviors of Cellulose Whiskers," *J. South China Univ. Technol. Nat. Sci. Ed.*, vol. 10, p. 013, 2007.
- [171] A. K. Roy, S. Schulze, M. Hietschold, and W. A. Goedel, "Oxidation protection of carbon fibers by coating with alumina and/or titania using atomic layer deposition," *Carbon*, vol. 50, no. 3, pp. 761–770, Mar. 2012.
- [172] R. g. Gordon, D. Hausmann, E. Kim, and J. Shepard, "A Kinetic Model for Step Coverage by Atomic Layer Deposition in Narrow Holes or Trenches," *Chem. Vap. Depos.*, vol. 9, no. 2, pp. 73–78, 2003.
- [173] A. Yanguas-Gil and J. W. Elam, "Diffusion-Reaction Model of ALD in Nanostructured Substrates: Analytic Approximations to Dose Times as a Function of the Surface Reaction Probability," *ECS Trans.*, vol. 41, no. 2, pp. 169–174, Oct. 2011.
- [174] T. L. Hudson, "Growth, diffusion, and loss of subsurface ice on Mars: Experiments and models," California Institute of Technology, 2008.
- [175] S. Montanari, M. Roumani, L. Heux, and M. R. Vignon, "Topochemistry of Carboxylated Cellulose Nanocrystals Resulting from TEMPO-Mediated Oxidation," *Macromolecules*, vol. 38, no. 5, pp. 1665–1671, Mar. 2005.
- [176] S. Noorani, J. Simonsen, and S. Atre, "Polysulfone-cellulose nanocomposites," in *Cellulose Nanocomposites, Processing, Characterization and Properties*, ACS Symposium Series, 2006, vol. 938.
- [177] Sean W. Smith, Christian Buesch, David Matthews, John Simonsen, and John F. Conley, Jr., "Improved oxidation resistance of organic/inorganic composite atomic layer deposition coated cellulose nanocrystal aerogels," *Nanotechnol. Submitt.*, Oct. 2013.
- [178] L. B. Kiss, J. Söderlund, G. A. Niklasson, and C. G. Granqvist, "The real origin of lognormal size distributions of nanoparticles in vapor growth processes," *Nanostructured Mater.*, vol. 12, no. 1, pp. 327–332, 1999.
- [179] L. B. Kiss, J. Söderlund, G. A. Niklasson, and C. G. Granqvist, "New approach to the origin of lognormal size distributions of nanoparticles," *Nanotechnology*, vol. 10, no. 1, p. 25, 1999.

- [180] B.-X. Wang, L.-P. Zhou, and X.-F. Peng, "A fractal model for predicting the effective thermal conductivity of liquid with suspension of nanoparticles," *Int. J. Heat Mass Transf.*, vol. 46, no. 14, pp. 2665–2672, 2003.

Appendices

Appendix 1: Mask set

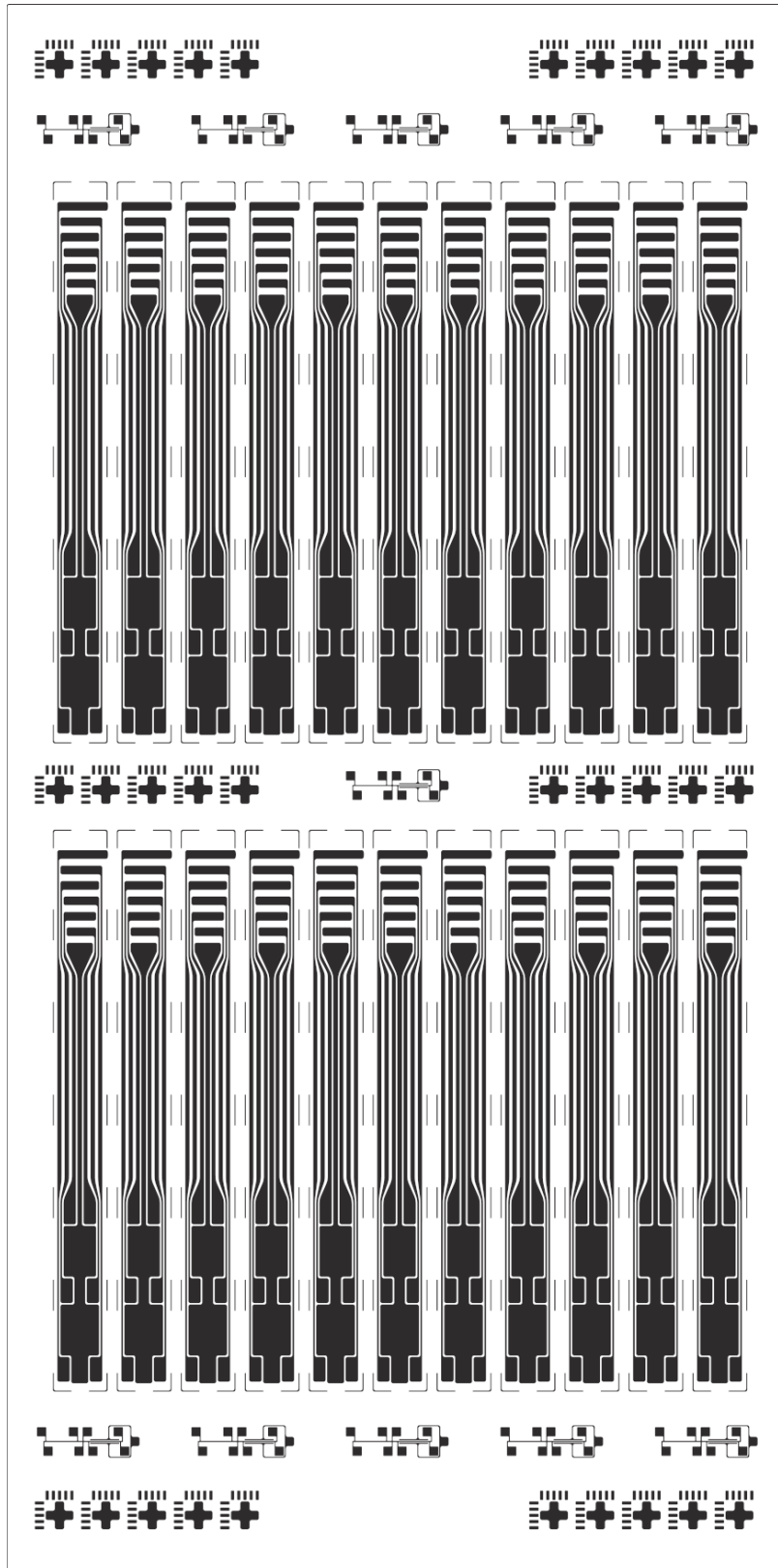


This appendix presents only masks used in the presented process flow. Other masks were also designed to enable easier contact, different electrode sizes, or masking / revealing of electrode pads.

Left: Mask 1, dark field mask for Pt/Ir lift-off patterning, for use with S1818 positive photoresist.

Photoresist will remain in black areas.

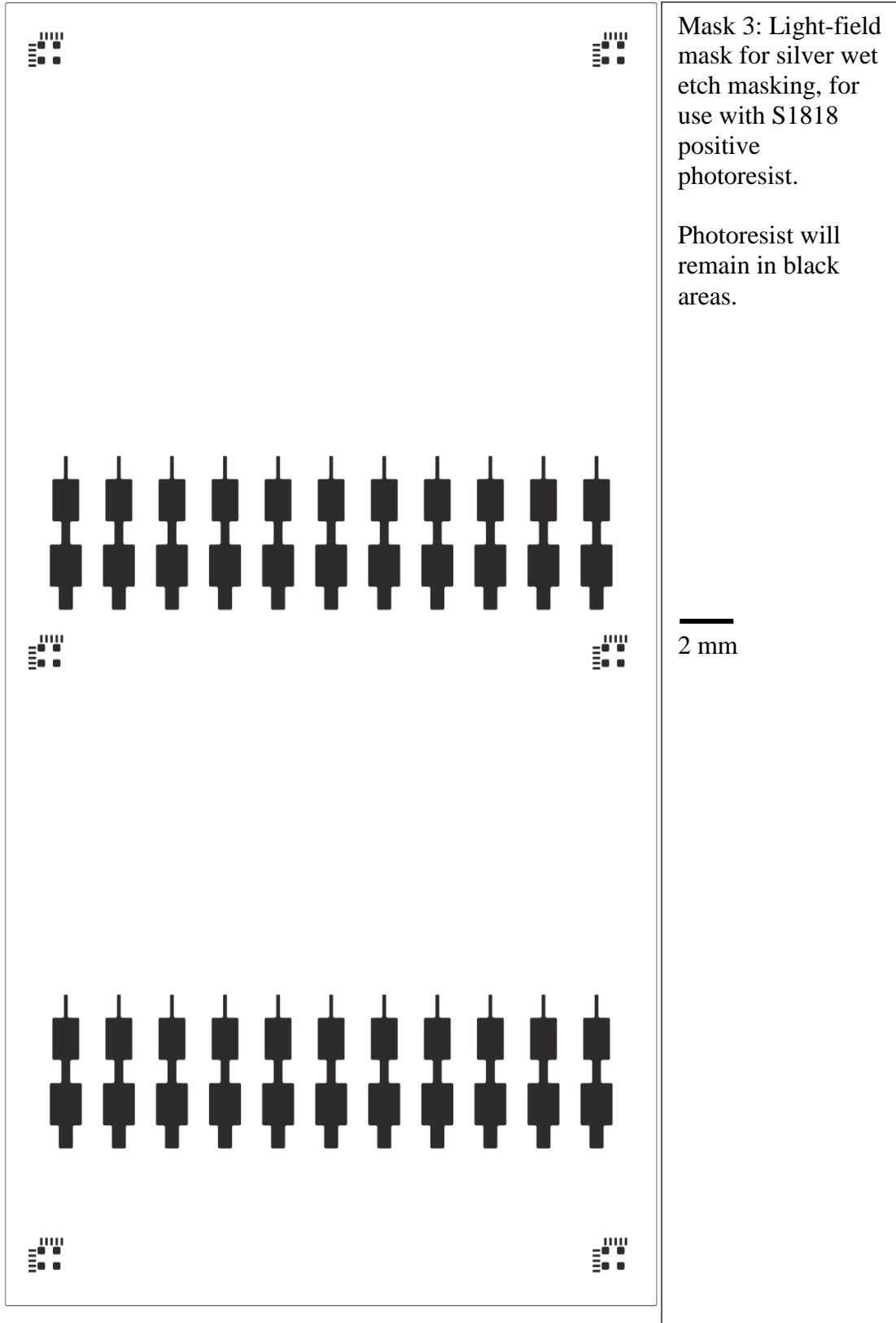
—
2 mm

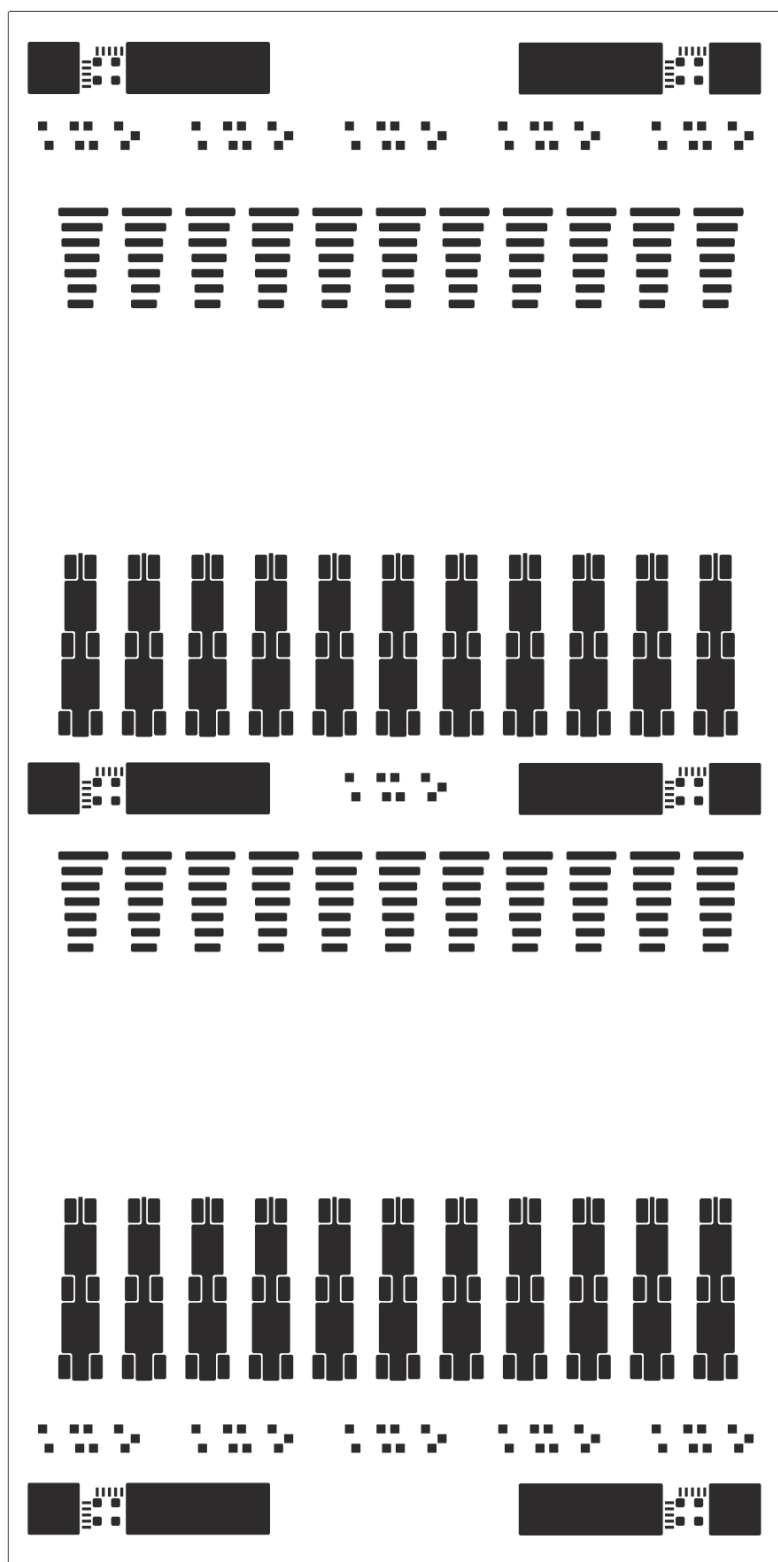


Mask 2: Light-field mask for gold wet etch masking, for use with S1818 positive photoresist.

Photoresist will remain in black areas.

—
2 mm





Mask 4: Light-field mask for SU-8 patterning, for use with SU-8 2 negative photoresist.

Photoresist will remain in white areas.

—
2 mm

Appendix 2: Run sheet through SU-8 deposition

#	Process	Date	Operator	Tool and other notes
1	Cut substrate			
25.4 x 25.4 mm rectangles, material used:				
2	Rigidize			
Apply AID-cleaned glass slides to Gel-Pak DGL film, cut, peel, and apply samples to gel. Remove excess gel.				
3	AID clean			
Thorough sequential rinses with acetone, isopropyl alcohol, and water				
4	Plasma treatment			
Ar plasma, 5m, 300W, 25 sccm Ar, 20 mTorr chamber pressure, using 418 etcher				
5	Liftoff pattern - Pt			
1 dropper S1818, spin 30s 3k RPM, bake 1.5m 85 C, dry surface with gentle N2, expose 6.5s, develop ~15s in 315 developer, rinse thoroughly with DI water. Change developer every 2 samples. Use photoroom aligner.				
Develop times:				
6	Plasma treatment			
Ar plasma, 5m, 300W, 25 sccm Ar, 20 mTorr chamber pressure				
7	Pt/Ir sputter			
Recipe:				
Run contents, thickness, and sample positions:				
8	Pt/Ir liftoff			
5m acetone sonication, 2m settle, acetone rinse, H2O bath, N2 dry				
Sonication times:				
9	Etch pattern - Au			
1 dropper S1818, spin 30s 3k RPM, bake 3m 85 C, expose 7s, bake 3m 85 C, develop ~20s in 315 developer, rinse thoroughly with DI water. Change developer every 2 samples. Use photoroom aligner.				
Develop times:				
10	Au etch			
KI-based TFS etchant, room temp, immerse for 55 seconds, wash thoroughly with DI water				
11	Ag evaporation			
200 nm, 1 50g pellet Ag, <20 mTorr crossover, 6×10^{-6} Torr base pressure				
Run contents, thickness, and sample positions:				
12	Etch pattern - Ag			

1 dropper S1818, spin 30s 3k RPM, bake 3m 85 C, expose 8s, bake 3m 85 C, develop 30s in 1:315 developer 4:DI H₂O, rinse thoroughly with DI water. Change developer every 2 samples. Use photoroom aligner.

Develop times:

--	--	--

13 Ag etch

1 HNO₃ : 1 H₂O₂ : 27 DI H₂O, room temp, immerse for 1m 15s, wash thoroughly with DI water

--	--	--

14 Resist pattern - SU-8:2

1 dropper SU-8:2, spin 500 RPM w/100 RPM ramp for 10s and 2k RPM w/300 RPM/s ramp for 30s, bake 1m 65 C, bake 3m 95 C, bake 1m 65 C, expo 20s, bake 1m 65 C, 1m 95 C, 1m 65 C, develop 30s, wash thoroughly with IPA. Use photoroom aligner.

Develop times:

--	--	--

--	--	--

Appendix 3: 50 nm ALD Al₂O₃ recipe

This recipe is presented in the language of the Gemstar Arradiance tool used, but labels are descriptive enough to interpret.

Step	Label	Device Name	Action	Value	Branch
1		Pump		0	
2		EXPO_Heater	Set_to_On	0	
3		MFC_Flow	Set_to_Value	200	
4		Manifold_1_Heat	Set_to_Value	115	
5		Manifold_2_Heat	Set_to_Value	115	
6		Precursor_1_Heat	Set_to_Value	0	
7		Precursor_2_Heat	Set_to_Value	0	
8		Chamber_Door_Heat	Set_to_Value	175	
9		Chamber_Heat	Set_to_Value	175	
10		Chamber_Heat	Wait_Until_Set_Point_+/ -	3	
11		Manifold_1_Heat	Wait_Until_Set_Point_+/ -	3	
12		Manifold_2_Heat	-	3	
13		Delay_(Sec.)		900	
14	LoopStart	Manifold_1_Heat	Wait_Until_Set_Point_+/ -	3	
15		Manifold_2_Heat	Wait_Until_Set_Point_+/ -	3	
16		Chamber_Heat	-	3	
17		Chamber_Door_Heat	Wait_Until_Set_Point_+/ -	3	
18		MFC_Flow	Set_to_Value	40	
19		Delay_(Sec.)		1.5	
20	TMA	ALD_2_Actuator	Pulse_(mSec.)	20	
21		Delay_(Sec.)		0.5	
22		MFC_Flow	Set_to_Value	90	
23		Delay_(Sec.)		10	
24		MFC_Flow	Set_to_Value	40	
25		Delay_(Sec.)		1.5	
26	H2O	ALD_5_Actuator	Pulse_(mSec.)	20	

27	Delay_(Sec.)		1	
28	MFC_Flow	Set_to_Value	90	
29	Delay_(Sec.)		10	
30	Loop_n_Times		455	LoopStr
31	Standby		0	t

Appendix 4: Matlab code for ALD model

```

%{
ALD Pulse Saturation Time Caluclator

David Matthews
Oregon State University, Conley group
8 August 2012

Model used:
Yanguas-Gil, A. and Elam, J. Self-Limited Reaction-Diffusion
    in Nanostructured Substrates: Surface Coverage Dynamics
    and Analytic Approximations to ALD Saturation Times.
    Chemical Vapor Deposition, 2012.
%}

clear;

% INPUT -----
---
% Replace X = X statements with X = (value) to shortcut
calculation of X

% Output options (t = inf for porosity = 0)
clc;                % Clear command window
hold off;          % Set to "on" to overlay successive
runs

% Corrections for transport time in our tools --
%tGemstar = 0;     % Transport time in GEMSTAR tool, sec
%tPico = 0;        % Transport time in PicoSun tool, sec

% Constants ---
k = 1.3806488E-23; % Boltzmann constant, J/K
Na = 6.022141E23;  % Avogadro's number, mol^-1

```

```

% Process ---
T = 473;           % Chamber temperature, K
c = 0.9999;       % Desired fractional coverage at substrate
                  % (c doesn't affect much for beta0 = 1)
time = [30, 120, 600, 600]; % Soak times, s (try a few!)
tpulse = [.02, .06, .18, 1]; % Pulse times, s
pTorr = 1;        % Total chamber pressure in Torr
flow = 150;       % Flow rate in sccm
p = 133.322*pTorr; % Total chamber pressure in Pa
Vchamber = 2163.1/1000000 % Chamber volume, m^-3

% Sample geometry ---
d = 50E-9;        % Fiber separation

% Range of fiber radii, m
r = 1E-10 : 1E-10 : d/2; % start:step:end

sizer = size(r,2);
sizetime = size(time,2);
L_Elam = zeros(sizetime,sizer);
L_measure = zeros(sizetime,floor(sizer/100));

%eps_t = 1;       % Porosity available for xport, 1 if
planar
%delta = 1;       % Constrictivity, 1 if planar
%tau = 1;         % Tortuosity, 1 if planar

% Averse surface area of adsorption site
%r_p = 0.5E-9;    % Precursor molecular radius, m
%s0 = pi*r_p^2;  % Estimated area, m^2
s0 = 5E-19       % 4E-19 m^2 for Hf(NMe2); 5E-19 works for
TMA

```

```

% Precursor ---
beta0 = 1;           % Fractional reaction probability
%D = 1.6E-5;        % Diffusivity in air
                    % (CO2 in air = 1.6E-5 m^2/s)

% Mass
m_mol = 72.086E-3;  % Precursor molar mass, kg/mol
m = m_mol/Na;       % Precursor molecular mass, kg
%m = m;

m_mol_gas = 28.0134E-3; % Carrier gas molar mass, kg/mol
m_gas = m_mol_gas/Na; % Carrier gas molecular mass, kg
%m_gas = m_gas;

%p = p;

% CALCULATIONS -----
---

% Precursor concentration
pPrecursor = 133.322 * (8.22 - 2134/T); % Precursor partial
pressure, Pa
molrate = 4.46E-5 * pPrecursor/p * flow; % Molar precursor
flow rate
n0 = molrate .* tpulse * Na / Vchamber;

%S0 = 3.91121E5;     % Surface area at pulse 0, m^2/kg
%V0 = 1.00973E-3;   % Volume to coat at pulse 0,
m^3/kg
%n0 = pPrecursor/(k*T) % Precursor concentration at
surface, %m^-3

vth = sqrt(8*k*T/(m*pi)); % Mean thermal velocity
(magnitude), %m/s

```

```

% Diffusion constant in free space, m^2/s
D = 1.858E-7 * T^(3/2) * sqrt( 1/(m_mol*1E3) +
1/(m_mol_gas*1E3)...
    )/(p*0.5*(3.5)^2);
%D = 3E-4/8 * k * T *
sqrt(k*T/(2*pi)*(1/m+1/m_gas))/(p*0.5*(3.5E-10)^2)

for i = 1:sizetime;          % Depth-dependent calculations
(loop %over T values)
    % Open pore network of cylinders assumed
    % Unit cell is a cube with vertices at fiber intersections

    V = zeros(1,sizer);      % Free volume per unit cell
    S = zeros(1,sizer);      % Surface area per unit cell
    Sbar = zeros(1,sizer);   % Surface area per unit cell
%volume
    porosity = zeros(1,sizer); % Normalized porosity
    Deff = zeros(1,sizer);    % Effective diffusivity
    gamma = zeros(1,sizer);  % Precursor excess number

    for j = 1:sizer;
        % V = V_cell - (12/4 cylinders - 3*8/8 bicylinders +
8/8
% tricylinders)
        V(j) = d^3 - 3*pi*d*r(j)^2 + 16*r(j)^3 - 8*(2-...
sqrt(2))*r(j)^3;
        % S = 12/4 cylinders - 3*8/8 bicylinders + 8/8
% tricylinders
        S(j) = 6*d*pi*r(j) - 32*3/2*r(j)^2 + 24*(2-...
sqrt(2))*r(j)^2;
        Sbar(j) = S(j)/d^3;
        porosity(j) = V(j)/d^3;
        Deff(j) = D * porosity(j)^3;
        %Deff = D .* porosity * constrictivity / tortuosity
        %Deff ~2E-6??
    end
end

```

```

        % Damkohler number = reaction rate/diffusion rate
        % alpha(j) = L(i)^2 / 4 * Sbar(j) * vth * beta0 /
% Deff(j);
        % Incorporated into the model step below to extract L
% dependence

        % Precursor excess number = precursor molecules per
unit
% site
        gamma(j) = V(j) * n0(i) * s0 / S(j);

        % sc expression for non-saturating precursor loss (ie,
% PEALD)
        % only applies to circular pores in this form (AR)
        %sc_loss = -log(1-c)/alpha * exp(sqrt(gamm))/...
        % (1+(2*AR-sqrt(gamm))/(2*AR+sqrt(gamm))*...
        % (1-exp(-2*sqrt(gamm)))));
end;

% Model -----
---

for j = 1:sizer;
    L_Elam(i,j) = sqrt(4 * Deff(j) * (time(i) * gamma(j)
+...
        log(1-c)/(Sbar(j)*vth*beta0)));
    if mod(r(j),10E-9) == 0;
        L_measure(i,ceil(j/100)) = L_Elam(i,j);
    end
end
end

%plot(r,V)

```

```

% Output -----
-

% %Text
% for i = 1:size(L_measure,1);
%     ['Time: ' num2str(time(i)) ' seconds']
%     for j = 1:size(L_measure,2);
%         ['r: ' num2str(j*10) 'nm, depth: '
num2str(L_measure(i,j)*1E6) 'um']
%     end
% end
%ratio = L_measure(2,1)/L_measure(1,1)

% Observed times
x10 = [ 10 10 ];
y30 = [ 22 50 ];
y120 = [ 0 0 ];
y600 = [ 230 390 ];

% Plots
figure(1)
semilogy(r.*1E9, L_Elam.*1E6,'linewidth',3)
hold on
semilogy(x10,y30,'-',x10,y120,'-',x10,y600,'-', 'linewidth',2)
hold off
set(gca,'FontSize',14)
%title(['Depth for ' num2str(c) ' Coverage vs. Fiber Radius']
)
title(['Depth vs. Fiber Radius'] )
xlabel('Fiber radius, nm')
ylabel('log( Depth ), um')
legend([num2str(time(1)) 's Exposure time'],
[num2str(time(2))...
's'], [num2str(time(3)) 's'])
text(10-6.5, y30(1)+10, ['Observed range \rightarrow'])

```

```
%text(10-3.6, y30(1)-5, [num2str(y30(1)) ' - ' num2str(y30(2))  
' %um'])  
%text(10+0.2, y600(2)+30, [num2str(y600(1)) ' - '  
%num2str(y600(2)) ' um'])  
  
figure(2)  
plot(L_Elam.*1E6, r.*1E9, 'linewidth',3)  
set(gca,'FontSize',14,'LineWidth',2.5)  
axis([0 300 10 d*0.5E9])  
title('Thickness Profile')  
xlabel('Depth, um')  
ylabel('Fiber raduis, nm')  
legend([num2str(time(1)) 's Exposure time'],  
[num2str(time(2))...  
 's'],[num2str(time(3)) 's'])
```